Optical pulse dynamics in nonlinear and resonant nanocomposite media

by

Joshua Eric Soneson

A Dissertation Submitted to the Faculty of the

Graduate Interdisciplinary Program
in Applied Mathematics

In Partial Fulfillment of the Requirements
For the Degree of

Doctor of Philosophy

In the Graduate College

The University of Arizona

2 0 0 5

THE UNIVERSITY OF ARIZONA
GRADUATE COLLEGE

As members of the dissertation committee, we certify that we have read the dissertation prepared by Joshua Eric Soneson entitled, *Optical Pulse Dynamics in Nonlinear and Resonant Nanocomposite Media*, and recommend that it be accepted as fulfilling the dissertation requirement for the degree of Doctor of Philosophy.

_____ Date: 7/14/2005
Ildar Gabitov

_____ Date: 7/14/2005
Robert Indik

_____ Date: 7/14/2005
Franko Kueppers

Final approval and acceptance of this dissertation is contingent upon the candidate's submission of the final copies of the dissertation to the Graduate College.

I hereby certify that I have read this dissertation prepared under my direction and recommend that it be accepted as fulfilling the dissertation requirement.

_____ Date: 7/14/2005
Dissertation Director: Ildar Gabitov

Statement by Author

This dissertation has been submitted in partial fulfillment of requirements for an advanced degree at The University of Arizona and is deposited in the University Library to be made available to borrowers under rules of the Library.

Brief quotations from this dissertation are allowable without special permission, provided that accurate acknowledgment of source is made. Requests for permission for extended quotation from or reproduction of this manuscript in whole or in part may be granted by the copyright holder.

SIGNED: Joshua Eric Soneson

Acknowledgments

I would like to sincerely thank my advisor Ildar Gabitov and Professor Robert Indik. Their guidance, expertise, and general good nature through both the research and writing stages of this work will always be appreciated.

I would also like to thank my committee members Franko Kueppers, Allen Newell, Bane Vasic, Moysey Brio, and Alejandro Aceves; collaborators Vladimir Drachev, Vladimir Shalaev, Andrei Maimistov, Natalia Litchinitser, Misha Stepanov, Yeojin Chung, and Kostya Turitsyn; Professors Linn Mollenauer and Joceline Lega; Program Head Michael Tabor; my Los Alamos mentor Avner Peleg; my Sandia mentor Ray Tuminaro and his postdoc (at the time) Jonathan Hu; and the great friends I met along the way: Subok Park, Eric Forgoston, Nakul Chitnis, Milos Ivkovich, Pasha Lushnikov, Tomas and Katarina Dohnal, Ignacio Rozada, and Hernan Rozenfeld.

A special thanks goes to the unsung heros who keep the machine running: Applied Math staff members Linda Silverman and Stacey Wiley, and LANL/T7 staff members Esther Vigil and Crystal Martinez.

A very special thanks goes to my parents, Eric and Trudy Soneson. The world would be a much better place with more people like them.

This work was supported by Arizona Proposition 301 and the National Science Foundation through a VIGRE fellowship.

Table of Contents

TABLE OF CONTENTS—*Continued*

List of Figures

List of Figures—*Continued*

LIST OF FIGURES—*Continued*

LIST OF FIGURES—*Continued*

List of Figures—*Continued*

List of Figures—*Continued*

LIST OF FIGURES—*Continued*

List of Tables

Abstract

The constantly increasing volume of information in modern society demands a better understanding of the physics and modeling of optical phenomena, and in particular, optical waveguides which are the central component of information systems. Two ways of advancing this physics are to push current technologies into new regimes of operation, and to study novel materials which offer superior properties for practical applications. This dissertation considers two problems, each addressing the above-mentioned demands. The first relates to the influence of high-order nonlinear effects on pulse collisions in existing high-speed communication systems. The second part is a study of pulse dynamics in a novel nanocomposite medium which offers great potential for both optical waveguide physics and applications. The nanocomposite consists of metallic nanoparticles embedded in a host medium. Under resonance conditions, the optical field excites plasmonic oscillations in the nanoparticles, which induce a strong nonlinear response.

Analytical and computational tools are used to study these problems. In the first case, a double perturbation method, in which the small parameters are the reciprocal of the relative frequency of the colliding solitons and the coefficient of quintic nonlinearity, reveals that the leading order effects on collisions are radiation emission and phase shift of the colliding solitons. The analytical results are shown to agree with

numerics. For the case of pulse dynamics in nanocomposite waveguides, the resonant interaction of the optical field and material excitation is studied in a slowly-varying envelope approximation, resulting in a system of partial differential equations. A family of solitary wave solutions representing the phenomenon of self-induced transparency are derived. Stability analysis reveals the solitary waves are conditionally stable, depending on the sign of the perturbation parameter. A characterization of two-pulse interaction indicates high sensitivity to relative phase, and collision dynamics vary from highly elastic to the extreme case where one wave is immediately destroyed by the collision, depositing its energy into a localized hotspot of material excitation. This last scenario represents a novel mechanism for "stopping light".

Chapter 1

Introduction

Electrical cables, which can be viewed as waveguides for electrical signals, have been used to propagate information over large distances for more than 100 years. However, due to capacity limitations, electrical cables were not able to keep up with the dramatic growth of worldwide information traffic during the last decade. Technological developments produced other transmission methods such as wireless and satellite communication. However, only the invention of optical fiber offered a real solution to this problem. This is due to the copious natural bandwidth and low cost of optical fibers. The many beneficial properties of optical fibers lead to numerous applications in various other fields such as medicine, micromachining, navigation, photonic devices, etc. These applications drew from existing analytical and numerical techniques and facilitated the development of new models which now have broad applications in many fields of mathematics and physics.

The bit error rate is a key characteristic of communication systems. In optical communications, this characterization is necessarily extremely low, usually in the neigborhood of $10^{-9} - 10^{-12}$. To achieve such low bit error rates, the energy of optical pulses (bitcarriers) cannot be lower than a certain critical value. The demand

for higher bit rate communication forces the duration of optical pulses to be shorter since bit rate is inversely proportional to optical pulse width. The energy of the optical pulse is proportional to the product of the pulse intensity and width. This means that to fulfill the low bit error rate requirement, pulse intensity must grow as a linear function of bit rate. As intensity increases, the natural nonlinearity of optical fiber begins to influence the propagation dynamics. This nonlinear effect was first considered adverse to system performance, but with increased understanding of nonlinear pulse dynamics, it became clear that waveguide nonlinearity can be beneficial for high-speed communications as well as many other applications utilizing optical fibers.

The nonlinearity of conventional optical fibers can be understood as a linear dependence of the refractive index on pulse intensity, and is known as the Kerr nonlinearity. This nonlinearity is the result of nonresonant light-matter interaction, in which the carrier frequency of the optical field is far from any atomic transition frequency of the medium. The invention of highly nonlinear materials such as chalcogenide glasses permit dramatically enhanced properties of photonic devices utilizing nonresonance nonlinearity. Another method for enhancing nonlinearity is to use resonance interaction of the optical field with active atoms. This enhancement can be acheived by doping waveguides with active atoms whose transition frequencies which are in resonance with the carrier frequency of the optical field. One of the most impressive examples of a device which uses a resonance effect is the erbium-doped fiber amplifier.

The simplest model describing the interaction of active atoms with an optical field is the Maxwell-Bloch system of equations.

Recent progress in nanofabrication technonlogies permits a new type of nonlinear light-matter resonance interaction. In this case, an optical medium is doped with metallic nanoparticles. Electron clouds in these nanoparticles experience oscillations in response to illumination by an optical field. If the carrier frequency of the optical field is in resonance with the natural oscillation frequency of the electron cloud displacement from its equilibrium (plasmonic oscillations), then the polarization of the medium induced by plamonic oscillations is strongly coupled to the optical field. If the field intensity is weak, the interaction is described by the classical Maxwell-Lorentz (ML) model, in which the electric field is coupled to harmonic oscillators (plasmonic oscillations in metallic nanoparticles). The nanoparticles are so small that for large amplitude oscillations, quantum effects must be taken into account. These effects manifest as a cubic anharmonicity in the (Duffing) oscillators which is modeled by the Maxwell-Duffing (MD) equations. Therefore this system is a generalization of the ML model.

This dissertation covers two topics related to nonlinear waveguide optics, one each for nonresonant and resonant interaction. The first topic is a supplement to the well-studied field of nonlinear optical waveguides, and is relevant to multichannel optical communications. The second topic is light interaction with a nanocomposite medium consisting of metallic nanoparticles embedded in a host material.

Nonresonant wavepacket electrodynamics in optical fiber are described to a high degree of accuracy in an envelope approximation (for quasimonochromatic pulses) by nonlinear Schrödinger (NLS)-type equations, a fact that has been verified in countless studies. Under certain conditions, when losses can be ignored or compensated by amplification, the pulse dynamics are described by the ideal NLS equation

$$iu_z + u_{tt} + |u|^2 u = 0,$$

where z is propagation distance, t is time measured in a copropagating frame, and u is the complex electric field envelope. It is well known that ideal NLS supports soliton solutions which are, in certain regimes, good candidates for bit carriers due to their intrinsic robustness to distortions and collisions with other solitons. Since this equation is integrable, optical pulse dynamics may be obtained analytically. However, for high bit rates the optical pulse duration must be short, and short pulses are subject to high-order effects. These effects may be modeled by retaining correction terms in the envelope description of pulse propagation. The result is NLS with additional correction terms which correspond to various high-order effects such as dispersion, stimulated Raman scattering, optical shocking, or high order self-phase modulation, which arises from including additional terms in the expansion of the intensity-dependent refractive index. These corrections result in nonintegrable systems for which a complete description of collisions is unavailable. Thus perturbation

and numerical methods are employed to determine how the high-order terms influence collision interaction. By using appropriate system parameters, the influence of a single correction term may be isolated. The work in Chapter 2 of this dissertation focuses on the influence of quadratic dependence of refractive index on intensity, which appears in the NLS description as an additional quintic nonlinear term.

Chapter 2 is organized as follows: Section 2.1 presents the derivation of NLS from first principles. In Section 2.2, the soliton perturbation technique is presented and applied to the problem of finding single-pulse stationary solutions to NLS in the presence of high-order corrections. Section 2.3 introduces the double perturbation theory for soliton collisions in the presence of a correction term. The theory is then applied in the case of a quintic nonlinear correction in Section 2.4. Numerical methods for simulating collision problems are introduced and tested in Section 2.5 and then compared with the perturbation theory predictions in Section 2.6. Finally, concluding remarks are made in section 2.7.

The resonance interaction of an optical field with plasmonic oscillations in metallic nanoparticles is considered in an envelope approximation. The cubic nonlinearity induced by quantum effects in nanoparticles introduces self-phase modulation of the material excitation field, which completely changes the light-matter dynamics described by the Maxwell-Lorentz model. In particular, it establishes conditions wherein energy confinement in both optical and material excitation fields (coupled optical-polarization solitary waves) are possible, and introduces highly nontrivial col-

lision dynamics of these solitary waves. New effects described in Chapter 3 have potential applications in photonics technology.

Chapter 3 is organized in the following way: The properties of metallic nanoparticles and the nanocomposite medium are discussed in Section 3.1. Section 3.2 covers the derivation of the MD equations from first principles. A dimensional analysis is conducted in Section 3.3 and a parameter regime where optical pulses may be observed is identified. The symmetries and conservation laws of the MD equations are presented in Section 3.4. In Section 3.5, a family of solitary wave solutions are derived and interpreted. The stability and collision dynamics of the solitary waves are also examined, and a new effect of light trapping by the medium is discovered. The modulational instability of constant-amplitude solutions is studied in Section 3.6. Self-similar solutions of the MD equations are studied in Section 3.8. The numerical methods employed in all these studies are discussed and analyzed in Section 3.9. Finally, the results obtained are reviewed in Section 3.10.

Chapter 2

Ultrashort pulse dynamics in optical communication systems

The nonlinear Schrödinger (NLS) equation has now enjoyed a quarter of a century of reliably predicting optical pulse dynamics in optical fiber. This legacy began in 1980 when a group at Bell Laboratories first observed optical solitons experimentally [1]. Interest in this equation exploded again after the experimental observation of Bose Einstein-condensation [2] in 1995.

The NLS equation was first derived by Gross and Pitaevskii [3, 4, 5] to describe the dynamics of Bose-Einstein condensation. Later, a number of authors derived NLS as a description of laser beam propagation in media with cubic (Kerr) nonlinearity. In this case, the nonlinearity results in an intensity-dependent contribution to the refractive index. The evolution of quasi-monochromatic light in such media was found to be governed by a multi-dimensional NLS equation [6, 7, 8, 9]. From a more general point of view, Benney and Newell showed that NLS is a universal equation which describes the slow modulation of a weakly nonlinear wave packet [10]. The single soliton solution was first discovered by Ostrovsky [9], although the term "soliton" had not yet been

coined. In 1971 Zakharov and Shabat showed that this equation can be solved exactly using the inverse scattering transform, a general solution procedure which accounts for multisoliton dynamics and the evolution of arbitrary initial data. In this work, they also proved the stability of solitons and elastic nature of multisoliton interaction [11].

The NLS equation accurately models optical phenomena in media with cubic nonlinearity, such as self focusing and optical pulse dynamics in nonlinear waveguides [12, 13]. In addition to fundamental nonlinear optics, this equation has a very important industrial application [14], namely that optical solitons can be used as bit carriers in communication systems. This application was predicted in 1973 and was empirically verified seven years later [1].

The nonlinear Schrödinger equation is a simplified description of wavepacket dynamics in optical fibers. It assumes that the spectral width $\Delta\omega$ of the signal is much smaller than the carrier frequency ω_0, so $\Delta\omega/\omega_0 \ll 1$. In this regime, the dispersion curve may be approximated by a quadratic polynomial $k(\omega) \simeq k_0 + \beta_1(\omega - \omega_0) + \beta_2(\omega - \omega_0)^2$. The Kerr effect, which is the linear dependence of the refractive index n on intensity I ($n = n_0 + n_2 I$, where n_0 is the constant part of the refractive index and n_2 is the Kerr coeffient), is assumed to be the leading order nonlinear effect. The Kerr nonlinearity can also be represented as an intensity dependence of the wavenumber $k_0 = k_{lin} + n_2 I$. The NLS description also assumes that the field propagates through weakly lossy media (attenuation coefficient $\gamma \ll 1$). These assumptions are justified

in cases where the characteristic dispersion length z_d and nonlinearity length z_{nl} are much smaller than the attenuation length z_γ ($z_{nl},\ z_d \ll z_\gamma$).

In real optical communication systems, losses are unavoidable. To compensate for this attenuation, optical amplifiers are used to periodically restore the intensity of the signal. This necessarily introduces a new charactersitic scale z_a, the distance between amplifiers, which is similar to the characteristic attentuation distance $z_a \sim z_\gamma$. If the characteristic dispersion and nonlinearity lengths are much larger than this new scale $z_{nl},\ z_d \gg z_a$, then averaging over the amplification distance may be performed, and the slow average dynamics of the pulse are again described by NLS up to $\mathcal{O}(\epsilon^2)$, where $\epsilon = z_a/z_d$ (where $z_d \sim z_{nl}$) [15].

The robustness and stability of NLS solitons suggest the use of nonlinearity to compensate for dispersive broadening. In this way, they may be used as bit carriers in communication systems. This approach was the focus of intense research until the mid 1990's. However, there are two major drawbacks to this technique for long distance communications. First, in single frequency channel transmission, the soliton approach works well if the characteristic dispersion and nonlinearity lengths are much larger than the distance between amplifiers ($z_{nl}, z_d \gg z_a$). However $z_d \sim \tau_0^2/d$, where τ_0 is pulse width and d is the dispersion at the transmission frequency. Thus the applicability of NLS fails at high bitrates BR, when $BR \sim \tau_0^{-1} \sim 1/\sqrt{dz_a}$. Second, transmission systems take advantage of the copious bandwidth of optical fibers by transmitting on multiple frequency channels in a single fiber. The chromatic

dispersion of real fibers is a function of frequency, which causes pulses in different frequency channels to propagate at different group velocities. Eventually the pulses overlap and pass one another which leads to interchannel interaction. In single channel transmission, the pulse dynamics are decomposed into rapid linear amplification and attenuation and slow dispersive broadening and nonlinear self phase modulation. The NLS equation is derived by averaging over the fast process. This averaging may be performed for multichannel transmission only if the characteristic length of interaction z_i is much larger than the amplification distance ($z_{nl}, z_d, z_i \gg z_a$). As soon as interaction distance becomes comparable to amplification distance, soliton bit carrier performance degrades severely.

The scale separation problem can be eliminated using dispersion tapered fiber [16], where fiber spans of decreasing dispersion are used to preserve the balance of dispersive broadening and nonlinearity as pulses attenuate during propagation.

After introducing dispersion tapered fiber spans, the only remaining drawback is the effect of amplifier spontaneous emission, which results in timing jitter. Amplifier noise is broadly distributed in frequency, which effects solitons as phase perturbations. Since the soliton phase is coupled to its velocity, the soliton experiences a random shift in its velocity. As a result, each soliton in a bitstream experiences a different time shift at the end of the line. In principle solitons can "walk" out of their bitslots, resulting in errors. This phenomena is also known as timing jitter or the Elgin-Gordon-Haus effect [17, 18]. Timing jitter can be suppressed by introducing sliding-

frequency guiding filters at semiregular intervals in the transmission link, in such a way that the center frequencies of these filters shift as a linear function of distance. This results in filtering of amplifier noise, while the intrinsic robustness of solitons allows them to adapt to the frequency shift they experience when they pass through the filters [19].

By the late-1990's, the technique of dispersion management had demonstrated its advantages for long distance optical data transmission and became the leading technology in optical fiber communications [20]. This technique involves the use of a periodic dispersion map in which alternating spans of positive and negative dispersion fiber are used to quell limiting effects in long-haul systems. However, for short range communications (such as networks on university campuses or industrial complexes), NLS once again governs the dynamics. In this regime signal amplification is obviated since propagation distances are much shorter than the characteristic attenuation distance. Thus multichannel soliton transmission offers a promising approach for these systems.

Multichannel soliton transmission is also well suited for advanced optical circuitry. The state of the art in traditional electronic circuits is reaching its limit, and thus optical interconnect technology is the most appropriate and promising method for continuing the development of ultrafast information processing. The functional elements of microchips may be connected by optical waveguides, which results in reduced delay and increased intra-chip information transmission. As the level of integration of

electronic circuits increases, malign parasitic effects such as resistance, capacitance, and inductance also increase. These effects introduce relaxation processes which are on the same order of the chip's operating frequency. Thus the transition to optical interconnects must be made to further advance the integration of these devices. Due to the short propagation distances, losses may be ignored and NLS solitons may be used as bit carriers. Thus studying the dynamics of NLS type equations has applications in technology in addition to the advancement of waveguide physics.

The demand for higher bitrates (and clockspeeds) is constantly increasing. In a multichannel system, the bitrate of each channel may be increased by reducing the bitslot duration, which in turn requires the pulse duration to be reduced into the *ultrashort*, or sub-picosecond (10^{-12}s) regime. From a modeling point of view, ultrashort pulses are not adequately described by the NLS equation since the assumptions under which it is derived are no longer valid. Hence higher order correction terms must be retained in the derivation to extend its validity [20]. These generalized models lack some of the nice properties of NLS that make it easy to analyze, such as integrability, which permits analytic solutions via inverse scattering methods. Consequently, a huge research effort (including the material in this chapter) has been launched at these generalized models to understand the implications of high-order effects.

Short pulses governed by NLS collide elastically, i.e., they lose no energy in the collision and the information content of the bitstreams is not affected. But ultrashort pulses do not behave the same way during collisions. They exchange or lose energy

and their characteristic parameters such as amplitude or position, for example, may be shifted. The energy which is lost in collisions is converted to nonlocal radiation which effects other pulses in the bitstream by inducing shifts in their positions in their bitslots, causing timing jitter. The effects of these generalizations of NLS must be studied to determine which parameter regimes offer the best performance in an optical transmission system.

In this chapter, theoretical and numerical tools are presented and used to analyze the dynamics of multichannel ultrashort pulse transmission. First, the NLS is derived in detail from Maxwell's equations. Then the question of how high-order corrections effect single pulse dynamics is investigated using a soliton perturbation theory. The influence of high-order corrections on soliton collisions is then addressed using a two-parameter generalization of the perturbation theory. This analysis is applied to a multichannel system in a parameter regime where the leading-order correction is a quintic nonlinear term and the governing equation is cubic-quintic nonlinear Schrödinger (CQNLS) equation. The leading order parameter shifts and radiation emission are obtained for collisions in the presence of weak quintic nonlinearity. For completeness, numerical methods for pulse propagation are discussed, analyzed, and finally used to compare with the results of the double perturbation theory. Finally, the results of the perturbation theory and numerics are compared and shown to agree.

2.1 Derivation of the nonlinear Schrödinger equation

The ubiquitous NLS equation is central to the field of nonlinear optics, and it is no surprise that it appears in one way or another throughout this dissertation. Its application is not limited to pulse propagation in optical fiber, rather it governs wavepacket dynamics in any weakly nonlinear, dispersive system. Therefore a complete derivation of the equation from first principles is presented in this section. A mathematically rigorous derivation, including its high-order correction terms, may be performed using a multiple scales analysis, and is detailed in Moloney and Newell [13]. However, this derivation is a more complete version of the one in Boyd [21], which is easier to understand because it appeals to one's physical intuition.

The starting point is Maxwell's equations, which describe electrodynamics in the most general sense. In MKS units they are

$$\nabla \cdot \tilde{\mathbf{D}} = \tilde{\rho} \qquad \nabla \cdot \tilde{\mathbf{B}} = 0$$
$$\nabla \times \tilde{\mathbf{E}} = -\frac{\partial \tilde{\mathbf{B}}}{\partial t} \qquad \nabla \times \tilde{\mathbf{H}} = \frac{\partial \tilde{\mathbf{D}}}{\partial t} + \tilde{\mathbf{J}}$$

and are accompanied by the constitutive relations

$$\tilde{\mathbf{B}} = \mu_0 \tilde{\mathbf{H}} \qquad \tilde{\mathbf{D}} = \epsilon_0 \tilde{\mathbf{E}} + \tilde{\mathbf{P}}$$

Here $\tilde{\mathbf{E}}$ and $\tilde{\mathbf{H}}$ are the electric and magnetic field intensities, $\tilde{\mathbf{D}}$ and $\tilde{\mathbf{B}}$ are the electric

and magnetic induction fields, and $\tilde{\rho}$ and $\tilde{\mathbf{J}}$ are the charge and current densities. The constants ϵ_0 and μ_0 are the permittivity and permeability of free space, and $\tilde{\mathbf{P}}$ is the polarization, or the effect the electric field has on the medim through which it propagates.

Throughout this dissertation, the tilde is used to denote highly oscillatory quantities. The speed of variation of the quantities is important because the disparity of time and length scales, namely that the pulse envelope varies slowly compared to the optical carrier wave, is central to the derivation of NLS.

The geometry of the problems under consideration here allows these equations to be simplified in several ways. First, there are no charge or current distrubutions, so the quantities $\tilde{\rho}$ and $\tilde{\mathbf{J}}$ are both zero. All the analysis that follows is for plane wave propagation in which the electric field is assumed to be linearly polarized, the direction of polarization is x, and the propagation direction is z. This assumption is valid in the case of a perfectly cylindrical waveguide because the two transverse components of the field are degenerate and only one needs to be considered. The waveguides under consideration have a cross-sectional area, or "fiber core area", which is small enough to support only the fundamental transverse mode at optical frequencies. Such waveguides are called *monomode* fibers. The transverse structure of the field, which is Gaussian to a good approximation, may be averaged over the cross-section of the waveguide, and thus needs not be considered in the analysis. In accordance with this

insight, a linearly polarized light ansatz is used for the fields:

$$\tilde{\mathbf{E}} = \big(\tilde{E}(t,z), 0, 0\big), \quad \tilde{\mathbf{P}} = \big(\epsilon_0 \tilde{P}(t,z), 0, 0\big), \quad \tilde{\mathbf{H}} = \big(0, \tilde{H}(t,z), 0\big).$$

This representation automatically satisfies the divergence conditions in Maxwell's equations. The curl equations result in coupled scalar advection equations for $\tilde{E}$ and $\tilde{H}$, which can be decoupled by taking cross derivatives and eliminating $\tilde{H}$. This results in the scalar Maxwell wave equation[1]

$$\left(\frac{\partial^2}{\partial z^2} - \frac{1}{c^2}\frac{\partial^2}{\partial t^2}\right)\tilde{E} = \frac{1}{c^2}\frac{\partial^2 \tilde{P}}{\partial t^2}, \tag{2.1}$$

where the speed of light in vacuum $c = (\epsilon_0 \mu_0)^{-1/2}$. This equation is closed by relating the polarization back to the electric field, which requires some knowledge of the medium. The polarization of materials whose atomic resonance frequencies are far

[1]Equation (2.1) is sometimes written in the alternative form

$$\frac{\partial^2 \tilde{E}}{\partial z^2} - \frac{n^2}{c^2}\frac{\partial^2 \tilde{E}}{\partial t^2} = 0,$$

where the polarization is hidden in the refractive index n. In this representation, a dispersive medium with cubic nonlinearity is modeled by formulating the refractive index as $n(\omega, \tilde{E}) = n_0(\omega) + n_2 \tilde{E}^2$, which is a linear approximation of the refractive index as a function of intensity $\tilde{E}^2$. In this representation, the zeroth order term captures the frequency dependence of the medium and the first order term accounts for intensity dependence.

from that of the optical carrier wave may be written as

$$\begin{aligned}\tilde{P}(t,z) &= \int_{\mathbf{R}} \chi^{(1)}(t-s)\tilde{E}(s,z)\mathrm{d}s \\ &+ \int_{\mathbf{R}^3} \chi^{(3)}(t-s_1,t-s_2,t-s_3)\tilde{E}(s_1,z)\tilde{E}(s_2,z)\tilde{E}(s_3,z)\mathrm{d}s_1\mathrm{d}s_2\mathrm{d}s_3.\end{aligned} \tag{2.2}$$

The functions $\chi^{(1)}$ and $\chi^{(3)}$ are the linear and nonlinear susceptibilities, respectively, which represent the response of the medium to the electric field. The first convolution integral takes linear response of the medium into account, while the second convolution integral takes nonlinear response into account. There is no $\chi^{(2)}$ or any other "even" χ because the materials considered here display inversion symmetry and consequently do not respond to even powers of the electric field. The characteristic time of nonlinear response of silica is approximately 5fs (5×10^{-15}), which is much faster than the pulse durations considered here, which are more than 100fs. Thus the nonlinear response may be approximated by

$$\chi^{(3)}(t-s_1,t-s_2,t-s_3) \simeq \bar{\chi}^{(3)}\delta(t-s_1,t-s_2,t-s_3),$$

where

$$\bar{\chi}^{(3)} = \int_{\mathbf{R}^3} \chi^{(3)}(t-s_1,t-s_2,t-s_3)\mathrm{d}s_1\mathrm{d}s_2\mathrm{d}s_3.$$

This delta function approximation results in the following simplified expression for

the polarization:

$$\tilde{P}(t,z) = \int_{\mathbf{R}} \chi^{(1)}(t-s)\tilde{E}(s,z)\mathrm{d}s + \bar{\chi}^{(3)}\tilde{E}^3(t,z) \tag{2.3}$$

Using the Fourier transform pair

$$\tilde{E}(\omega,z) = \int_{\mathbf{R}} \tilde{E}(t,z)e^{i\omega t}\mathrm{d}t \quad \text{and} \quad \tilde{E}(t,z) = \frac{1}{2\pi}\int_{\mathbf{R}} \tilde{E}(\omega,z)e^{-i\omega t}\mathrm{d}\omega,$$

Equations 2.1 and 2.3 may be expressed in the frequency domain as

$$\left[\frac{\partial^2}{\partial z^2} + \frac{\omega^2}{c^2}\left(1-\chi^{(1)}\right)\right]\tilde{E} = -\frac{\omega^2\bar{\chi}^{(3)}}{c^2}\int_{\mathbf{R}^3}\tilde{E}_1\tilde{E}_2\tilde{E}_3\delta(\omega_1+\omega_2+\omega_3-\omega)\mathrm{d}\omega_1\mathrm{d}\omega_2\mathrm{d}\omega_3. \tag{2.4}$$

Here, $\tilde{E}_j = \tilde{E}(\omega_j, z)$. The goal is to model pulse propagation over perhaps thousands of kilometers, but the electric field $\tilde{E}$ captures every optical cycle, the length of which is on the order of a micron. Modeling a system with such a huge range of scales is a daunting task for researcher and computer alike, so this disparity of scales is reduced by applying a *slowly varying amplitude approximation*. In this approximation, the field is factored into a slowly-varying complex amplitude function E and a rapidly oscillating carrier wave. It is valid when the amplitude function varies much more slowly than the carrier wave so that

$$\left|\frac{\partial E}{\partial z}\right| \ll k_0|E| \quad \text{and} \quad \left|\frac{\partial E}{\partial t}\right| \ll \omega_0|E|, \tag{2.5}$$

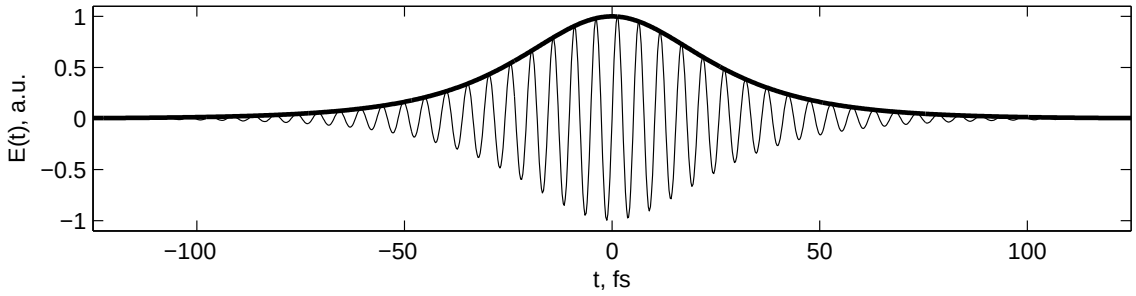

FIGURE 2.1. Separation of scales in the electric field (thin line) and its slowly varying amplitude (thick line) in an ultrashort ∼50fs pulse with a 1550nm carrier wave.

where k_0 and ω_0 are the respective wavenumber and angular frequency of the carrier wave. The electric field is written as

$$\tilde{E}(t,z) = E(t,z)\exp\big[i(k_0 z - \omega_0 t)\big] + \text{complex conjugate} \tag{2.6}$$

An illustration of this separation of scales appears in Figure 2.1 for an ultrashort pulse. By taking the Fourier transform of this factorization and inserting it into Equation 2.4, a bulky expression is obtained which may be simplified by making the *resonant approximation*. In this approximation, the exponentially small contributions of terms oscillating at frequencies other than the frequency of interest, which in this case is that of the carrier wave, are neglected. Thus only terms oscillating at $e^{ik_0 z}$ are

retained, obtaining

$$\left(\frac{\partial^2}{\partial z^2}+k^2(\omega)\right)\left(Ee^{ik_0z}\right)=-\frac{\omega^2\bar{\chi}^{(3)}}{c^2}e^{ik_0z}\int_{\mathbf{R}^3}(E_1^*E_2E_3+E_1E_2^*E_3+E_1E_2E_3^*)$$
$$\times\delta(\omega_1+\omega_2+\omega_3-\omega)\mathrm{d}\omega_1\mathrm{d}\omega_2\mathrm{d}\omega_3,$$

where the substitution $k(\omega)=\omega\sqrt{1-\chi^{(1)}}/c$ has been made. Expanding the right hand side of this equation and using Inequality 2.5 results in

$$\begin{aligned}\left(\frac{\partial^2}{\partial z^2}+k^2(\omega)\right)\left(Ee^{ik_0z}\right) &\simeq 2ik_0\frac{\partial E}{\partial z}+\left(k^2-k_0^2\right)E\\ &\simeq 2ik_0\frac{\partial E}{\partial z}+2k_0(k-k_0)E.\end{aligned}$$

The second approximation can be made since the wavenumbers contained in the pulse are very nearly the carrier wavenumber. Also neglected in this approximation is the influence of counterpropagating waves. Since the group velocity of optical waves is so high, the characteristic time of interaction of counterpropagating waves is much smaller than that of copropagating waves. This is the so-called *unidirectional wave approximation*. Now, using the relation $\omega^2\bar{\chi}^{(3)}/2c^2k_0\simeq\omega_0n_2/3c$, the frequency representation is

$$\left(i\frac{\partial}{\partial z}+k-k_0\right)E=-\frac{\omega_0n_2}{3c}\int_{\mathbf{R}^3}(E_1^*E_2E_3+E_1E_2^*E_3+E_1E_2E_3^*)$$
$$\times\delta(\omega_1+\omega_2+\omega_3-\omega)\mathrm{d}\omega_1\mathrm{d}\omega_2\mathrm{d}\omega_3. \qquad (2.7)$$

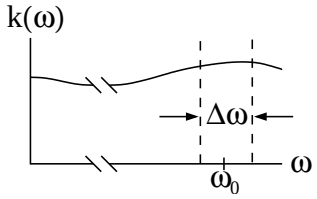

FIGURE 2.2. Schematic showing wavenumber as a function of frequency and the scale separation $\Delta\omega \ll \omega_0$.

Since the pulse duration is much longer than that of an optical cycle, the spectral width of the pulse is much smaller than the carrier frequency, as shown in Figure 2.2. This allows the linear dispersion relation $k(\omega)$ to be approximated using a second-order Taylor polynomial expanded about ω_0:

$$k(\omega) = k(\omega_0) + k'(\omega - \omega_0) + \frac{1}{2}k''(\omega - \omega_0)^2.$$

In this expression the primes denote differentiation with respect to ω and evaluation at ω_0. The last step is to take the inverse Fourier transform Equation 2.7 with respect to $\omega - \omega_0$. First for the right hand side:

$$\mathcal{F}^{-1}\left[i\frac{\partial E}{\partial z} + k'(\omega - \omega_0)E + \frac{1}{2}k''(\omega - \omega_0)^2 E\right] = \frac{i}{2\pi}\frac{\partial E}{\partial z} + \frac{ik'}{2\pi}\frac{\partial E}{\partial t} - \frac{k''}{4\pi}\frac{\partial^2 E}{\partial t^2}$$

The inverse Fourier transform of the left hand side of Equation 2.7 is

$$\frac{1}{2\pi}\int_{\mathbf{R}}\int_{\mathbf{R}^3}\left(E_1^*E_2E_3+E_1E_2^*E_3+E_1E_2E_3^*\right)\delta(\omega_1+\omega_2+\omega_3-\omega)$$
$$\times \mathrm{d}\omega_1\mathrm{d}\omega_2\mathrm{d}\omega_3 e^{-i(\omega-\omega_0)t}\mathrm{d}(\omega-\omega_0).$$

Consider the integral of the first product of amplitude functions

$$\begin{aligned}
&\frac{1}{2\pi}\int_{\mathbf{R}}\int_{\mathbf{R}^3} E_1^*E_2E_3\delta(\omega_1+\omega_2+\omega_3-\omega)\mathrm{d}\omega_1\mathrm{d}\omega_2\mathrm{d}\omega_3 e^{-i(\omega-\omega_0)t}\mathrm{d}(\omega-\omega_0)\\
&=\frac{1}{2\pi}\int_{\mathbf{R}^3} E_1^*E_2E_3\int_{\mathbf{R}}\delta(\omega_1+\omega_2+\omega_3-\omega)e^{-i(\omega-\omega_0)t}\mathrm{d}(\omega-\omega_0)\mathrm{d}\omega_1\mathrm{d}\omega_2\mathrm{d}\omega_3\\
&=\int_{\mathbf{R}^3} E^*(\omega_1-\omega_0)E(\omega_2+\omega_0)E(\omega_3+\omega_0)e^{-i(\omega_1+\omega_2+\omega_3-\omega_0)t}\mathrm{d}\omega_1\mathrm{d}\omega_2\mathrm{d}\omega_3\\
&=\int_{\mathbf{R}} E^*(\omega_1+\omega_0)e^{-i(\omega_1+\omega_0)t}\mathrm{d}\omega_1\int_{\mathbf{R}} E(\omega_2-\omega_0)e^{-i(\omega_2-\omega_0)t}\mathrm{d}\omega_2\\
&\times\int_{\mathbf{R}} E(\omega_3-\omega_0)e^{-i(\omega_3-\omega_0)t}\mathrm{d}\omega_3 = E^*E^2
\end{aligned}$$

The other two terms in the integral each make a similar contribution, resulting in the following time domain representation of Equation 2.7:

$$i\left(\frac{\partial}{\partial z}+k'\frac{\partial}{\partial t}\right)E-\frac{k''}{2}\frac{\partial^2 E}{\partial t^2}+\frac{\omega_0 n_2}{c}|E|^2E=0 \tag{2.8}$$

It is convenient to analyze the dynamics of pulse propagation in a reference frame which is traveling at the same speed as the pulse. In numeical simulations, for example, the copropagating frame allows the computational window to be made small

enough to contain only the pulse, which stays centered in the window. Without making this transformation the window would have to be large enough to view the pulse propagating across it. Moreover, other issues associated with advection problems arise such as limitations in step size. It is also convenient to work in dimensionless variables. To both of these ends, new variables are defined:

$$z = z_d\zeta - \tau_0\tau/k', \quad t = \tau_0\tau, \quad E = \sqrt{A_0}u.$$

Here the propagation distance is scaled by z_d, the characteristic dispersion length of the medium. This is the propagation distance required for dispersion to cause a pulse to broaden to approximately twice its initial width. It is also shifted by the amount required to transform to the copropagating reference frame. Time is scaled by the pulse duration τ_0 and the amplitude is scaled by the square root of the peak pulse amplitude A_0. This transformation results in the dimensionless equation

$$i\frac{\partial u}{\partial \zeta} + \frac{\partial^2 u}{\partial \tau^2} + \frac{z_d}{z_c}|u|^2 u = 0,$$

where the coefficient of the nonlinear term is the ratio of the characteristic dispersion length z_d to the characteristic cubic nonlinearity length z_c, which is the distance at which the phase rotation due to nonlinear self-phase modulation becomes $\mathcal{O}(1)$. These lengths may be related back to the original parameters appearing in the dimensional

equation through

$$z_d = 2\tau_0^2/|k''| \quad \text{and} \quad z_c = c/\omega_0 n_2 A_0.$$

The pulse peak power and width are control parameters which may be tuned. By fixing their relationship according to $A_0 = c|k''|/\omega_0 n_2 \tau_0^2$, the coefficient of the nonlinear term becomes 2 and the familiar form of the NLS equation is obtained:

$$i\frac{\partial u}{\partial \zeta} + \frac{\partial^2 u}{\partial \tau^2} + 2|u|^2 u = 0. \tag{2.9}$$

This equation is important not only because of its ubiquity in applied mathematics but also because it is integrable, and it also supports the uniquely robust soliton solutions. Unlike an ordinary solitary wave which may propagate without changing shape, solitons have the additional property of undergoing elastic collisions with one another. No energy is lost to continuous radiation during or after collisions. Solitons can be viewed a balance of forces acting on the propagation dynamics. The two forces acting on optical solitons are chromatic dispersion and nonlinearity. In the time domain, chromatic dispersion causes pulses to broaden as the propagate. This occurs because different frequency components of the pulse propagate at different velocities. The nonlinearity causes the electric field to concentrate in regions of higher refractive index. This happens because photons travel at the speed c/n, so they slow down as

the refractive index increases. Thus the number of photons per unit cross-sectional area (intensity) is larger when the refractive index is higher. The effect is nonlinear because it is the intensity itself which increases the refractive index.

The balance of forces has an interpretation in the frequency domain as well. Chromatic dispersion causes phase distortion among the frequency components of the pulse, and the self-phase modulation caused by the nonlinear term in NLS exactly compensates the dispersive phase distortion.

The integrability of NLS, as well as a general method for pulse solutions, was first obtained using the inverse scattering transform [11] in 1972. This involves writing NLS as a compatibility condition for the *Lax pair*, given by

$$\frac{\partial \hat{\psi}}{\partial \tau} = \hat{U}\hat{\psi} \tag{2.10}$$

$$\frac{\partial \hat{\psi}}{\partial \zeta} = \hat{V}\hat{\psi}, \tag{2.11}$$

where $\hat{\psi}$ and the potentials $\hat{U}$ and $\hat{V}$ are 2×2 matrices which depend on ζ, τ, and λ, the so-called spectral parameter. The compatibility condition for this linear system of equations is given by

$$\frac{\partial \hat{U}}{\partial \zeta} - \frac{\partial \hat{V}}{\partial \tau} + [\hat{U}, \hat{V}] = 0, \tag{2.12}$$

where the brackets indicate the commutator. This condition is equivalent to NLS if

$$\hat{U} = i(\lambda\hat{\sigma_3} + \hat{H}), \quad \hat{V} = 2\lambda\hat{U} + i\hat{F}$$

with

$$\hat{\sigma}_3 = \begin{pmatrix} 1 & 0 \\ 0 & -1 \end{pmatrix} \quad \hat{H} = \begin{pmatrix} 0 & r \\ q & 0 \end{pmatrix} \quad \hat{F} = \begin{pmatrix} -rq & -i\frac{\partial r}{\partial \tau} \\ i\frac{\partial q}{\partial \tau} & rq \end{pmatrix}.$$

for all λ. Inserting this form of the potentials $\hat{U}$ and $\hat{V}$ into the compatability condition (2.12) and setting $r = q^* = u$ produces Equation (2.9). The equation may be solved in the following way: The given initial pulse $u(\tau, \zeta = 0)$ is inserted into the potential $\hat{H}$, which is substituted into Equation (2.10). This spectral problem is solved for λ and the scattering data (reflection and transmission coefficients) is determined. Zakharov and Shabat showed that Equation (2.11) gives the evolution of the scattering data with respect to ζ. To reconstruct the potential according to the evolved scattering data, the inverse scattering problem must be solved, which presents as a system of linear integral equations [22] or can be reformulated as a Riemann-Hilbert problem [23, 24]. The solution of the integral equations yields the field for all ζ and τ.

NLS gives an excellent approximation of pulse dynamics for wavepackets as short as about 10ps. To model shorter pulses, some of the assumptions made in the deriva-

tion of NLS must be relaxed. Since the frequency spectrum of ultrashort pulses is broader, a second-degree Taylor polynomial is not a sufficiently accurate approximation of the linear dispersion relation. Including the third-degree term results in a more accurate model which retains a third-order dispersion term proportional to $iu_{\tau\tau\tau}$ on the right hand side of Equation (2.9).

The broader frequency spectrum of ultrashort pulses also has an effect on the transverse mode profile, since it varies as a function of frequency. This effect may be modeled by incorporating the frequency dependence of $\chi^{(3)}$ (or n_2). A linear approximation of this dependence results in the NLS correction term $-i(|u|^2u)_\tau$. This effect leads to the development of steep fronts in optical pulses and is known as optical shocking or self-steepening.

The nonlinear response time of SiO_2 is about 5fs. When pulse duration is no longer well separated from this characteristic time, nonlinear delay effects (namely stimulated Raman scattering) must be taken into account. In this regime, the δ-function approximation of $\chi^{(3)}$ is not valid and must be relaxed. As a result, the Raman delay term $|u|^2_\tau u$ is retained in NLS.

As pulse durations decrease, their peak power must increase to ensure that the pulses contain enough energy to be detected at the receiver. High power effects are captured by retaining an additional term in the expansion of the intensity-dependent refractive index, or equivalently, including the $\chi^{(5)}$ response of the material. This results in the retention of a quintic nonlinear term $|u|^4u$ in NLS.

Including all these effects results in the so-called short pulse equation

$$i\frac{\partial u}{\partial \zeta} + \frac{\partial^2 u}{\partial \tau^2} + 2|u|^2 u = ia\frac{\partial^3 u}{\partial \tau^3} - ib\frac{\partial}{\partial \tau}\big(|u|^2 u\big) + cu\frac{\partial}{\partial \tau}\big(|u|^2\big) + d|u|^4 u,$$

with real positive constants a, b, c, and d. This equation is valid for pulse durations down to about 50fs at carrier wavelength 1550nm. In the regime of interest here, for which pulse durations are about one picosecond, not all of these correction terms need to be included. System parameters may be chosen so that only one of these terms need be included, which allows the effects of each term to be considered separately. Since the effect under consideration is small in the chosen parameter regime, a perturbation method may be used in its analysis based on the exact soliton solution of NLS. Over the years, many perturbation techniques have been proposed, but only one provides a quantitative description of the radiation effects of pulses propagating in the presence of these high-order contributions. This technique is detailed in the following section.

2.2 A soliton perturbation technique

As discussed in the preceeding section, generalizations of the NLS description of pulse propagation result in equations of the form

$$i\frac{\partial u}{\partial z} + \frac{\partial^2 u}{\partial t} + 2|u|^2 u = \epsilon f(u). \tag{2.13}$$

The form of the function $f(u)$ depends on how the model is generalized. The meaning of the parameter ϵ varies according to which perturbation effect is under consideration, but in this analysis it is assumed to be positive and small, i.e. $0 < \epsilon \ll 1$, since only the onset of one of these high-order effects is considered.

The general form of the fundamental soliton solution of NLS is given by

$$u_\beta(t, z) = \eta_\beta \operatorname{sech}(x_\beta) \exp(i\chi_\beta), \tag{2.14}$$

with

$$x_\beta = \eta_\beta(t - y_\beta - 2\beta z), \quad \chi_\beta = \alpha_\beta + \beta(t - y_\beta) + (\eta_\beta^2 - \beta^2)z. \tag{2.15}$$

This solution is characterized by four parameters, α, y, β, and η, corresponding to phase, position, frequency and amplitude, respectively. The frequency β also plays the roles of velocity and a correction to the wavenumber, while the amplitude η also determines pulse width and contributes to the wavenumber.

Without loss of generality, the parameters are assumed to have the values $\alpha = y = \beta = 0$ and $\eta = 1$ in this analysis. The following calculations are uneffected by arbitrary parameter values modulo some additional bulk in the expressions. The general form of a stationary solution to Equation (2.13) is $u(t, z) = u(t) \exp(iz)$. This

substitution obtains the ordinary differential equation

$$u'' - u + 2|u|^2 u = \epsilon f(u), \quad u \in L^2(\mathbf{R}) \tag{2.16}$$

where primes denote differentiation with respect to t. Since the parameter ϵ is small, a regular perturbation series $u(t) = u_0(t) + u_1(t) + u_2(t)$, where $u_n(t) = \mathcal{O}(\epsilon^n)$, is used to obtain linear equations in successive orders of ϵ for each unknown function $u_n(t)$:

$$u_0'' - u_0 + 2|u_0|^2 u_0 = 0 \tag{2.17}$$

$$u_1'' - u_1 + 2(2|u_0|^2 u_1 + u_0^2 u_1^*) = f(u_0) \tag{2.18}$$

$$u_2'' - u_2 + 2(2|u_0|^2 u_2 + u_0^2 u_2^*) = -2\left(2u_0|u_1|^2 + u_0^* u_1^2\right) + u_1 \, f_u|_{u_1} . \tag{2.19}$$

The nontrivial solutions to Equation (2.17) is $u_0(t) = \pm\mathrm{sech}\,(t)$. Since the only observable quantity is the square modulus of this function, the sign is an arbitrary choice and the positive is selected. The equations for higher-order corrections can now be written in the general form

$$v'' - v + 2\,\mathrm{sech}^{\,2} t(2v + v^*) = g(t), \tag{2.20}$$

This equation may be closed by combining it with its negative complex conjugate,

resulting in

$$\hat{L}\mathbf{v} = \mathbf{g}, \tag{2.21}$$

where $\mathbf{v} = (v, v^*)^T$, $\mathbf{g} = (g, -g^*)^T$, and the linear operator is given by

$$\hat{L} = \left(\frac{\mathrm{d}^2}{\mathrm{d}t^2} - 1\right)\hat{\sigma}_3 + \frac{2}{\cosh^2 t}\left(2\hat{\sigma}_3 + i\hat{\sigma}_2\right) \tag{2.22}$$

and $\hat{\sigma}_j$ are Pauli matrices. The reason for writing the problem in this form is that $\hat{L}$ is self-adjoint, so it has a complete set of orthogonal eigenfunctions. This means that Equation (2.21) can be solved by expanding both the unknown and right-hand side functions in a basis of eigenfunctions of the operator $\hat{L}$ and using the orthogonality condition to determine the unknown coefficeints. The basis consists of four discrete or "soft" modes and two continuous modes [25]:

$$\mathbf{0} = \frac{1}{\cosh t}\begin{pmatrix} 1 \\ -1 \end{pmatrix} \qquad \mathbf{1} = \frac{\tanh t}{\cosh t}\begin{pmatrix} 1 \\ 1 \end{pmatrix}$$

$$\mathbf{2} = \frac{t}{\cosh t}\begin{pmatrix} 1 \\ -1 \end{pmatrix} \qquad \mathbf{3} = \frac{t\tanh t - 1}{\cosh t}\begin{pmatrix} 1 \\ 1 \end{pmatrix}$$

$$\mathbf{k} = e^{ikt}\left[1 - \frac{2ike^{-t}}{(k+i)^2\cosh t}\right]\begin{pmatrix} 0 \\ 1 \end{pmatrix} + \frac{e^{ikt}}{(k+i)^2\cosh^2 t}\begin{pmatrix} 1 \\ 1 \end{pmatrix}$$

$$\bar{\mathbf{k}} = e^{-ikt}\left[1 + \frac{2ike^{-t}}{(k-i)^2\cosh t}\right]\begin{pmatrix} 1 \\ 0 \end{pmatrix} + \frac{e^{-ikt}}{(k-i)^2\cosh^2 t}\begin{pmatrix} 1 \\ 1 \end{pmatrix}$$

Here k is a continuous index which varies over the real line. The orthogonality conditions are

$$\langle \mathbf{0}|\hat{\sigma}_3|\mathbf{3}\rangle = -2 \qquad \langle \mathbf{1}|\hat{\sigma}_3|\mathbf{2}\rangle = 2$$

$$\langle \mathbf{k}|\hat{\sigma}_3|\mathbf{k}\rangle = -1 \qquad \langle \bar{\mathbf{k}}|\hat{\sigma}_3|\bar{\mathbf{k}}\rangle = -1$$

All other inner products are zero. The inner product is defined as

$$\langle \mathbf{i}|\hat{\sigma}_3|\mathbf{j}\rangle = \int_{\mathbf{R}} \mathbf{i}^*(t)\hat{\sigma}_3\mathbf{j}(t)\mathrm{d}t,$$

where the * refers to Hermitian conjugation. The soft modes correspond to the discrete spectrum of the operator and the unlocalized modes correspond to the continuous spectrum. These eigenfunctions obey the relations

$$\begin{aligned} \hat{L}\mathbf{0} = 0 \qquad & \hat{L}\mathbf{1} = 0 \\ \hat{L}\mathbf{2} = -2\mathbf{1} \qquad & \hat{L}\mathbf{3} = -2\mathbf{0} \\ \hat{L}\mathbf{k} = (k^2+1)\mathbf{k} \qquad & \hat{L}\bar{\mathbf{k}} = -(k^2+1)\bar{\mathbf{k}}. \end{aligned} \tag{2.23}$$

The Fredholm Alternative guarantees the existence of a solution of Equation (2.21) when the kernel of the adjoint operator is orthogonal to the right-hand side of the original problem. Since $\hat{L}$ is self-adjoint, Equations (2.23) indicate that $Ker(\hat{L})$ is

spanned by **0** and **1**. Thus the necessary condition for solubility of Equation (2.21) is

$$\langle \mathbf{0}|\hat{\sigma}_3|\mathbf{g}\rangle = 0 = \langle \mathbf{1}|\hat{\sigma}_3|\mathbf{g}\rangle \,. \tag{2.24}$$

The soft modes are related to the four parameters which characterize the fundamental soliton solution of NLS. This may be seen by considering a change in each of the parameters which characterize the fundamental solution (2.14) and (2.15). Differentiating with respect to each parameter obains expressions which, after the assumptions of this construction are substituted, obtains

$$\begin{aligned}
\frac{\partial}{\partial\alpha}\begin{pmatrix} u \\ u^* \end{pmatrix} &= i\begin{pmatrix} u \\ -u^* \end{pmatrix} = i\mathbf{0} \\
\frac{\partial}{\partial y}\begin{pmatrix} u \\ u^* \end{pmatrix} &= \tanh t\begin{pmatrix} u \\ u^* \end{pmatrix} = \mathbf{1} \\
\frac{\partial}{\partial\beta}\begin{pmatrix} u \\ u^* \end{pmatrix} &= it\begin{pmatrix} u \\ -u^* \end{pmatrix} = i\mathbf{2} \\
\frac{\partial}{\partial\eta}\begin{pmatrix} u \\ u^* \end{pmatrix} &= (1 - t\tanh t)\begin{pmatrix} u \\ u^* \end{pmatrix} = -\mathbf{3}.
\end{aligned}$$

Those assumptions are that there is no z dependence on these parameters and the values $\alpha = y = \beta = 0$ and $\eta = 1$ are fixed[2]. This establishes the relationship between

[2]Relaxing the fixed parameter assumption results in the more general relations

$$\frac{\partial \mathbf{u}}{\partial\alpha} = i\eta\mathbf{0}, \quad \frac{\partial \mathbf{u}}{\partial y} = \eta^2\mathbf{1}, \quad \frac{\partial \mathbf{u}}{\partial\beta} = i\mathbf{2}, \quad \frac{\partial \mathbf{u}}{\partial\eta} = -\mathbf{3} \tag{2.25}$$

the soft modes and the soliton parameters.

Now that all the machinery is in place, Equation (2.21) may be solved. Both the unknown and right-hand side functions $\mathbf{v}$ and $\mathbf{g}$ are expanded in a basis of eigenfunctions of $\hat{L}$:

$$\mathbf{g}(t) = \sum_{\mathbf{j=0}}^{\mathbf{3}} g_j \mathbf{j}(t) + \frac{1}{2\pi} \int_{\mathbf{R}} \left[g_k \mathbf{k}(t) + g_k^* \bar{\mathbf{k}}(t) \right] \mathrm{d}k$$
$$\mathbf{v}(t) = \sum_{\mathbf{j=0}}^{\mathbf{3}} v_j \mathbf{j}(t) + \frac{1}{2\pi} \int_{\mathbf{R}} \left[v_k \mathbf{k}(t) + v_k^* \bar{\mathbf{k}}(t) \right] \mathrm{d}k$$

Using the orthogonality conditions, the expansion coefficients for the right-hand side function are

$$g_0 = \langle \mathbf{3} | \hat{\sigma}_3 | \mathbf{g} \rangle \quad g_1 = \langle \mathbf{2} | \hat{\sigma}_3 | \mathbf{g} \rangle \quad g_2 = \langle \mathbf{1} | \hat{\sigma}_3 | \mathbf{g} \rangle$$
$$g_3 = \langle \mathbf{0} | \hat{\sigma}_3 | \mathbf{g} \rangle \quad g_k = \langle \mathbf{k} | \hat{\sigma}_3 | \mathbf{g} \rangle \,.$$

Applying $\hat{L}$ to the expansion of $\mathbf{v}$ yields

$$\hat{L}\mathbf{v}(t) = -2v_2 \mathbf{1}(t) - 2v_3 \mathbf{0}(t) + \frac{1}{2\pi} \int_{\mathbf{R}} \left[(k^2+1) v_k \mathbf{k}(t) - (k_2+1) v_k^* \bar{\mathbf{k}}(t) \right] \mathrm{d}k.$$

Now equating the expansions of $\hat{L}\mathbf{v}$ and $\mathbf{g}$ results in

$$
\begin{aligned}
&v_0,\ v_1 \text{ arbitrary} \\
&v_2 = -\tfrac{1}{2}\langle \mathbf{2}|\hat{\sigma}_3|\mathbf{g}\rangle \\
&v_3 = -\tfrac{1}{2}\langle \mathbf{3}|\hat{\sigma}_3|\mathbf{g}\rangle \\
&v_k = \langle \mathbf{k}|\hat{\sigma}_3|\mathbf{g}\rangle / (k^2+1)
\end{aligned}
$$

and by choosing $v_0 = 0 = v_1$, the solution may be written

$$
\begin{aligned}
\mathbf{v}(t) = &-\tfrac{1}{2}\langle \mathbf{2}|\hat{\sigma}_3|\mathbf{g}\rangle\, \mathbf{2}(t) - \tfrac{1}{2}\langle \mathbf{3}|\hat{\sigma}_3|\mathbf{g}\rangle\, \mathbf{3}(t) \\
&+\frac{1}{2\pi}\int_{\mathbf{R}} \left[\frac{\langle \mathbf{k}|\hat{\sigma}_3|\mathbf{g}\rangle}{k^2+1}\mathbf{k}(t) + \frac{\langle \mathbf{k}|\hat{\sigma}_3|\mathbf{g}\rangle^*}{k^2+1}\bar{\mathbf{k}}(t) \right] \mathrm{d}k.
\end{aligned}
$$

Since $\mathbf{v}$ is a linear combination of $\mathbf{2}$, $\mathbf{3}$, $\mathbf{k}$, and $\bar{\mathbf{k}}$, this form represents shifts in the frequency and amplitude of the soliton as well as the unlocalized radiation emitted, represented by the integral term.

2.2.1 Application: stationary solutions

The presence of the perturbations $\epsilon f(u)$ upsets the balance between energy confinement and dispersion which makes solitons so robust. But it is still possible that stationary solutions of perturbed NLS exist as a result of a three-way balance. The subject of this section is the application of the soliton perturbation technique to find-

ing approximations of stationary solutions. The term *stationary solution* implies that the amplitude of the solution does not change with propagation distance z. It can be shown that a pulse which is not exactly stationary evolves into the stationary form after a transient [26, 27]. In the transient distance, the pulse sheds radiation and adjusts its parameters until the stationary form is realized. The transient distance may be reduced by shaping the initial pulse closer to its stationary form, whereupon propagating it emits less radiation, enabling the transmission of stationary solutions over greater distances than standard NLS solitons in the presence of high-order corrections.

In the following analyses, the individual perturbation terms are examined and approximations to the stationary solutions of their corresponding equations are obtained. In the case of the TOD perturbation $f(u) = iu_{ttt}$ [27], Equation (2.18) becomes

$$u_1'' - u_1 + 2\,\mathrm{sech}^{\,2}t(2u_1 + u_1^*) = i\epsilon\,\mathrm{sech}\;t\left(\mathrm{sech}^{\,2}t - \tanh^2 t\right).$$

Applying the techniques described in this section results in the solution

$$\mathbf{u}_1(t) = -\frac{i\epsilon}{2}\left\{\mathbf{2}(t) + \begin{pmatrix} 1 \\ -1 \end{pmatrix}\int_{\mathbf{R}} \frac{k[k\cos(kt)\tanh t + \frac{1}{2}(k^2-1)\sin(kt)]}{(k^2+1)\cosh(\frac{\pi}{2}k)}\mathrm{d}k\right\}.$$

This form shows that in $\mathcal{O}(\epsilon)$ of the perturbation theory, corrections are made to

the soliton frequency and emitted radiation. This is because the solution is a linear combination of **2** and an integral term. This equation actually has the closed-form solution

$$u_1(t) = \tfrac{1}{2} i\epsilon \text{ sech } t(t - 3\tanh t)$$

which allows Equation (2.19) to be written

$$\begin{aligned} & u_2'' - u_2 + 2\,\text{sech}^{\,2} t(2u_2 + u_2^*) \\ & = -\tfrac{1}{2}\epsilon^2 \left[63\,\text{sech}^{\,5} t + (t^2 - 57)\,\text{sech}^{\,3} t + (6 - t\tanh t)\,\text{sech } t\right] \end{aligned} \tag{2.26}$$

At the time of this writing, a closed-form solution of this equation is unknown. Applying the eigenfunction expansion method obtains the following solution:

$$\mathbf{u}_2 = \frac{\epsilon^2(54 + \pi^2)}{48}\mathbf{3}(t) + \frac{\epsilon^2}{2\pi}\int_{\mathbf{R}} \left[\frac{\langle \mathbf{k}|\hat{\sigma}_3|\mathbf{u}_1\rangle}{k^2+1}\mathbf{k}(t) - \frac{\langle \mathbf{k}|\hat{\sigma}_3|\mathbf{u}_1\rangle^*}{k^2+1}\bar{\mathbf{k}}(t)\right] \mathrm{d}k.$$

The integrals in this expression can only be calculated numerically, so obtaining solutions to Equation (2.26) is simpler and computationally cheaper using a finite difference scheme. However, this expression reveals that in $\mathcal{O}(\epsilon^2)$ of the perturbation theory, corrections are made to amplitude and radiation. Full numerical simulations of the dynamical equation [27] show that this stationary solution reduces walk-off and radiation emission by a factor of ϵ^2 over the soliton solution. The first- and

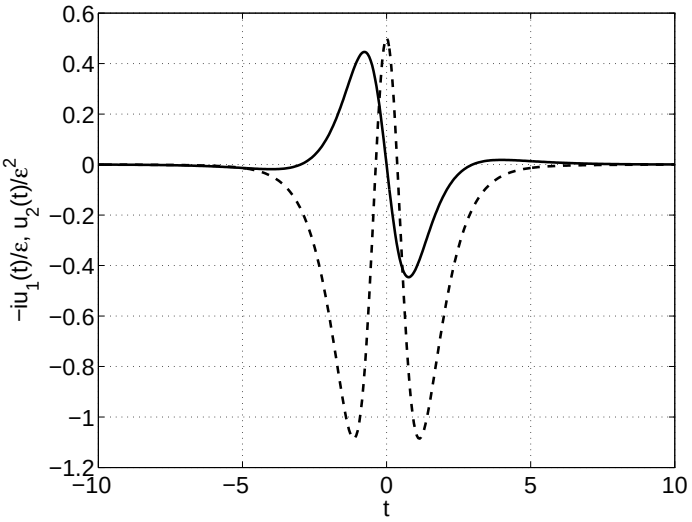

FIGURE 2.3. First- and second-order corrections to the stationary solution of NLS in the presence of weak third-order dispersion, represented by solid and dashed lines, respectively.

second-order corrections are shown in Figure 2.3.

In the case of the self-steepening perturbation $f(u) = -i(|u|^2u)_t$, closed-form solutions are available for both the first- and second-order corrections. Thus a second-order approximation to the stationary solution is

$$u_s(t) = \text{sech } t - \tfrac{3i}{4}\epsilon \,\text{sech } t \tanh t + \epsilon^2 \text{sech } t \left(\tfrac{5}{16}\,\text{sech}^2 t - \tfrac{11}{32}\right).$$

Closed-form corrections are also available for case of the quintic nonlinearity per-

turbation $f(u) = |u|^4 u$. The approximation to its stationary solution is given by

$$u_q(t) = \text{sech } t + \tfrac{1}{6}\epsilon(1 - \tanh^2 t)\,\text{sech } t \\ +\epsilon^2 \text{sech } t \left(\tfrac{5}{18} - \tfrac{2}{9}\,\text{sech}^2 t + \tfrac{1}{24}\,\text{sech}^4 t\right). \tag{2.27}$$

This expression will be useful in Section 2.6 where the effects of quintic nonlinearity on soliton collisions are studied.

Finally, let us examine stationary solutions to NLS in the presence of stimulated Raman scattering. In this case $f(u) = (|u|^2)_t u$ and the right-hand side of Equation (2.20) is given by

$$\mathbf{g}(t) = -\frac{2\tanh t}{\cosh^3 t}\begin{pmatrix} 1 \\ -1 \end{pmatrix}.$$

This perturbation causes the center frequency of solitons to shift, and since the frequency parameter also plays the role of velocity, this frequency shift causes pulses to change velocity. Therefore it is worthwhile to ask if stationary solutions even exist in the presence of this perturbation. The solubility condition (2.24) provides us with the answer. Since $\mathbf{g}$ is odd and $\mathbf{0}$ is even, their product is an odd function which is integrated over a symmetric interval, so the first condition in Equation (2.24) is satisfied. However, $\langle \mathbf{1}|\hat{\sigma}_3|\mathbf{g}\rangle = -\frac{16}{15} \neq 0$ so a correction that reduces the change in frequency due to stimulated Raman scattering does not exist.

2.3 Double perturbation theory for collision problems

As discussed at the beginning of this chapter, there are two ways of utilizing the huge bandwidth available with optical fibers: using ultrashort pulses as bit carriers and partitioning the bandwidth for use in multichannel communication, also known as wavelength division multiplexing (WDM). For pulses longer than about 10ps, solitons may be used as bit carriers and interchannel collisions between solitons are elastic, that is, no radiation is emitted when collisions take place. In addition, the amplitude, frequency, and shape of the solitons are not changed by the collisions. The only two effects of a soliton collision are a phase shift proportional to $1/|\beta|$, and a position shift proportional to $1/(|\beta|\beta)$, where β is the frequency difference between adjacent channels. But as the bit rate in each channel increases, pulse duration must decrease and the elastic nature of soliton collisions breaks down due to the influence of high-order effects. The consequences of this inelasticity can have malign effects on system performance; therefore it is important to account for the intensity of the emitted radiation and the shift in the pulse parameters induced by these inelastic collisions.

Optical soliton propagation is described by the ideal NLS equation $\big($"ideal NLS" refers to Equation (2.13) with $\epsilon = 0\big)$ in multichannel systems as well as single channel systems [20, 28, 29]. Interchannel collisions [30, 31] between solitons of ideal NLS have been studied in detail and are well understood. Because of the difficulty of developing a complete perturbation theory around the two soliton solution of ideal

NLS, a full description of the effects of high-order terms on interchannel optical soliton collisions remains elusive. Thus perturbation techniques must be built around single soliton solutions.

In this section a perturbation theory in two small parameters [32, 33] is developed which describes the effects of high-order corrections on optical soliton collisions. It is built upon the results discussed in the previous section. In this procedure, two stationary pulses, propagating with different group velocities, are used as the initial condition for the collision problem. Thus, the effects of radiation emission and changes in the parameters of the pulses are only due to the collision itself (and not due to single pulse propagation). The effects of the collision are calculated using a double perturbation expansion in two small parameters, the coefficient of the correction term ϵ and the reciprocal of the interchannel frequency difference $1/\beta$. The assumption on the second channel is $|\beta| \gg 1$, a condition that is usually satisfied in fiber optic communication systems even for neighboring channels [34, 35].

This perturbation procedure is used to determine the intensity and dynamics of collision-induced emitted radiation. Even though the cumulative effect of radiation emission due to many interchannel collisions is potentially dangerous for long haul soliton transmission [32, 33], this aspect has been largely ignored in most perturbative descriptions of optical soliton collisions. The few works that attempted to address radiation emission in interchannel soliton collisions did not present any comparison of the theoretical predictions with results from numerical simulations [36, 37]. Moreover,

a detailed analysis of data obtained from numerics (or experiments) for the effects of radiation emission in interchannel collisions between optical solitons, including comparison with theoretical predictions, has never been performed. Indeed, in order to measure the collision-induced emitted radiation numerically (or experimentally), the effects of radiation emitted due to single pulse propagation must be completely eliminated. While this is impossible in the framework of the perturbative description presented in Refs. [36, 37], it is automatically guaranteed in the framework of the new perturbation procedure [32, 33], by using the sum of two well separated *stationary pulses* as the initial condition.

The ansatz for a two soliton solution of Equation (2.13) is [32, 33]

$$u = \psi_0 + \psi_\beta + \phi, \tag{2.28}$$

where ψ_0 and ψ_β are stationary single pulse solutions of Equation (2.13) with $0 < \epsilon \ll 1$ in channels 0 and β, respectively. For simplicity, and without loss of generality, one of the two channels is chosen as the reference channel with $\beta = 0$. Here $\phi = \phi(t, z)$ is an $\mathcal{O}(\epsilon)$ correction to these solutions, resulting solely from collision effects. In analogy with the ideal collision case ϕ may be represented as the sum

$$\phi = \phi_0 + \phi_\beta + \ldots, \tag{2.29}$$

where ϕ_0 and ϕ_β stand for collision induced effects in channels 0 and β. The ellipsis represents higher order terms in other channels such as $-\beta$ and 2β which make exponentially small contributions. To calculate the collision induced effects on the stationary pulse in the reference channel, (2.28) and (2.29) are substituted into Equation (2.13) and only terms up to first order in the two small parameters are retained. This approximation allows the calculation of collision effects up to second order with respect to both $1/\beta$ and ϵ. Since ϕ_0 oscillates at the same frequency as ψ_0, and since $|\beta| \gg 1$, the resonant approximation is employed and the exponentially small contributions from rapidly oscillating terms are neglected. The dynamics of ϕ_0 are then described by:

$$\begin{aligned} & i\frac{\partial \phi_0}{\partial z} + \frac{\partial^2 \phi_0}{\partial t^2} + 4|\psi_0|^2\phi_0 + 2\psi_0^2\phi_0^* \\ & \quad = -4|\psi_\beta|^2\psi_0 - 4|\psi_\beta|^2\phi_0 - 4\left(\psi_\beta\phi_\beta^* + \psi_\beta^*\phi_\beta\right)\psi_0 + \epsilon F(\psi_0, \psi_\beta), \end{aligned} \tag{2.30}$$

where $F(\psi_0, \psi_\beta)$ contains the interaction terms of the linearization of $f(\psi_0 + \psi_\beta + \phi_0 + \phi_\beta)$ with respect to $1/\beta$ and ϵ. The factorizations

$$\psi_0(t,z) = \Psi_0(x_0)\exp(i\chi_0), \qquad \phi_0(t,z) = \Phi_0(x_0)\exp(i\chi_0),$$

$$\psi_\beta(t,z) = \Psi_\beta(x_\beta)\exp(i\chi_\beta), \qquad \phi_\beta(t,z) = \Phi_\beta(x_\beta)\exp(i\chi_\beta)$$

are substituted into Equation (2.30), where x and χ are defined by Equations (2.15)[3]. This yields

$$\frac{\partial \Phi_0}{\partial z} - i\left[\left(\frac{\partial^2}{\partial t^2} - \eta_0^2\right)\Phi_0 + 4|\Psi_0|^2\Phi_0 + 2\Psi_0^2\Phi_0^*\right] = 4i\left[|\Psi_\beta|^2\Psi_0 + |\Psi_\beta|^2\Phi_0 + \left(\Psi_\beta\Phi_\beta^* + \Psi_\beta^*\Phi_\beta\right)\Psi_0\right] - i\epsilon F(\Psi_0, \Psi_\beta). \quad (2.31)$$

Three different regions in z are naturally separated. The first one is the collision region, which is the small interval $[z_0 - \tilde{z}/|\beta|, z_0 + \tilde{z}/|\beta|]$ in the vicinity of the collision point z_0, where $|\beta| \gg \tilde{z} \gg 1$. In the collision region Φ_0 acquires a fast change in z. Therefore, in this region the $4i|\Psi_\beta|^2\Psi_0$ term gives the leading contribution to Φ_0. In higher orders of the perturbation theory, one has to take into account interaction terms coming from $F(\Psi_0, \Psi_\beta)$. In the pre- and post-collision regions, $z < z_0 - \tilde{z}/|\beta|$ and $z > z_0 + \tilde{z}/|\beta|$, respectively, the interaction between the two solitons is exponentially small, so the term $4i|\Psi_\beta|^2\Psi_0$ and all other interaction terms can be neglected. Thus, these two regions correspond to free propagation of the stationary pulse before and after the collision.

The correction ϕ_0 and the complete solution $\psi_0^{total} = \psi_0 + \phi_0$ are obtained in the

[3]If effects in the β-channel are being calculated, x_β and χ_β are not as simple as in Equation (2.30). They need to be modified to account for the correction term. In the case of third-order dispersion [32], $x_\beta = \eta_\beta(1+3\epsilon\beta)^{-1/2}[t - y_\beta - 2\beta(1+3\epsilon\beta/2)z]$ and $\chi_\beta = \alpha_\beta + \beta(t - y_\beta) + [\eta_\beta^2 - \beta^2(1+\epsilon\beta)]z$. For self-steepening, $x_\beta = \eta_\beta(1 - \epsilon\beta/2)(t - y_\beta - 2\beta z)$ and $\chi_\beta = \alpha_\beta + \beta(t - y_\beta) + [(1 - \epsilon\beta/2)\eta_\beta^2 - \beta^2]z$.

form of a perturbation series. That is, in the collision region one substitutes

$$\Phi_0(x_0, z) = \Phi_{01}^{(0)}(x_0, z) + \Phi_{01}^{(1)}(x_0, z) + \Phi_{02}^{(0)}(x_0, z) + \Phi_{02}^{(1)}(x_0, z) + \dots , \tag{2.32}$$

$$\Psi_0(x_0) = \Psi_{00}(x_0) + \Psi_{01}(x_0) + \dots , \tag{2.33}$$

and

$$\psi_\beta(x_\beta, z) = e^{i\chi_\beta} \left[\Psi_{\beta 0}(x_\beta) + \Psi_{\beta 1}(x_\beta) + \dots\right] \tag{2.34}$$

into Eq. (2.31), and linearizes the result with respect to the two small parameters. In Eq. (2.32) the first subscript in $\Phi_{01}^{(0)}$, for example, stands for the channel, the second subscript indicates the combined order with respect to both ϵ and $1/\beta$, and the superscript represents the order in ϵ. Thus, $\Phi_{01}^{(0)}$ is the $\mathcal{O}(1/\beta)$ collision-induced correction in the reference channel. The stationary zero order terms Ψ_{00} and $\Psi_{\beta 0}$ in the expansions (2.33) and (2.34) correspond to the ideal soliton given by

$$\Psi_{\beta 0} = \frac{\eta_\beta}{\cosh x_\beta} \tag{2.35}$$

The stationary correction terms $\tilde{\Psi}_{01}$ and $\tilde{\Psi}_{\beta 1}$ are $\mathcal{O}(\epsilon)$ and may be obtained through the methods in Section 2.3.

In the free propagation region, one substitutes $\psi_0^{total} = \exp(i\chi_0)(\Psi_0 + \Phi_0)$ into Eq. (2.13) and linearizes with respect to ϵ and $1/\beta$. To analyze the free propagation of Φ_0 after the collision one needs to project Φ_0 onto the set of eigenfunctions of the linear

operator $\hat{L}$, defined by Equation (2.22).

2.3.1 Collision effects in $\mathcal{O}(1/\beta)$

Here the collision induced effects in order $1/\beta$ of the perturbation theory are determined. Inserting Equations (2.32) and (2.33) into Equation (2.31) and collecting the $\mathcal{O}(1/\beta)$ terms results in

$$\frac{\partial \Phi_{01}^{(0)}}{\partial z} = 4i|\Psi_{\beta 0}|^2 \Psi_{00}.$$

The right hand side is given by Equation (2.35), so this expression may be integrated to determine the collision-induced effects in this order as a function of z:

$$\begin{aligned} \Phi_{01}^{(0)}(t,z) - \Phi_{01}^{(0)}(t,-\infty) &= \frac{4i\eta_\beta^2 \eta_0}{\cosh\left[\eta_0\left(t-y_0\right)\right]} \int_{-\infty}^{z} \frac{\mathrm{d}z'}{\cosh^2\left[\eta_\beta\left(t-y_\beta-2\beta z'\right)\right]} \\ &= \frac{2i\eta_\beta \eta_0}{\beta \cosh x_0}\left(1-\tanh x_\beta\right). \end{aligned}$$

It stands to reason that no collision-induced effects are present before the collision, so $\Phi_{01}^{(0)}(t,-\infty) = 0$. Using this initial condition, the total effect of the collision is obtained by taking the limit of this expression as $z \to \infty$:

$$\Delta\Phi_{01}^{(0)} = \frac{4i\eta_0\eta_\beta}{|\beta|\cosh x_0},$$

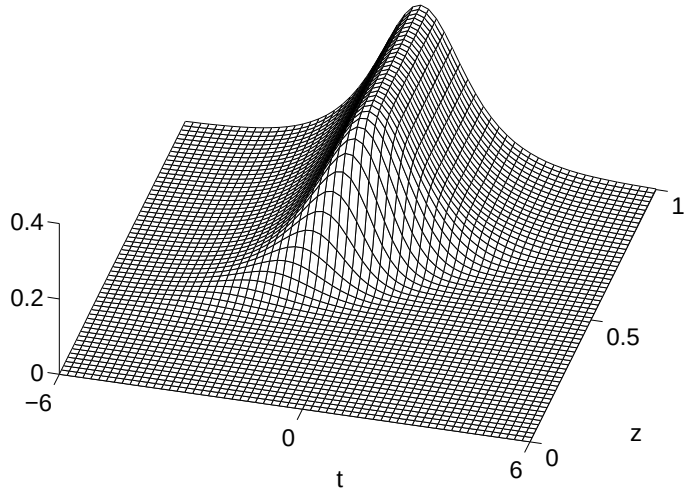

FIGURE 2.4. The collision-induced effects in $\mathcal{O}(1/\beta)$ given by $\Phi_{01}^{(0)}(t,z)$ (the imaginary part of which is shown here) with parameter values $\eta_0 = 1 = \eta_\beta$, $\beta = 10$, $y_0 = 0$, and $y_\beta = -10$. This corresponds to the a collision in which the β-channel pulse approaches the collision point $z_0 = 1/2$ from the right, or $-t$ direction.

where the absolute value is due to the invariance of the sign of β. The z-evolution of $\Phi_{01}^{(0)}$ is shown in Figure 2.4. Note that $\Phi_{01}^{(0)}$ changes rapidly in the vicinity of the collision and reaches a steady-state $\operatorname{sech} x_0$ profile quickly thereafter. Also note the asymmetry in the t-direction at the beginning of the collision region, which is due to the direction from which the β-channel pulse approaches.

However, taking $\Phi_{01}^{(0)}(t,-\infty) = 0$ makes the following analysis more complicated than necessary. This complication can be avoided by preparing the solitons with an initial phase shift which manifests as

$$\Phi_{01}^{(0)}(t,-\infty) = -\frac{2i\eta_\beta\eta_0}{\beta\cosh x_0}.$$

This represents an initial phase shift because its spinor form $(\Phi_{01}^{(0)}, \Phi_{01}^{(0)*})^T$ is proportional to the zeroth eigenfunction of $\hat{L}$. Using this initial condition results in a simpler expression for the z-dependent effects of the collision:

$$\Phi_{01}^{(0)}(t,z) = -\frac{2i\eta_\beta\eta_0 \tanh x_\beta}{\beta \cosh x_0}$$

Under this assumption, the total effect of the collision is obtained by taking the difference of this expression as $z \to \pm\infty$, which gives the same result as Equation (2.36). The collision-induced effects in this order are given by writing $\Delta\Phi_{01}^{(0)}$ in spinor form and expanding the spinor in the basis of eigenfunctions of $\hat{L}$. The nonzero coefficients determine the change in the corresponding soliton paramters and emission of continuous radiation. In this order, the only nonzero projection is on the zeroth eigenfunction $\mathbf{0}$, so that

$$\Delta\mathbf{\Phi}_{01}^{(0)} = \frac{4i\eta_0\eta_\beta}{|\beta|}\mathbf{0} = \frac{4\eta_\beta}{|\beta|}\frac{\partial \mathbf{u}}{\partial \alpha},$$

where $\partial\mathbf{u}/\partial\alpha$ comes from Equation (2.25) and the soliton phase $\alpha_{01}^{(0)}$ is the only parameter effected. Thus the $\mathcal{O}(1/\beta)$ effect incurred by the reference channel soliton due to the collision is the phase shift

$$\Delta\alpha_{01}^{(0)} = \frac{4\eta_\beta}{|\beta|}.$$

2.3.2 Collision effects in $\mathcal{O}(1/\beta^2)$

In analogy with the previous section, the $\mathcal{O}(1/\beta^2)$ contribution of Equation (2.31) is

$$\frac{\partial \Phi_{02}^{(0)}}{\partial z} = i\left(\frac{\partial^2}{\partial t^2} - \eta_0^2\right)\Phi_{01}^{(0)} + 4i|\Psi_{00}|^2\Phi_{01}^{(0)} + 2i\Psi_{00}^2\Phi_{01}^{(0)*} \\ +4i|\Psi_{\beta 0}|^2\Phi_{01}^{(0)} + 4i\left(\Psi_{\beta 0}\Phi_{\beta 1}^{(0)*} + \Psi_{\beta 0}^*\Phi_{\beta 1}^{(0)}\right)\Psi_{00},$$

but since $\Phi_{01}^{(0)}$ is purely imaginary and Ψ_{00} and $\Psi_{\beta 0}$ are both purely real, this equation reduces to

$$\frac{\partial \Phi_{02}^{(0)}}{\partial z} = i\left(\frac{\partial^2}{\partial t^2} - \eta_0^2 + 2\Psi_{00}^2 + 4\Psi_{\beta 0}^2\right)\Phi_{01}^{(0)}.$$

To obtain the collision-induced effects in this order, this equation must be integrated over all values of z. Thus terms on the right hand side which are odd in z make no contribution, and only one even term from the second derivative of $\Phi_{01}^{(0)}$ remains:

$$\frac{\partial \Phi_{02}^{(0)}}{\partial z} = -\frac{4\eta_0^2\eta_\beta^2 \tanh x_0}{\beta \cosh x_0 \cosh^2 x_\beta}$$

Performing the integration results in

$$\Delta\mathbf{\Phi}_{02}^{(0)} = -\frac{4\eta_0^2\eta_\beta \tanh x_0}{\beta|\beta| \cosh x_0}\begin{pmatrix} 1 \\ 1 \end{pmatrix} = -\frac{4\eta_\beta}{\beta|\beta|}\frac{\partial \mathbf{u}}{\partial y},$$

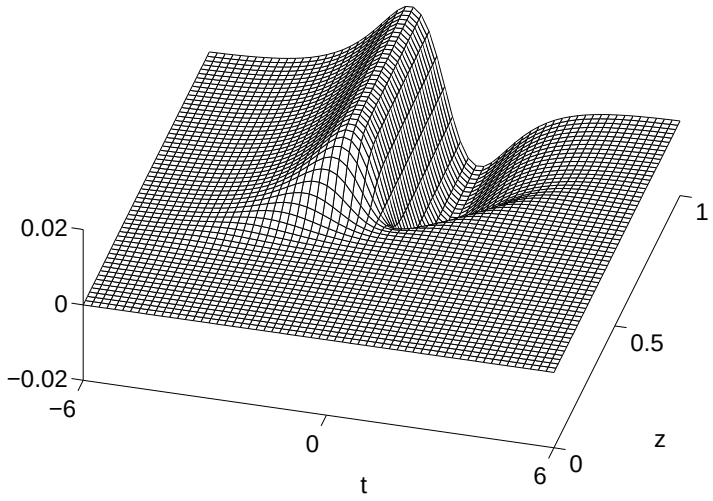

FIGURE 2.5. The collision-induced effects leading to position shift in $\mathcal{O}(1/\beta^2)$ given by $\Phi_{02}^{(0)}(t,z)$ with the same parameter values as described in Figure 2.4.

which implies the the collision induced effect in this order is a position shift

$$\Delta y_{02}^{(0)} = -\frac{4\eta_\beta}{\beta|\beta|}.$$

The contribution to $\Phi_{02}^{(0)}(t,z)$ which contributes to the position shift is plotted in Figure 2.5 Again note the rapid change in the collision region and residual $\tanh x_0 \mathrm{sech}\, x_0$ profile characteristic of position shift.

2.3.3 Perturbation theory vs. analytic solution

Here a comparison is made between the results of the perturbation theory and the analytic two-soliton collision solution obtained by inverse scattering methods [11]

which was originally presented in [32]. The exact solution is

$$\psi_{two} = \frac{\eta_1 \exp(i\chi_1)\left[(\eta_1^2 - \eta_2^2 + \beta_{12}^2)\cosh x_2 + 2i\eta_2\beta_{12}\sinh x_2\right]}{(\eta_1^2 + \eta_2^2 + \beta_{12}^2)\cosh x_1 \cosh x_2 - 2\eta_1\eta_2(\cos\chi_{12} + \sinh x_1 \sinh x_2)} + \frac{\eta_2 \exp(i\chi_2)\left[(\eta_2^2 - \eta_1^2 + \beta_{12}^2)\cosh x_1 - 2i\eta_1\beta_{12}\sinh x_1\right]}{(\eta_1^2 + \eta_2^2 + \beta_{12}^2)\cosh x_1 \cosh x_2 - 2\eta_1\eta_2(\cos\chi_{12} + \sinh x_1 \sinh x_2)},$$

where $\chi_{12} = \chi_1 - \chi_2$, $\beta_{12} = \beta_1 - \beta_2$, and the χs and βs are defined in Equations (2.15). The collision occurs at $z_0 = (y_2 - y_1)/2(\beta_1 - \beta_2)$. The assumption in our perturbation theory is that the frequency channels are well separated so that $\beta_{12} \gg 1$. In this limit, the two-soliton solution becomes

$$\begin{aligned}\psi_{two} = {} & \frac{\eta_0 \exp(i\chi_0)}{\cosh x_0}\left(1 - \frac{2i\eta_\beta \tanh x_\beta}{\beta} - \frac{2\eta_\beta^2 - 2\eta_0\eta_\beta \tanh x_0 \tanh x_\beta - \eta_\beta^2 \mathrm{sech}^2 x_\beta}{\beta^2}\right) \\ & + \frac{\eta_\beta \exp(i\chi_\beta)}{\cosh x_\beta}\left(1 + \frac{2i\eta_0 \tanh x_0}{\beta} - \frac{2\eta_0^2 - 2\eta_0\eta_\beta \tanh x_0 \tanh x_\beta - \eta_0^2 \mathrm{sech}^2 x_0}{\beta^2}\right) \\ & + \frac{\eta_0\eta_\beta^2 \exp[i(2\chi_\beta - \chi_0)]}{\beta^2 \cosh^2 x_0 \cosh x_\beta} + \frac{\eta_0^2\eta_\beta \exp[i(2\chi_0 - \chi_\beta)]}{\beta^2 \cosh x_0 \cosh^2 x_\beta} + \mathcal{O}(1/\beta^3),\end{aligned} \tag{2.36}$$

where the notation $\beta_1 = 0$ and $\beta_2 = \beta$ is adopted to be consistent with the perturbation analysis. Note that this expression is in the form of Equations (2.28) and (2.29), where the terms ϕ_0 and ϕ_β are $\mathcal{O}(1/\beta)$ and the terms $\phi_{-\beta}$ and $\phi_{2\beta}$ are $\mathcal{O}(1/\beta^2)$. In the region far before the collision point, where $z \ll z_0 - 1/\beta$, this expression reduces

to

$$\psi_{two}^{before} = \frac{\eta_0 \exp(i\chi_0)}{\cosh x_0}\left(1 \pm \frac{2i\eta_\beta}{\beta} - \frac{2\eta_\beta^2 \pm \eta_0\eta_\beta \tanh x_0}{\beta^2}\right) + \frac{\eta_\beta \exp(i\chi_\beta)}{\cosh x_\beta}\left(1 \pm \frac{2i\eta_0}{\beta} - \frac{2\eta_0^2 \mp \eta_0\eta_\beta \tanh x_\beta}{\beta^2}\right)$$

for $\mp\beta$. In the region far after the collision point, where $z \gg z_0 - 1/\beta$, Equation (2.36) reads

$$\psi_{two}^{after} = \frac{\eta_0 \exp(i\chi_0)}{\cosh x_0}\left(1 \mp \frac{2i\eta_\beta}{\beta} - \frac{2\eta_\beta^2 \mp \eta_0\eta_\beta \tanh x_0}{\beta^2}\right) + \frac{\eta_\beta \exp(i\chi_\beta)}{\cosh x_\beta}\left(1 \mp \frac{2i\eta_0}{\beta} - \frac{2\eta_0^2 \pm \eta_0\eta_\beta \tanh x_\beta}{\beta^2}\right)$$

Taking $\psi_{two}^{after} - \psi_{two}^{before}$ and comparing the result with Equations (2.25) results in the following expressions for the phase shifts in $\mathcal{O}(1/\beta)$:

$$\Delta\alpha_{01}^{(0)} = \frac{4\eta_\beta}{|\beta|} = \Delta\alpha_{\beta 1}^{(0)},$$

and position shifts in $\mathcal{O}(1/\beta)$:

$$\Delta y_{01}^{(0)} = -\frac{4\eta_\beta}{\beta|\beta|}, \quad \Delta y_{\beta 1}^{(0)} = \frac{4\eta_\beta}{\beta|\beta|}.$$

The results for the zero channel soliton are identical to those obtained using the perturbation theory. Note the sum of the position shifts of the colliding solitons is

zero, since momentum is among the infinite number of quantities conserved by NLS.

2.3.4 Collision effects in $\mathcal{O}(\epsilon/\beta)$, general case

Substituting Equations (2.32) and (2.33) into Equation (2.31) and collecting the $\mathcal{O}(\epsilon/\beta)$ terms which are dominant in the collision region results in

$$\frac{\partial \Phi_{02}^{(1)}}{\partial z} = 4i|\Psi_{\beta 0}|^2\Psi_{01} + 4i\Psi_{\beta 0}(\Psi_{\beta 1} + \Psi_{\beta 1}^*)\Psi_{00} + \cdots , \tag{2.37}$$

where the ellipsis represents the zero-channel contributions of $\epsilon F(\Psi_{00}, \Psi_{\beta 0})$. To proceed further requires the specific forms of Ψ_{01} and $\Psi_{\beta 1}$, which depend on the type of high-order correction being considered. In the following section the quintic nonlinear correction term is analyzed.

2.4 The effects of quintic nonlinearity on soliton collisions

For the remainder of this chapter, the high-order correction term is specialized to quintic nonlinearity. In order to determine the validity of this model, a full parameter analysis must be conducted. Since quintic nonlinearity is just one of many high-order effects that ultrashort pulses encounter, a parameter regime must be found such that the quintic term is the leading order correction, and all other high-order effects are of subleading order. Only after it is determined that a multichannel transmission

system may indeed be built using the appropriate parameter regime does it make sense to study the effects of the governing equation in that regime.

2.4.1 A valid parameter regime for cubic-quintic nonlinear Schrödinger

In dimensional form, the generalization of NLS which includes all the dominant high-order correction terms is written in the copropagating reference frame as

$$\begin{aligned} i\frac{\partial E}{\partial z} - \frac{k''}{2}\frac{\partial^2 E}{\partial t^2} - \frac{ik'''}{6}\frac{\partial^3 E}{\partial t^3} \\ = -\frac{\omega_0 n_2}{c}\left[|E|^2E + \frac{i}{\omega_0}\frac{\partial}{\partial t}\left(|E|^2E\right) - T_R E\frac{\partial}{\partial t}\left(|E|^2\right)\right] - \frac{\omega_0 n_4}{c}|E|^4E. \end{aligned} \tag{2.38}$$

Here T_R characterizes the Raman gain curve. Introducing the scaled variables $z = z_{d2}\zeta$, $t = \tau_0\tau$, and $E = A_0^{1/2}u$, this equation may be written in dimensionless form as

$$i\frac{\partial u}{\partial \zeta} + \frac{\partial^2 u}{\partial \tau^2} + \frac{z_{d2}}{z_c}|u|^2u = i\frac{z_{d2}}{z_{d3}}\frac{\partial^3 u}{\partial \tau^3} - i\frac{z_{d2}}{z_s}\frac{\partial}{\partial \tau}\left(|u|^2u\right) + \frac{z_{d2}}{z_R}u\frac{\partial}{\partial t}\left(|u|^2\right) + \frac{z_{d2}}{z_q}|u|^4u.$$

In this form, all of the coefficients are ratios of the characteristic lengths of each effect. In this form, the relevance of each term is easy to assess. The terms z_{d2}, z_{d3}, z_c, z_s, z_R, and z_q stand for the characteristic lengths of second-order dispersion, third-order dispersion, cubic nonlinearitiy, optical shocking, Raman, and quintic nonlinearity, repsectively. These quantities are related back to the original physical parameters in

Equation (2.38) through

$$z_{d2} = \frac{2\tau_0^2}{|k''|} \quad z_{d3} = \frac{6\tau_0^3}{k'''} \quad z_c = \frac{c}{A_0\omega_0 n_2}$$
$$z_s = \frac{c\tau_0}{A_0 n_2} \quad z_R = \frac{c\tau_0}{A_0\omega_0 n_2 T_R} \quad z_q = \frac{c}{A_0^2\omega_0|n_4|}$$

where the absolute value of k'' is taken to insure the positivity of z_{d2}. In fact, the so-called "bright" soliton propagation considered here takes place only for $k'' < 0$, the *anomolous* group velocity dispersion regime. Fixing the relationship between peak pulse amplitude and pulse width according to $A_0 = c|k''|/\omega_0 n_2 \tau_0^2$ results in $z_{d2}/z_c = 2$ so that

$$i\frac{\partial u}{\partial \zeta} + \frac{\partial^2 u}{\partial \tau^2} + 2|u|^2 u = i\frac{z_{d2}}{z_{d3}}\frac{\partial^3 u}{\partial \tau^3} - i\frac{z_{d2}}{z_s}\frac{\partial}{\partial \tau}\left(|u|^2 u\right) + \frac{z_{d2}}{z_R}u\frac{\partial}{\partial \tau}\left(|u|^2\right) + \frac{z_{d2}}{z_q}|u|^4 u. \quad (2.39)$$

A typical multichannel soliton transmission system clusters channels very near the center channel wavelength $\lambda_0 = 1.55\mu$m. Then $\omega_0 = 2\pi c/\lambda_0 = 1220\text{ps}^{-1}$ and for SiO_2 optical fiber [38, 20], $n_2 = 1.2 \times 10^{-22}(\text{m/V})^2$, $n_4 = -4.4 \times 10^{-37}(\text{m/V})^4$, $k'' = -20\text{ps}^2/\text{km}$, and $k''' = 0.1\text{ps}^3/\text{km}$. The other constants are $n_0 = 1.444$, $c = 3 \times 10^{-7}\text{km/ps}$, and $T_R \simeq 5\text{fs}$. Using these constants, the necessary relationship between the pulse peak power and duration may be determined:

$$P_0 = \frac{\epsilon_0 n_0 c}{2} A_0 S \simeq 3.93\tau_0^{-2},$$

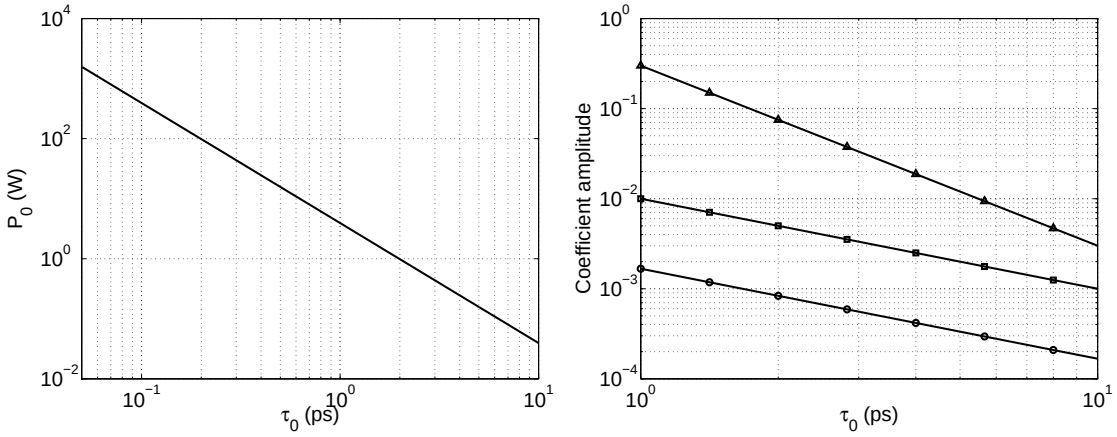

FIGURE 2.6. Left: Relationship between pulse width τ_0 and peak power P_0 required to maintain the cubic nonlinearity coefficient of 2 (for $S = 50\mu\text{m}^2$). Right: The dimensionless amplitude of the coefficients in Equation (2.39) as a function of pulse width; circles indicate third-order dispersion z_{d2}/z_{d3}, squares indicate Raman z_{d2}/z_R, and triangles indicate quintic nonlinearity z_{d2}/z_q. The coefficient of optical shocking is not shown due to its exceedingly small $\mathcal{O}(10^{-15})$ amplitude.

where S is the effective fiber core area. Typical fibers have core areas in the 50-80μm^2 range [20]; to compute the power $S = 50\mu\text{m}^2$ is used since tighter transverse mode confinement increases nonlinear response, which allows the use of shorter duration pulses at lower peak power. The relationship between pulse peak power and width is plotted in Figure 2.6.

The influence of the high-order correction terms in Equation (2.39) may be compared by stating them in original physical parameters:

$$\frac{z_{d2}}{z_{d3}} = \frac{k'''}{3|k''|\tau_0} \qquad \frac{z_{d2}}{z_s} = \frac{2}{\omega_0\tau_0}$$
$$\frac{z_{d2}}{z_R} = \frac{2T_R}{\tau_0} \qquad \frac{z_{d2}}{z_q} = \frac{2c|n_4 k''|}{\omega_0 n_2^2 \tau_0^2}$$

The amplitude of these coefficients is plotted as a function of pulse width in Figure 2.6. It is clear that the influence of the Raman effect is negligable for pulse widths $\tau_0 < 4$ps. The effects of third-order dispersion may be neglected for all values of τ_0 shown. The requirement of the perturbation theory is that the coefficient of the quintic term is small, which is satisfied for $\tau_0 > 1.5$ps. This range of valid pulse widths corresponds to peak powers of $0.25\text{W} < P_0 < 1.1\text{W}$. Thus cubic-quintic nonlinear schrödinger (CQNLS) equation

$$i\frac{\partial u}{\partial z} + \frac{\partial^2 u}{\partial t^2} + 2|u|^2 u = \epsilon|u|^4 u \tag{2.40}$$

is a valid model for pulse propagation given the physical constants and tuning parameters discussed. Here, $\epsilon = 2cn_4k''/\omega_0 n_2^2\tau_0^2$, so the small parameter values that correspond to the region of validity are given by $0.02 < \epsilon < 0.3$.

As an example, consider a transmission system using 2ps pulses. Such a sytem could transmit 50GBit/s per channel using 20ps timeslots. In order to satisfy the perturbation theory requirement that $\epsilon \ll 1$, it follows that $z_{d2} \ll z_q$. These characteristic distances work out as $z_{d2} = 0.4$km and $z_q = 5.32$km and the condition is satisfied. The second requirement is that the next most influential correction, in this case the Raman term, is of subleading order so that $z_q \ll z_R$. Using these system parameters, $z_R = 80$km and this condition is also well satisfied. It should be noted that in higher orders such as $\mathcal{O}(\epsilon^2)$, the effect of the quintic term may not be well

separated from first-order Raman effects when using these example parameter values, so determining the validity of the perturbation theory results in this and higher orders requires further analysis.

2.4.2 Collision effects in $\mathcal{O}(\epsilon/\beta)$, quintic case

Inserting Equations (2.32) and (2.33) into Equation (2.40) and collecting the $\mathcal{O}(\epsilon/\beta)$ terms results in the following specialization of Equation (2.37) to the quintic case:

$$\begin{aligned}\frac{\partial \Phi_{02}^{(1)}}{\partial z} &= 4i|\Psi_{\beta 0}|^2\Psi_{01} + 4i\Psi_{\beta 0}(\Psi_{\beta 1} + \Psi_{\beta 1}^*)\Psi_{00} \\ &\quad -6i\epsilon|\Psi_{\beta 0}|^2|\Psi_{00}|^2\Psi_{00} - 3i\epsilon|\Psi_{\beta 0}|^4\Psi_{00}, \end{aligned} \tag{2.41}$$

valid for the collision region. The $\mathcal{O}(\epsilon)$ corrections may be obtained by expanding the solitary wave solutions of Equation (2.40) [39, 40], but they were also computed in Section 2.3. With general parameter values, Equation (2.27) reveals that

$$\Psi_{\beta 1}(x) = \eta_\beta^3 \epsilon \frac{1 + \tanh^2 x}{6 \cosh x}. \tag{2.42}$$

The first term on the right hand side of Equation (2.41) may be neglected since it does not contribute to any new effect. Its effect is the same $\mathcal{O}(1/\beta)$ phase shift accounted

for in Equation (2.36). Using this result, the explicit form of Equation (2.41) is

$$\frac{\partial \Phi_{02}^{(1)}}{\partial z} = \frac{4i\epsilon\eta_0\eta_\beta^4(1+\tanh^2 x_\beta)}{3\cosh x_0 \cosh^2 x_\beta} - \frac{6i\epsilon\eta_0^3\eta_\beta^2}{\cosh^3 x_0 \cosh^2 x_\beta} - \frac{3i\epsilon\eta_0\eta_\beta^4}{\cosh x_0 \cosh^4 x_\beta}.$$

Integrating this equation over the collision region results in

$$\begin{aligned}\Phi_{02}^{(1)}(t, z_0 + \tilde{z}/|\beta|) &= -\frac{6i\epsilon\eta_0^3\eta_\beta}{|\beta|\cosh^3 x_0} - \frac{2i\epsilon\eta_0\eta_\beta^3}{9|\beta|\cosh x_0} \\ &= \frac{6i\epsilon\eta_0^3\eta_\beta \tanh^2 x_0}{|\beta|\cosh x_0} - \frac{2i\epsilon\eta_0\eta_\beta}{|\beta|\cosh x_0}\left(3\eta_0^2 + \frac{\eta_\beta^2}{9}\right), \qquad (2.43)\end{aligned}$$

where the second line was obtained using the identity $\mathrm{sech}^2 x = 1 - \tanh^2 x$. The second term on the right hand side is proportional to $i\eta_0 \mathrm{sech}\, x_0$, which represents an additional collision-induced phase shift of

$$\Delta\alpha_{02}^{(1)} = -\frac{2\epsilon\eta_\beta}{|\beta|}\left(3\eta_0^2 + \frac{\eta_\beta^2}{9}\right).$$

The z-evolution of the parts of $\Phi_{02}^{(1)}$ which contribute to this phase shift are expressed as

$$\begin{aligned}\Phi_{02}^{(1)}(t, z) = &\frac{2i\epsilon\eta_0\eta_\beta^3}{3\beta\cosh x_0}(\tanh x_\beta - 1) + \frac{2i\epsilon\eta_0\eta_\beta^3}{9\beta\cosh x_0}(\tanh^3 x_\beta - 1) \\ &-\frac{i\epsilon\eta_0\eta_\beta^3}{\beta\cosh x_0}\left(\tanh x_\beta + \frac{\tanh x_\beta}{2\cosh^2 x_\beta} - 1\right).\end{aligned}$$

A plot of this function in the collision region appears in Figure 2.7. The first term on

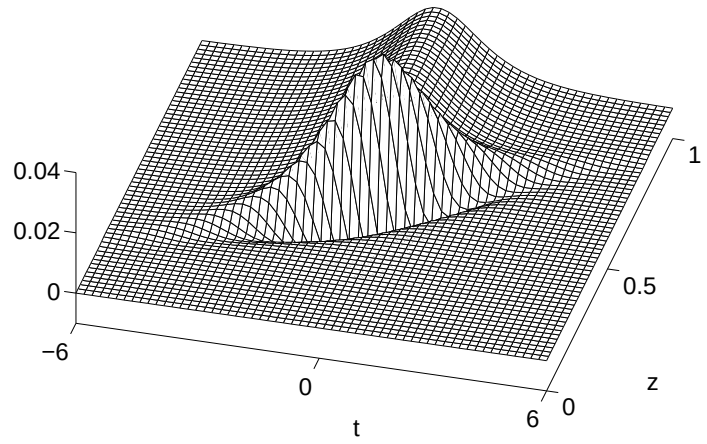

FIGURE 2.7. The collision-induced effects leading to phase shift due to the presence of quintic nonlinearity appearing in $\mathcal{O}(\epsilon/\beta)$. The imaginary part of $\Phi_{02}^{(1)}(t,z)/\epsilon$ is shown using the same parameters as descibed in Figure 2.4.

the right hand side of Equation (2.43) only makes a contribution to radiation emission and not to shifts in soliton parameters, since its spinor form has zero projections on the four discrete eigenfunctions of $\hat{L}$. Thus it may be expanded in terms of the continuous eigenfunctions:

$$\begin{aligned}\mathbf{v}_{02}(t, z_0 + \tilde{z}/|\beta|) &= 2iB\frac{\tanh^2 x_0}{\cosh x_0}\begin{pmatrix} 1 \\ -1 \end{pmatrix} \\ &= B\int_{\mathbf{R}} \left[a_k(z_0 + \tilde{z}/|\beta|)\mathbf{k}(x_0) + a_k^*(z_0 + \tilde{z}/|\beta|)\bar{\mathbf{k}}(x_0)\right] \mathrm{d}k,\end{aligned}$$

with $B = 3\epsilon\eta_0^3\eta_\beta/|\beta|$. The form of the expansion coefficient a_k at the end of the

collision region is determined by

$$\begin{aligned} a_k(t, z_0 + \tilde{z}/|\beta|) &= -\frac{1}{2\pi B} \langle \mathbf{k}|\hat{\sigma}_3|\mathbf{v}_{02}\rangle \\ &= \frac{i(k+i)^2}{4\cosh(\frac{\pi}{2}k)}. \end{aligned} \tag{2.44}$$

The collision-induced effect of radiation emission is nonlocal, i.e., it is not confined to the pulse like the soft modes which represent shifts in soliton parameters. Rather, the radiation is free to propagate away from the pulse. It evolution is governed by the linear partial differential equation

$$i\frac{\partial \mathbf{v}_{02}^{(f)}}{\partial z} + \eta_0^2 \hat{L}\mathbf{v}_{02}^{(f)} = 0, \tag{2.45}$$

where the superscript f indicates that this is free radiation in the post-collision region. This equation may be solved by expanding the radiation term in the continuous eigenfunction of $\hat{L}$:

$$\mathbf{v}_{02}^{(f)}(t, z) = B \int_{\mathbf{R}} \left[a_k(z)\mathbf{k}(x_0) + a_k^*(z)\bar{\mathbf{k}}(x_0)\right] \mathrm{d}k. \tag{2.46}$$

This expression is substituted into Equation (2.45) which results in

$$i\frac{\partial}{\partial z}\int_{\mathbf{R}} (a_k\mathbf{k} + a_k^*\bar{\mathbf{k}})\mathrm{d}k + \eta_0^2\hat{L}\int_{\mathbf{R}} (a_k\mathbf{k} + a_k^*\bar{\mathbf{k}})\mathrm{d}k = 0.$$

Passing the operators $\partial/\partial z$ and $\hat{L}$ through the integrals and using properties (2.23) gives an ordinary differential equation for the evolution of the expansion coefficient

$$\dot{a}_k = i\eta_0^2(k^2-1)a_k$$

which is supplemented by the initial condition in Equation (2.44). Here the overdot denotes differentiation with respect to z. Integrating this equation and applying the initial condition leads to

$$a_k(z) = \frac{i(k+i)^2}{4\cosh(\frac{\pi}{2}k)}\exp[i\eta_0^2(k^2-1)(z-c)],$$

with $c = z_0 + \tilde{z}/|\beta|$. This is then substituted into Equation (2.46) to yield a rather offensive expression whose best quality is that it simplifies to

$$\begin{aligned} v_{02}^{(f)}(t,z) &= \frac{B}{2\cosh^2 t}\int_{\mathbf{R}} \frac{\sin[\eta_0^2(1-k^2)(z-c)]\cos(kt)}{\cosh(\frac{\pi}{2}k)}\mathrm{d}k \\ &+ iB\int_{\mathbf{R}} \frac{(1-k^2)\cos(kt)+2k\tanh t\sin(kt)}{\cosh(\frac{\pi}{2}k)}\exp[i\eta_0^2(1-k^2)(z-c)]\mathrm{d}k, \end{aligned} \tag{2.47}$$

which is valid in the post-collision region $z > z_0 + \tilde{z}/|\beta|$. The z-evolution of the part of $\Phi_{02}^{(1)}$ that contributes to radiation emission in the collision region $z < z_0 + \tilde{z}/|\beta|$ is given by

$$v_{02}^{(c)}(t,z) = \frac{3i\epsilon\eta_0^3\eta_\beta\tanh^2 x_0}{|\beta|\cosh x_0}(1-\tanh x_\beta).$$

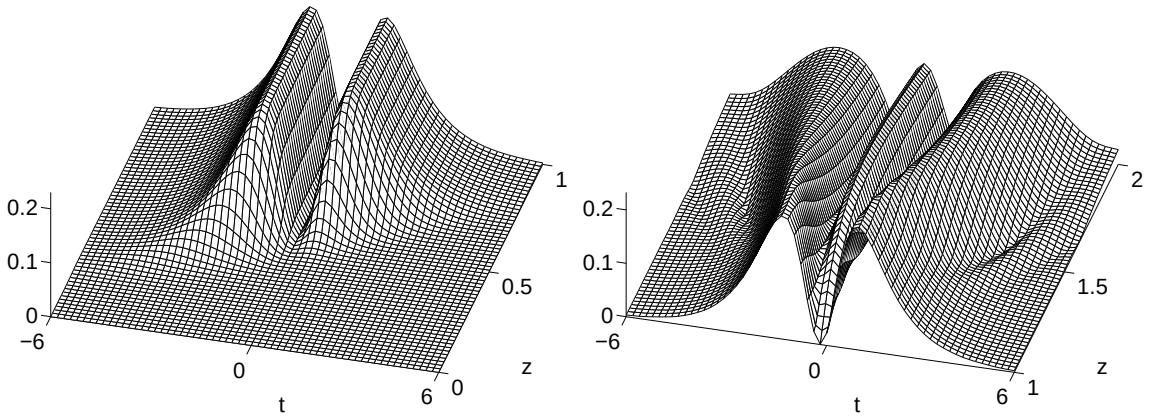

FIGURE 2.8. Collision-induced radiation emitted due the presence of quintic nonlinearity in $\mathcal{O}(\epsilon/\beta)$. Left: The emission of radiation in the collision region $|v_{02}^{(c)}(t,z)|/\epsilon$. Right: the propagation of emitted radiation in the post-collision region $|v_{02}^{(f)}(t,z)|/\epsilon$. The parameters are the same as those described in Figure 2.4.

Thus the emission and subsequent propagation of radiation in $\mathcal{O}(\epsilon/\beta)$ is described by $v_{02}^{(c)}$ in the collision region and $v_{02}^{(f)}$ in the post-collision region. Plots of the amplitude of these functions are displayed in Figures 2.8 and 2.9. These images illustrate a collision for which $z_0 = 1/2$ and $\beta = 10$ and the choice of $\tilde{z} = 5$ is made so that $v_{02}^{(c)}(t,1) = v_{02}^{(f)}(t,1)$. Note that the radiation does not disperse until it reaches the post-collision region at $z = 1$. This is because the dispersion term in Equation (2.31) does not make a contribution in this order of the perturbation theory. Including the $\mathcal{O}(\epsilon^2/\beta)$ correction yields more accurate results for the radiation dynamics [41], but radiation emission due to stimulated Raman scattering is also present in this parameter regime. Note that the coefficient of the Raman term in Equation (2.39) is equal to the square of the quintic coefficient at $\tau_0 \simeq 2$ps, which is within the

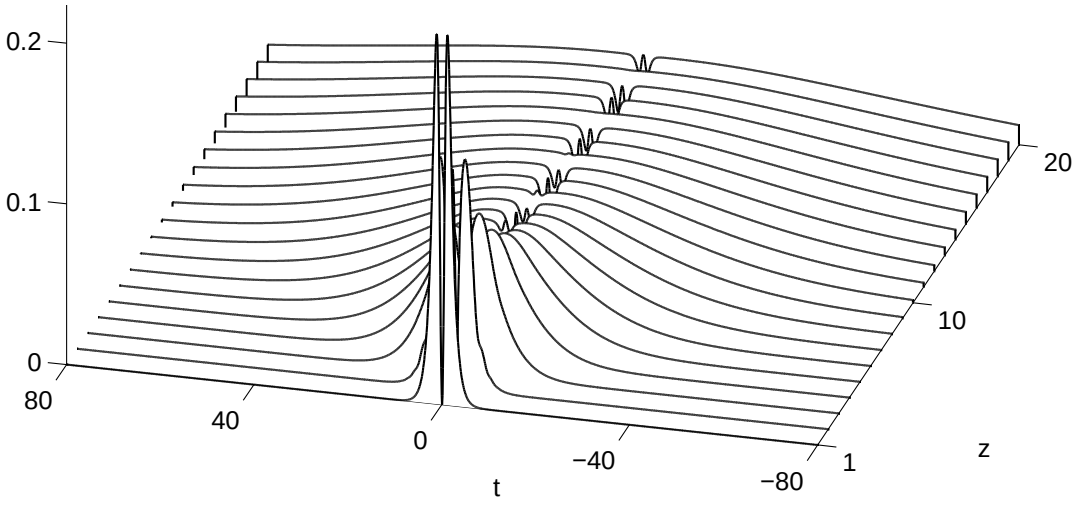

FIGURE 2.9. Long-range effects of collision-induced radiation $|v_{02}^{(f)}(t,z)|/\epsilon$.

valid range of pulsewidths considered in this regime. Also note the persistence and nonlocality of the radiation in Figure 2.9. In a data transmission system, this buildup of background radiation leads to intrachannel crosstalk of solitons in a bitstream, which leads to timing jitter and other malign effects.

Radiation emission causes the solitons to lose energy in an amount determined by evaluating

$$\mathcal{E}(z) = \int_{\mathbf{R}} |v_{02}(t,z)| \mathrm{d}t$$

in the limit $z \to \infty$. An asymptotic analysis [32] shows that

$$\mathcal{E} = \frac{2\pi B^2}{\eta_0} \int_{\mathbf{R}} |a_k|^2 \mathrm{d}k = \frac{48\epsilon^2 \eta_0^5 \eta_\beta^2}{5|\beta|^2}.$$

Since the energy in the soliton Ψ_{00} is $2\eta_0$, the fraction of energy lost in a single collision is given by

$$\mathcal{F} = \frac{24\epsilon^2\eta_0^4\eta_\beta^2}{5|\beta|^2}$$

which manifests as a reduction of soliton amplitude and an increase in width.

2.5 Numerical integration of generalized NLS

2.5.1 Fractional step methods

The performance of numerical integrators is often limited for equations which evolve according to different physical processes because rarely is one integration technique optimized for all the physical process. Most integrators perform well for some processes but not for others. Therefore it is advantageous to use different integrators on the same problem by integrating each physical process using a method which is taylored for that process. This is accomplished using fractional step methods, also known as split-step or operator splitting methods.

Suppose a quantity evolves according to the equation

$$\frac{\partial u}{\partial t} = (\hat{A} + \hat{B})u,$$

where $u = u(\mathbf{x}, t)$ is a function of the evolution variable t and $\mathbf{x}$ is a vector of spatial coordinates, and $\hat{A}$ and $\hat{B}$ are general noncommutative operators describing different physical processes. The case of two operators is discussed here, although the theory may be generalized to include more operators. The formal solution of this equation is

$$u(\mathbf{x}, t) = \exp[t(\hat{A} + \hat{B})]u(\mathbf{x}, 0), \tag{2.48}$$

but the evolution operator $\exp[t(\hat{A} + \hat{B})]$ is only a formal expression which is not explicitly computable in general. Thus consider using the compound evolution operator

$$u(\mathbf{x}, t) = \left[\prod_{j=1}^{k} \exp(a_j t\hat{A}) \exp(b_j t\hat{B})\right] u(\mathbf{x}, 0). \tag{2.49}$$

In this form, the constituent evolution operators are explicitly computable and the approximation is $\mathcal{O}(t^k)$ accurate for $k \leq 4$ for appropriately chosen fractional coefficients a_j and b_j.[4] A kth-order integrator may be derived by expanding the evolution operators in Equations (2.48) and (2.49), taking their difference, and choosing the fractional coefficients a_j and b_j such that the terms cancel to $\mathcal{O}(t^k)$. For higher order integrators, this computation is rather cumbersome and more sophisticated techniques [42] should be used. It is easy to show that a two-stage, first-order method

[4]For $\mathcal{O}(t^6)$ and $\mathcal{O}(t^8)$ accurate approximations, the minimum number of steps is $k = 8$ and $k = 16$, respectively [42]. The number of steps necessary for $\mathcal{O}(t^5)$ accuracy was not computed by the author.

requires $a_1 = b_1 = 1$. A general statement for integrators of all orders is

$$\sum_{j=1}^{k} a_j = 1 = \sum_{j=1}^{k} b_j,$$

since the contribution of each process must be fully accounted for at time t. A three-stage, second-order integrator [43] has $a_1 = a_2 = 1/2$, $b_1 = 1$, $b_2 = 0$ and requires only fractionally more computational expense than the first-order method. This is due to the fact that each operator commutes with itself:

$$\begin{aligned} u(\mathbf{x}, t + \Delta t) &= \left[\exp\left(\tfrac{\Delta t}{2}\hat{A}\right)\exp\left((\Delta t\hat{B}\right)\exp\left(\tfrac{\Delta t}{2}\hat{A}\right)\right]^n(\mathbf{x}, t) \\ &= \exp\left(\tfrac{\Delta t}{2}\hat{A}\right)\left[\exp\left(\Delta t\hat{B}\right)\exp\left(\Delta t\hat{A}\right)\right]^{n-1} \\ &\times \exp\left(\Delta t\hat{B}\right)\exp\left(\tfrac{\Delta t}{2}\hat{A}\right)u(\mathbf{x}, t). \end{aligned} \tag{2.50}$$

Here the time interval $[0, T]$ has been discretized such that $T = n\Delta t$ and $u_n(\mathbf{x}) = u(T, \mathbf{x})$. This is analogous to the numerical evaluation of integrals by the trapezoid rule, which is identical to the Riemann sum except at the interval endpoints, yet obtains a higher order of accuracy. This property extends to higher even-order integrators, although the increase in efficiency is not as dramatic as this case.

A six-stage, third-order integrator may be derived with $a_1 = 7/24$, $a_2 = -1/24$, $a_3 = 3/4$, $b_1 = 24/17$, $b_2 = -2/3$, and $b_3 = 13/51$. Unfortunately, a five-stage third-order method does not exist. The last method described here is a seven-stage,

fourth-order integrator [44, 42]. The fractional coefficients in this case are given by

$$a_1 = a_4 = \frac{1}{2(2-2^{1/3})} \quad a_2 = a_3 = \frac{1-2^{1/3}}{2(2-2^{1/3})}$$
$$b_1 = b_3 = \frac{1}{2-2^{1/3}} \quad b_2 = \frac{-2^{1/3}}{2-2^{1/3}} \quad b_4 = 0.$$

The fractional coefficients for higher-order integrators may be found by solving a nonlinear system of algebraic equations [42]. However, for higher orders more than $2k-1$ stages required at each evolution step which results in decreased efficiency.

2.5.2 Application to pulse propagation equations

In the case of ideal NLS [Equation (2.9)], optical coordinates are used; the evolution variable is z and retarded time t plays the role of the single space variable. Thus the operators involved are

$$\hat{A} = i\frac{\partial^2}{\partial t^2}, \qquad \hat{B} = 2i|u|^2. \tag{2.51}$$

Thus fractional step methods allow separate consideration of the two equations

$$\frac{\partial u}{\partial z} = i\frac{\partial^2 u}{\partial t^2}, \qquad \frac{\partial u}{\partial z} = 2i|u|^2 u. \tag{2.52}$$

The first of these equations is solved by applying the Fourier transform in the time variable and solving the resulting ordinary differential equation in the frequency domain. This yields

$$u(\omega, z) = u(\omega, 0) \exp(-i\omega^2 z),$$

to which the inverse Fourier transform is applied to return to the time domain. The solution is the convolution

$$u(t, z) = \frac{1}{2\sqrt{i\pi z}} \int_{\mathbf{R}} u(t - s, 0) \exp\left(\frac{is^2}{4z}\right) \mathrm{d}s.$$

Is easy to see from this expression that the effect of this term is smoothing and broadening of initial data with increasing z. The discrete analog of this procedure is performed very efficiently at each evolution step using the fast Fourier transform (FFT) [45]. This is written as

$$\mathbf{u}_{n+1} = \hat{F}^{-1} \hat{D} \hat{F} \mathbf{u}_n,$$

where $\mathbf{u}_n$ is the solution vector (distributed on uniformly spaced t nodes) at the nth evolution step and $\hat{F}$ represents the FFT operator and $\hat{D} = \exp(-i\Delta z \boldsymbol{\omega}^2)$. Here, $\boldsymbol{\omega}^2$

is the termwise product of $\boldsymbol{\omega}$ vectors, whose mth entry is given by

$$\omega_m = \begin{cases} \Delta\omega(m-1), & 1 \leq m \leq 2^{p-1} \\ \Delta\omega(m-1-2^p), & 2^{p-1}+1 \leq m \leq 2^p \end{cases}$$

where $\Delta\omega = 2\pi/2^p\Delta t$ and the length of $\boldsymbol{\omega}$ is 2^p.

An advantage of the FFT is that if $\mathbf{u}$ is distributed on 2^p t-nodes, where p is a whole number, then the transformation requires only $2^{p-1}p$ floating point operations. Not only is the computation cheap, but it is also accurate. The spectral discretization converges exponentially fast for smooth functions, i.e., it is $\mathcal{O}\big(\exp(-2^p)\big)$ accurate for infinitely differentiable periodic functions. While pulse propagation problems are defined on the real line, the convergence dependence upon periodicity and automatic implementation of periodic boundary conditions by the FFT is usually not a problem since the amplitude and first derivative of the solutions under consideration decay exponentially as $t \to \pm\infty$. Then the error induced by the periodic boundary conditions in exponentially small if the boundaries are well separated from the localized solution. If the solution involves radiation emission, then special care must be taken with the interaction of radiation near the boundaries. This will be discussed in the next section.

The second equation of (2.52) has an exact solution, since $|u|^2$ does not change with z. This may be seen by multiplying the equation through by u^* and adding this new equation to its complex conjugate, resulting in $\partial|u|^2/\partial z = 0$. Thus $|u|^2$ is

constant and the equation is integrated as if it were linear, which yields

$$u(t,z) = u(t,0)\exp\left[2i|u(t,0)|^2 z\right].$$

It is clear why this effect is called phase modulation. This term only effects the phase of the solution through the product of z and the intensity of the field. As an implementation example, a single integration step using the second-order fractional step method is given by

$$\mathbf{u}_{n+1} = \exp\big(i\tfrac{\Delta z}{2}|\mathbf{u}_{n+1/2}|^2\big)\hat{F}^{-1}\hat{D}\hat{F}\exp\big(i\tfrac{\Delta z}{2}|\mathbf{u}_n|^2\big)\mathbf{u}_n,$$

where $\mathbf{u}_{n+1/2}$ represents the field after half a nonlinear evolution step and a full linear evolution step. Integrating NLS in this fashion has become the scientific and industrial standard for more than a decade.

The fractional step method may be used for NLS with high-order correction terms [Equation (2.13)] in a variety of ways, but the specific correction term under consideration dictates how the term is incorporated. The two-operator fractional step method (2.49) generalizes easily for third-order dispersion and quintic nonlinearity corrections. In the former case, the TOD operator is incorporated in the definition of $\hat{A}$ in Equation (2.51) at no additional computational expense, while in the latter, the quintic term is incorporated into $\hat{B}$ at very little additional expense. The exactness

of the solutions in each fractional step is not effected by including either of these corrections.

The Raman and optical shocking terms, on the other hand, do not admit exact solutions when incorporated in the subproblems (2.52). This complication may be handled in two ways. First, three-operator fractional step methods are derived and the correction term is handled using one's favorite ODE integrator which commits no larger error than the splitting. The second approach is to simply abandon the benefits of exactly integrating the phase modulation term and group both nonlinear terms together in the definition of $\hat{B}$, which is solved using an ODE integrator. The author has had success using standard explicit Runge-Kutta methods [46] with this approach.

2.5.3 Boundary conditions

One unifying feature of dynamical systems which support solitary wave solutions, such as NLS and its generalizations, is that the solution may be decomposed as a sum of localized solitary waves (or solitons for ideal NLS) and nonlocal radiation. The radiation eventually finds its way to the boundaries of the computational domain and interacts with it in a nonphysical way. In the case of Dirichlet boundary conditions, the radiation reflects from the artificial boundary back into the domain, corrupting the dynamics of interest. Reflection does not occur with periodic boundary conditions, but left-propagating waves near the right boundary interfere with right-propagating

waves near the left boundary, causing similarly spurious results.

The simplest way to avoid these effects is to simply make the computational domain large enough that the radiation does not reach the boundaries. This approach may be practical for short integrations in z, but limited computational resources preclude this method for long z integrations and more advanced methods must be used. One way is to apply an artificial absorber periodically (say, after every q integration steps, where q depends on simulation requirements) during the integration. This entails multiplying the solution by an absorber function $a(t)$ which is unity in the domain of interest but decays smoothly near the boundaries. This technique can greatly reduce the amplitude of radiation near the boundaries while preserving the dynamics of interest and is easily implemenented. Figure 2.10 shows linear and log plots of a typical absorber function

$$a(t) = \begin{cases} \exp\{-[(t-20+T)/10]^4\}, & t < 20-T \\ 1, & 20-T < t < T-20 \\ \exp\{-[(t-T+20)/10]^4\}, & t > T-20 \end{cases} \tag{2.53}$$

in which $T = 50$ and the absorbing layers are 20 time units thick.

The disadvantages of this technique are that the absorbing layers require an increase in the size of the computational domain which induces additional overhead and that a small fraction of the radiation reflects off the absorber back into the domain of interest. For some simulations such as those performed in [41], the amplitude of

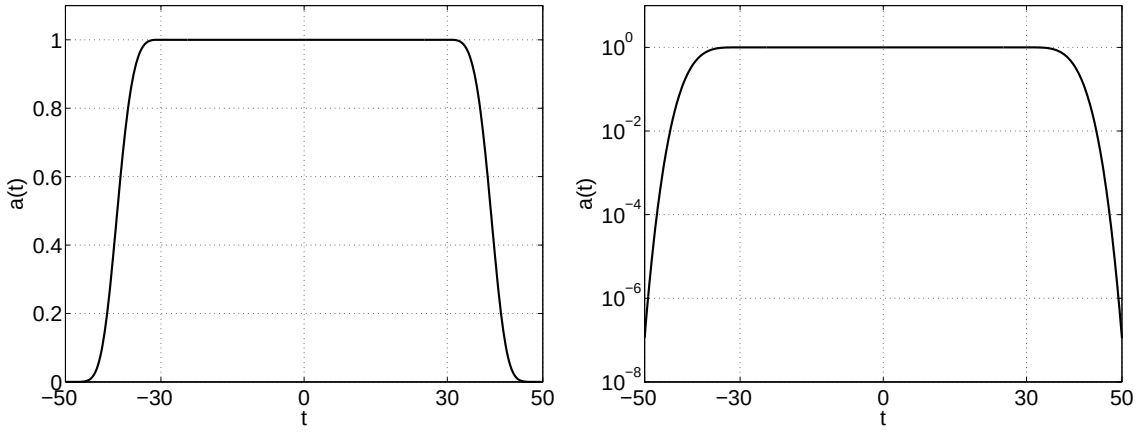

FIGURE 2.10. Linear and log plots of the absorber function of Equation (2.53).

reflected waves small enough to have a negligible effect on soliton dynamics.

Another absorbing boundary condition, called the perfectly matched layer (PML) [47], was developed for Maxwell's equations and is more reliable and efficient than the multiplicative absorber described above. Its extension to the Schrödinger equation is described in [48]. For its application to nonlinear pulse propagation equations, it requires that the amplitude of waves propagating in the layer be small since it is derived from the linearized equation. In layers near the boundaries, the pulse propagation equation is replaced with

$$i\frac{\partial u}{\partial z} + \frac{1}{1+\sigma e^{i\gamma}}\frac{\partial}{\partial t}\left(\frac{1}{1+\sigma e^{i\gamma}}\frac{\partial}{\partial t}\right)u = 0,$$

where the time derivatives are modified to include the PML.

The last boundary condition discussed here is the so-called transparent boundary

condition [49]. This condition also requires that the solution amplitude be small at the boundaries, since the linearized equation is used in the derivation. However, it has the feature of being applicable to propagation in inhomogeneous media. The Laplace transform is applied to the linear Schrödinger equation in the evolution variable which leads to the nonlocal boundary conditions

$$\frac{\partial}{\partial t}u(\pm T, z) = \pm\frac{i-1}{\sqrt{2\pi}}\int_0^z \frac{\partial}{\partial \zeta}\big[u(\pm T, \zeta)\big]\frac{\mathrm{d}\zeta}{\sqrt{z-\zeta}}$$

for a computational domain of $t \in [-T, T]$. The nonlocality is not a significant computational issue since the entire integral needs not be computed at each evolution step, it simply needs to be updated with the contribution from the most recent step. The disadvantage of this method is that it is not compatible with the FFT, so a different temporal discretization must be used to implement it.

2.5.4 Convergence analysis for ideal NLS

The performance of this family of fractional step methods is determined by comparing their numerical solutions to analytic solutions and by examining how well they preserve the first few integrals of motion of the system they are approximating. In this section the first- through fourth -order integrators are applied to the ideal NLS equation (2.9) and compared with analytic solutions corresponding to single soliton propagation and a soliton collision as shown in Figure 2.11.

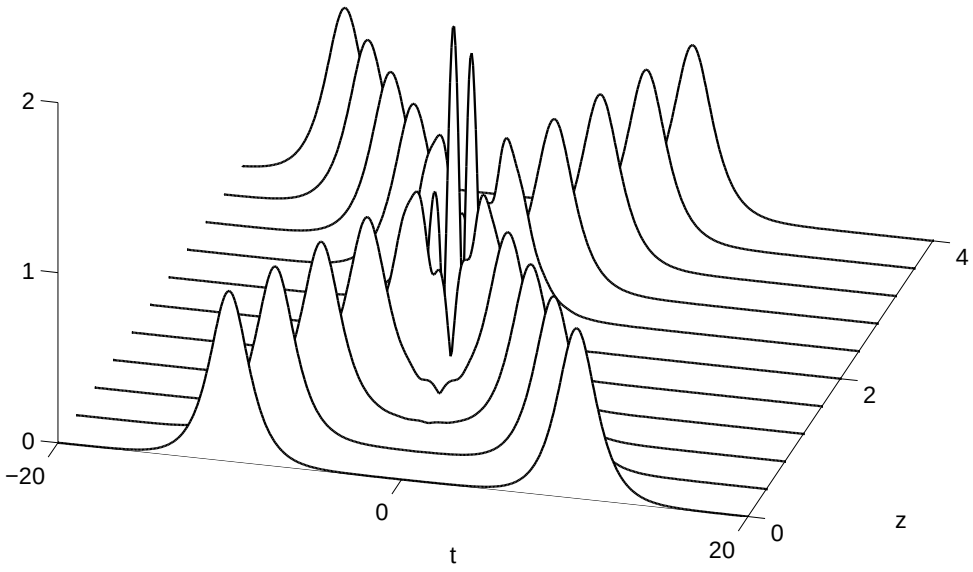

FIGURE 2.11. Amplitude $|u|$ of the exact solution of an ideal soliton collision with parameters $\eta_1 = \eta_2 = 1$, $\alpha_1 = \alpha_2 = 0$, $\beta_1 = 3$, $\beta_2 = -2$, $y_1 = -10$, and $y_2 = 10$.

The first test is to compute the difference between the exact solution for single soliton propagation and the computed solution at $z = 2$. In this computation the exact soliton $u(t, 0) = \operatorname{sech}(t)$ is used as the initial condition for the four different fractional step methods. The convergence obtainded by refining the integration step-size Δz is shown in Figure 2.12. In these simulations, a symmetric computational domain of $-T < t < T$ is used with $T = 40$, the spectral time discretization is used with $p = 10$, or 1024 Fourier modes, and the consequent periodic boundary conditions are left untreated. The error is evaluated by taking the one norm of the difference between exact and computed solutions. Plotting the results on the log-log scale reveals the order of the method, which is the negative slope of the lines. In this study, the

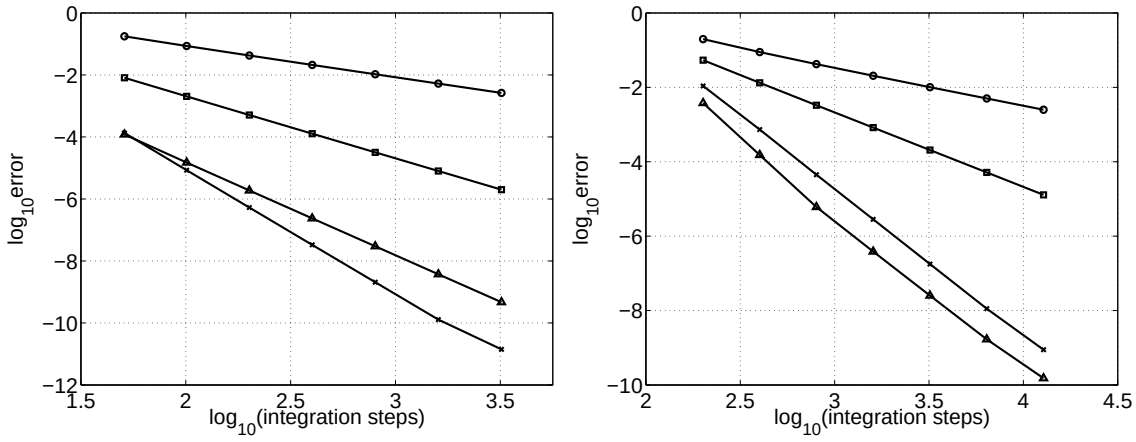

FIGURE 2.12. Left: Convergence of the first- through fourth-order fractional step methods with z-refinement. The first- through fourth-order integrators are indicated by circles, squares, triangles, and x's, respectively, for the single soliton propagation problem. Right: the corresponding results for the collision problem.

slopes are given by -1.00, -2.00, -3.00, and -4.01, showing excellent agreement with the predicted orders of the integration methods.

The methods are also tested on the strongly nonlinear process of a soliton collision. After the pulses collide, the error is computed at $z = 4$ when the pulses are well separated. The convergence behavior of the four integration methods are plotted in Figure 2.12. In order to reduce the possibility of certain symmetries causing error cancellation, the collision parameters are chosen so that the collision is asymmetric. Again, $p = 10$ and $T = 40$ in these simulations. The most interesting result is that the third-order splitting method actually achieves fourth-order convergence and is in fact more accurate than the true fourth-order method. The slopes are given by -1.02, -2.00, -4.14, and -3.98. To explain this behavior, the error of the third-order

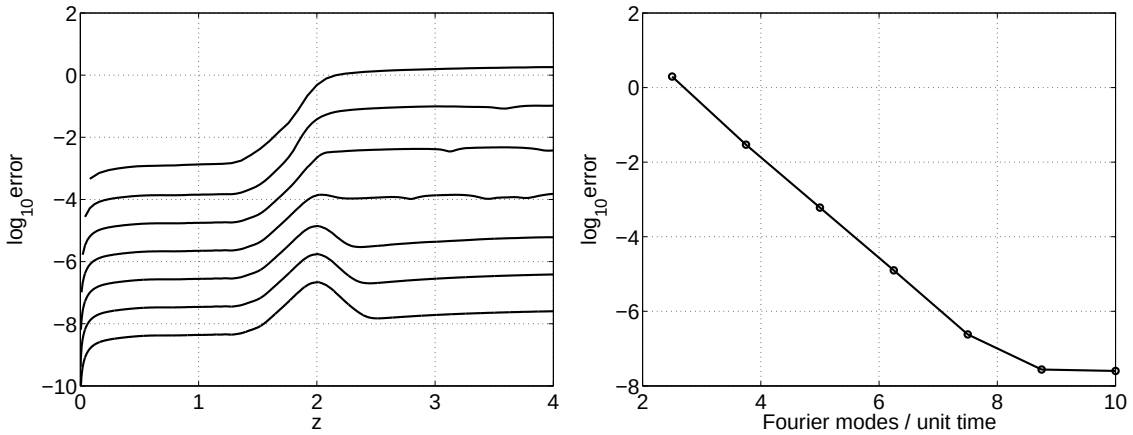

FIGURE 2.13. Left: Error in the third-order splitting method as a function of distance for the collision problem. Right: Exponential convergence with temporal grid refinement.

method is plotted as a function of z for $\Delta z = 0.08$, 0.04, 0.02, 0.01, 0.005, 0.0025, and 0.00125 in Figure 2.13. Before the collision, the error curves are closer together than they are after the collision. This accounts for the third-order convergence observed for single pulse propagation in Figure 2.12. As the z-discretization is refined, the error begins to drop after the collsion point of $z = 2$. This feature causes the error curves to separate with z-refinement, resulting in increasingly higher accuracy. This interesting behavior warrents more study but is out of the scope of this work.

The convergence behavior of the temporal discretization is shown in Figure 2.13. Here, the log of the error, measured at the end of the collision problem, is plotted against the number of Fourier modes used per unit time. On the log-linear scale, a linear function indicates an exponential convergence rate, i.e., the error decreases faster than any finite power of the mesh spacing Δt. This confirms that the spectral

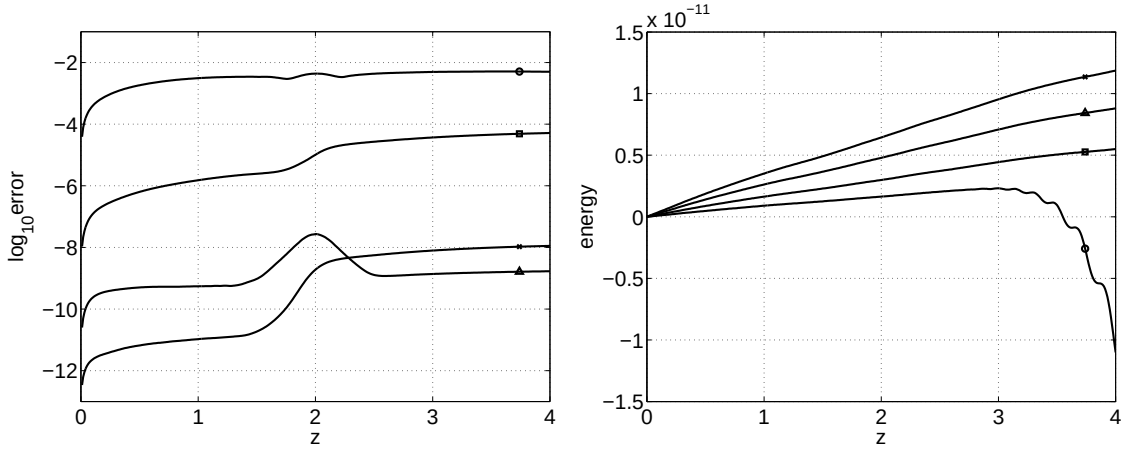

FIGURE 2.14. Left: Error as a function of propagation distance for the first- through fourth-order integrators, marked by the circle, square, triangle, and x, respectively, for the collision problem. Right: Deviation from initial energy as a function of propagation distance for the four integrators, also for the collision problem.

discretization is $\mathcal{O}\big(\exp(-\Delta t^{-1})\big)$ accurate for smooth functions. In this analysis, the third-order splitting method was used with $\Delta z = 0.00125$ and $T = 40$. The reduction in the rate of convergence near 8 Fourier modes per unit time is likely due to the unphysical periodic boundary conditions.

The left plot in Figure 2.14 shows the error of each of the four splitting schemes as a function of z. Note that each increase in order results in more accuracy in the pre-collision region, but the third- and fourth-order methods have different behavior in the collision region. The fourth-order integrator accumulates error through the collision, while the third-order scheme's error curve drops through the latter half of the collision, resulting in less error in the post-collision region than the fourth-order method. The NLS equation, being an integrable equation, has an infinite number

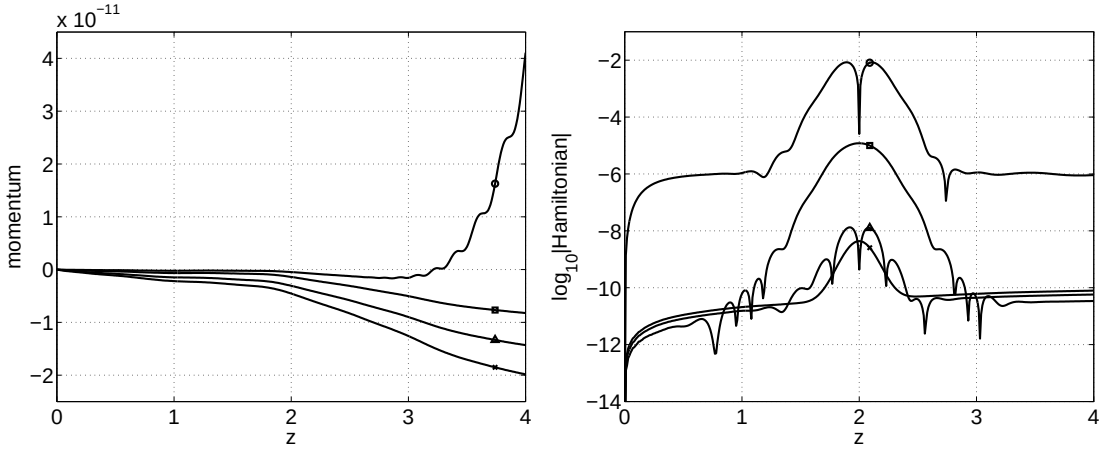

FIGURE 2.15. Deviation from initial momentum (left) and integrated Hamiltonian (right) through a soliton collision problem for first- through fourth-order integrators, marked by the circle, square, triangle, and x, respectively.

of conserved quantities. The first three of which have the physical interpretations of energy (or particle number), momentum, and integrated Hamiltonian:

$$c_1 = \int_{\mathbf{R}} |u|^2 \mathrm{d}t, \quad c_2 = \mathrm{Im} \int_{\mathbf{R}} u_t u^* \mathrm{d}t, \quad c_3 = \int_{\mathbf{R}} \big(|u_t|^2 - |u|^4 \big) \mathrm{d}t.$$

The behavior of the first of these quantities is represented in the right plot of Figure 2.13, while the second and third quantities are plotted in Figure 2.15. All four integrators conserve energy and momentum within a few parts in 10^{-11}. The difference is more evident in the Hamiltonian, where the third- and fourth-order methods perform much better in the collision region than their lower order siblings. In these simulations, the parameters $p = 10$, $T = 40$, and $\Delta z = 0.000625$ are used.

2.5.5 Convergence analysis for CQNLS

Since there is no known analytical solution for solitary wave collisions for the CQNLS equation, a complete convergence analysis for fractional step methods cannot be performed. However, exact solitary wave solutions do exist and are given by [39, 40]

$$u(t,z) = \frac{\eta_\beta \exp(i\chi_\beta)}{[\cosh^2(x_\beta - \gamma/2) - \eta_\beta^2 \epsilon \exp(\gamma - x_\beta)/3]^{1/2}},$$
$$\gamma = \log \frac{3[1-(1-4\epsilon\eta_\beta^2/3)^{1/2}]}{4\epsilon\eta_\beta^2 - 3[1-(1-4\epsilon\eta_\beta^2/3)^{1/2}]},$$

where x_β and χ_β are defined in Equation (2.15). These solutions exist for $\epsilon < 3/4\eta_\beta^2$ and have been shown to be stable [50, 51, 40]. Using $p = 10$, $T = 40$, $\epsilon = 1/2$, and integrating to $z = 2$, the convergence results for the four orders of splitting methods is shown in the left plot of Figure 2.17. The slopes of the lines are -1.00, -2.00, -3.01, and -4.01, confirming the accuracy of each method. The convergence rate of the fourth-order method is curbed near 2000 integration steps because of limitations imposed by the periodic boundary conditions enforced by the FFT.

Of course there is no analytic solution for CQNLS solitary wave collisions, otherwise there would be no reason to perform the perturbation and numerical analyses! Therefore it is impossible to determine if the numerical method is converging to the correct solution. However, good indications that it is indeed giving correct results come from the following three tests: First, it converges on the nearby ideal NLS colli-

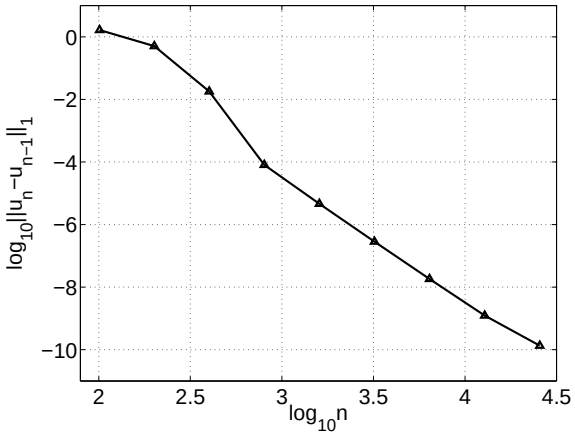

FIGURE 2.16. The log of the norm of the difference between successively refined solutions of the collision problem under CQNLS using third-order splitting. Here n indicates the number of integration steps taken to $z = 4$, where the collision takes place at $z_0 = 2$.

sion problem, which is established in the preceeding subsection. Second, it converges to *something*. This may be shown by plotting the norm of the difference of successively refined solutions against the number of integration steps used to obtain the more refined solution. This analysis is shown in Figure 2.16. The slope of the curve in the linear regime is about -3.95, indicating that the convergence rate is almost fourth order, which is consistent with the results for the ideal NLS collision problem convergence for the third-order integration method. Third, the energy, momentum, and integrated Hamiltonian are similarly conserved by CQNLS, although the latter is modified due to the additional nonlinear term:

$$c_3 = \int_{\mathbf{R}} \big(|u_t|^2 - |u|^4 + \epsilon|u|^6/3\big)\mathrm{d}t$$

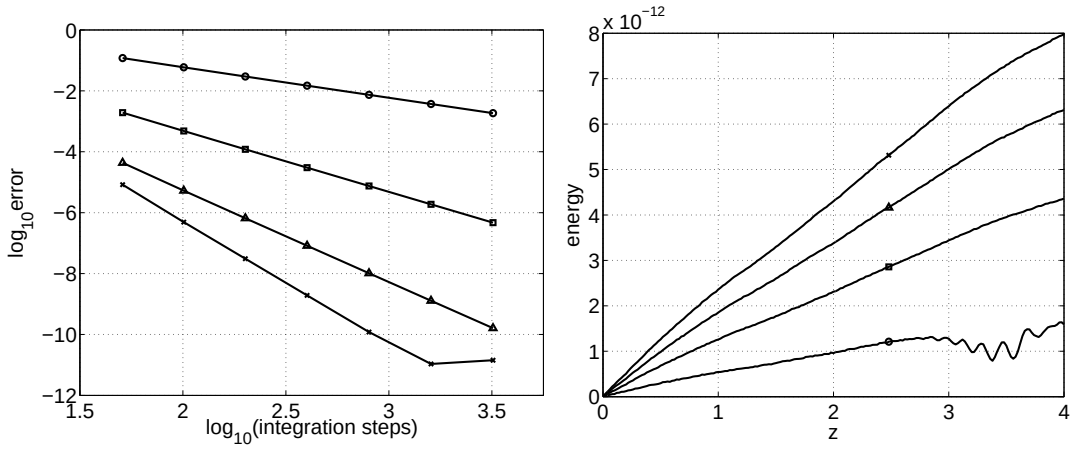

FIGURE 2.17. Left: Convergence of first- through fourth-order integrators with z-refinement, indicated by circles, squares, triangles, and x's, respectively, for the solitary wave solution of CQNLS. Right: Deviation from initial energy as a function of z for a CQNLS collision problem.

The deviation from the initial values of these three quantities is shown in the right plot of Figure 2.17 and in Figure 2.18, for all four integrators using $p = 10$, $T = 40$, $\Delta z = 0.00125$, and the relatively large value of $\epsilon = 1/2$ to ensure the influence of the high-order nonlinear term. The collision parameters in this simulation are $\eta_1 = \eta_2 = 1$, $\alpha_1 = \alpha_2 = 0$, $\beta_1 = 2$, $\beta_2 = -3$, $y_1 = -10$, and $y_2 = 10$. The result is that none of these quantities is significantly effected by the inclusion of the quintic term.

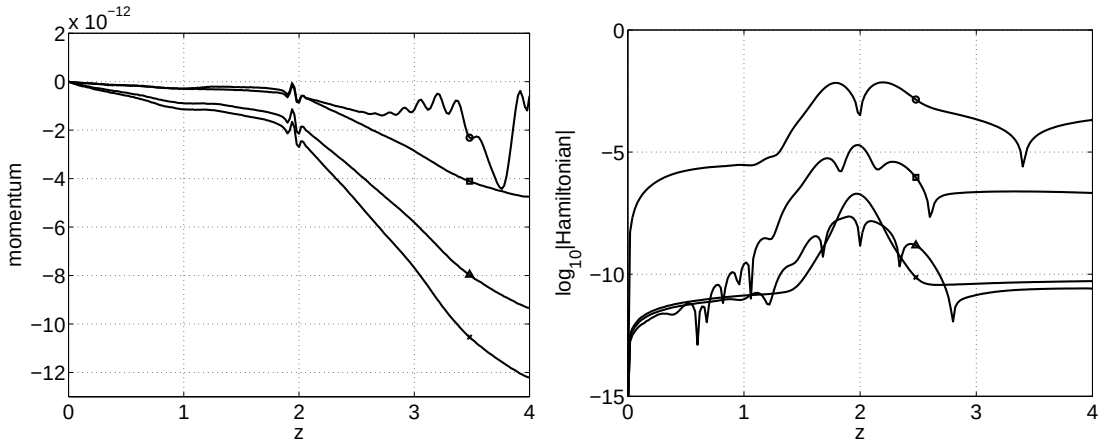

FIGURE 2.18. Deviation from initial momentum (left) and integrated Hamiltonian (right) through a CQNLS collision problem for first- through fourth-order integrators, marked by the circle, square, triangle, and x, respectively.

2.6 Comparison of perturbation theory and numerics

When all the effects up to second order in the perturbation theory are combined, the result is the following expression for the zero-channel pulse after the collision has taken place:

$$\begin{aligned}\psi_0(t,z) &= \exp\left[i\alpha_0 + i\Delta\alpha_{01}^{(0)} + i\Delta\alpha_{02}^{(1)} + i\eta_0^2 z\right] \\ &\times \left[\frac{1}{\cosh(t-\Delta y_{02}^{(0)})} + \frac{\epsilon}{6}\frac{1+\tanh(t-\Delta y_{02}^{(0)})}{\cosh(t-\Delta y_{02}^{(0)})} + v_{02}(t,z)\right].\end{aligned}$$

This expression is plotted in Figure 2.19 along with the numerical solution for a collision problem in which $\epsilon = 0.02$, $\beta = 10$, $y_0 = 0$, $y_\beta = 20$, $\eta_0 = \eta_\beta = 1$, and $\alpha_0 = \alpha_\beta = 0$. The numerical simulation was conducted using $p = 10$, $T = 60$,

$\Delta z = 0.01$, and boundary absorber function applications every 50 integration steps.

The large difference between the numerical and perturbation solutions on the right side of the first plot, corresponding to $z = z_0 + 2$, is due to the presence of the β-channel pulse which is located just out of view at $t = 40$. In the succeeding plots, corresponding to $z = z_0 + 5$ and $z = z_0 + 10$, the difference in the amplitude of the radiation diminishes with propagation distance. A common feature of these solutions is that the numerics reveal asymmetry in the radiation amplitude, which is due to the β-channel pulse approaching from the left. Since it iteracts with the left side of the zero-channel pulse first, the radiation has more "time" to disperse, resulting in a lower amplitude to the left of the pulse than to the right. The perturbation solution does not capture this effect because dispersive effects in the collision region are $\mathcal{O}(\epsilon^2/\beta)$, but it is clear that these error are of subleading order. It is, however, possible to include dispersive effects in the collision region [41]. The result is an expression which is even uglier than Equation (2.48). Its derivation is not presented here because corrections in higher orders compete with other processes which cause radiation emission such as Raman scattering, as shown in the analysis in Subsection 2.6.4. Using other system parameters which further suppress other high-order effects may extend the validity regime of CQNLS. For this reason, Figure 2.20 shows the results of this rather involved calculation. This plot shows that the reason for the asymmetric radiation profile is indeed the dispersion of radiation in the collision region. The agreement between the two solution methods is excellent.

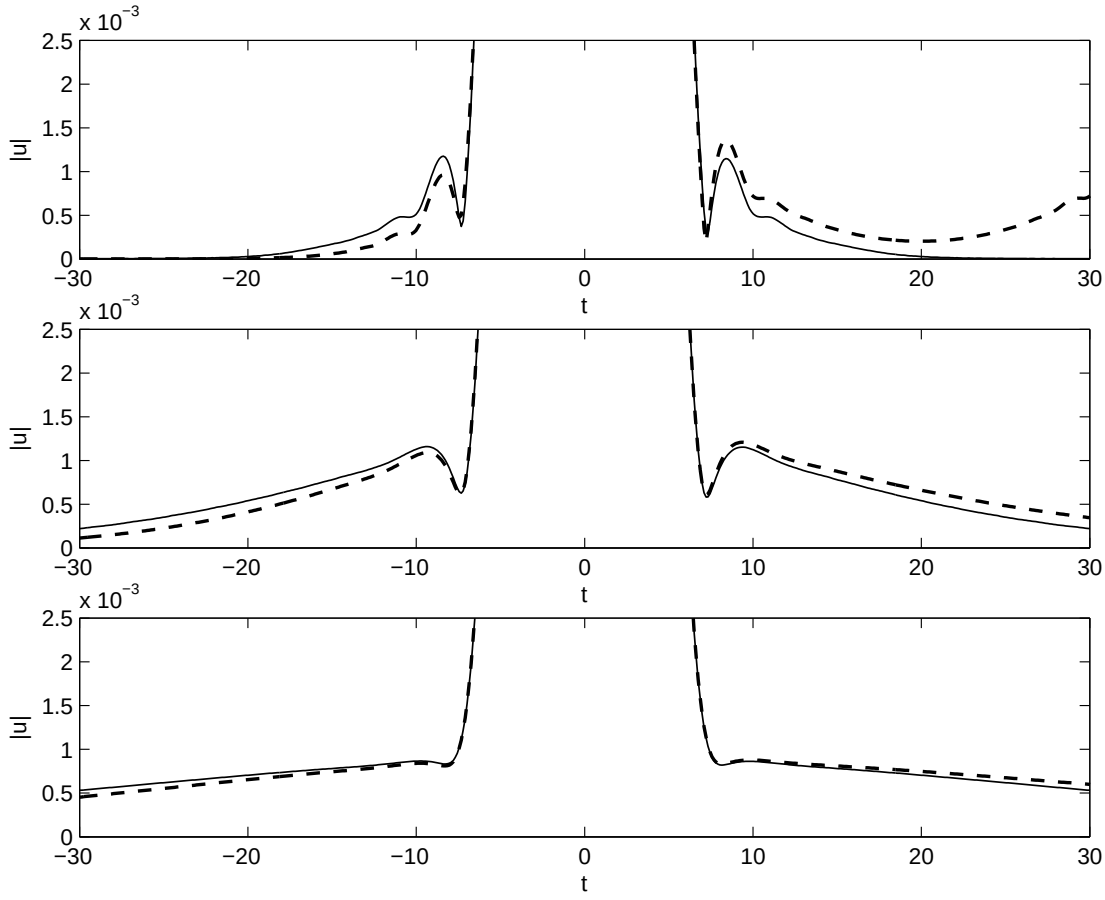

FIGURE 2.19. Second-order perturbation (solid) and numerical (dashed) solutions showing the zero-channel effects of radiation emission for $\epsilon = 0.02$ and $\beta = 10$. The three plots represent the solutions at $z = z_0 + 2$, $z = z_0 + 5$, and $z = z_0 + 10$, top to bottom.

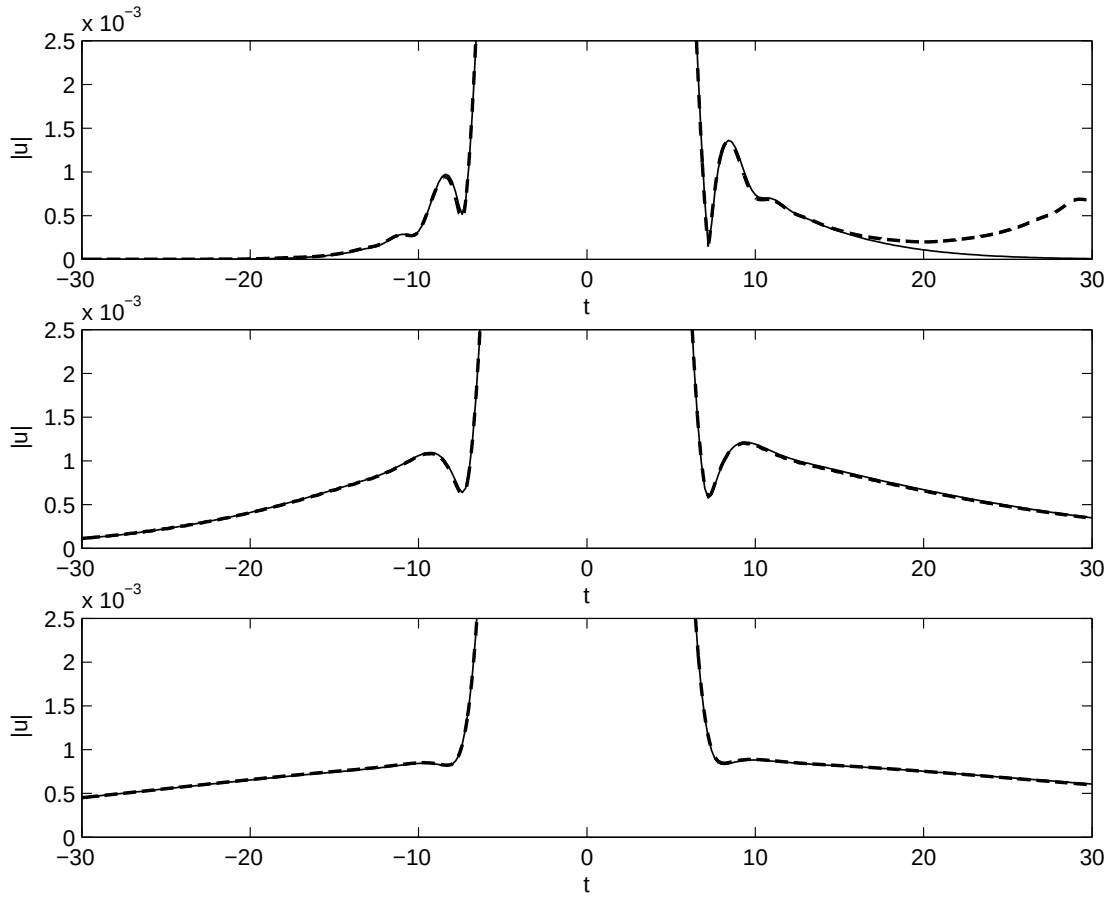

FIGURE 2.20. Perturbation (solid) and numerical (dashed) solutions in analogy with Figure 2.19, but taking dispersion in the collision region into account.

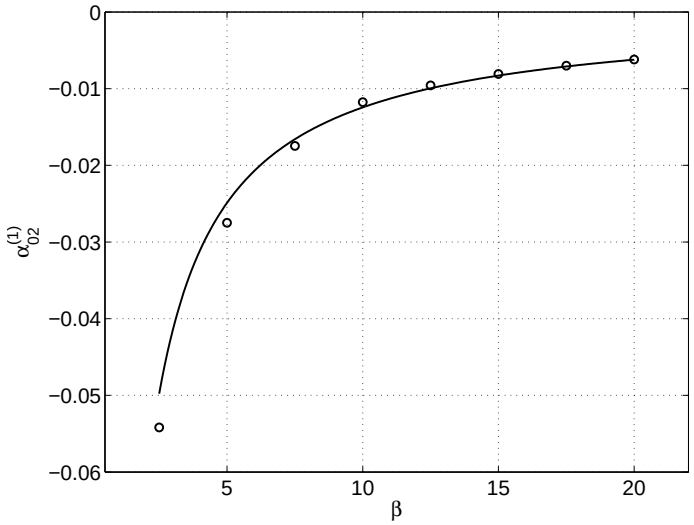

FIGURE 2.21. Leading order quintic nonlinearity-induced phase shift as a function of β for $\epsilon = 0.02$. The circles indicate data points measured from numerical solutions and the line indicates the predictions of the perturbation theory.

To compare the perturbation theoretical prediction of $\mathcal{O}(\epsilon/\beta)$ phase shift with numerics, the phase of the zero-channel pulse must be accurately measured in the simulation. This is done by interpolating the pulse peak using a quadratic polynomial, which allows the time coordinate of the peak to be determined more accurately than simply choosing the meshpoint for which the amplitude is highest. The phase is measured by taking the arctangent of the ratio of imaginary and real parts of this polynomial and then subtracting off the integration distance z, consistent with χ_0. The results of these measurements along with the theoretical predictions are plotted in Figure 2.21. Note that even for small β the agreement is quite good, with a phase shift inaccuracy of 10% at $\beta = 2.5$.

2.7 Conclusions

In this chapter, optical soliton collisions are studied in the presence of weak quintic nonlinearity. The dynamics of the collision-induced emitted radiation and the changes in the soliton parameters are determined. This analysis is performed using a double perturbation theory in two small parameters: the coefficient of the quintic nonlinear term ϵ, and the reciprocal of the relative frequency of the two colliding solitons $1/\beta$. The amplitude of emitted radiation is found to be proportional to ϵ/β. It is also found that the only other effect of the collision up to second order in the perturbation theory is an additional phase shift, proportional to ϵ/β. The results of this theory are in very good agreement with the results obtained via numerical simulations of the cubic-quintic NLS equation.

Chapter 3

Polariton dynamics in resonant nanocomposite media

At this point in the dissertation, the focus is shifted from nonresonant dynamics of optical pulses in waveguides, where the origin of the nonlinearity is the intensity dependence of the refractive index, to resonant interaction in waveguides, in which case the nonlinearity results from material excitation in response to the optical field. It is well known that adding active inclusions to optical waveguides results in useful phenomena employable in many devices such as erbium doped fiber amplifiers, lasers, pulse generators, etc. A new kind of active inclusion may now be used due to recent advances in nanofabrication, namely metallic nanoparticles. These tiny metallic particles induce new waveguide phenomena which have potential applications in a variety of scientific and engineering fields. The material under consideration here is a nanocomposite consisting of metallic nanoparticles embedded in a host medium. The conduction electrons of a metallic nanoparticle (known collectively as a plasmon) are displaced from their equilibrium positions in response to an applied optical field. If the field is switched off, a restoring force returns the plasmon to its equilibrium in

an oscillatory fashion. Thus the metallic nanoparticles may be viewed as oscillators which have a certain natural oscillation frequency. Since the nanoparticles are so small, quantum effects induce a nonlinearity on the restoring force and the oscillations are anharmonic. If the optical carrier wave is in resonance with the plasmon oscillation frequency, the resonance condition is satisfied and the coupling between the material polarization induced by the nanoparticles and the optical field becomes strong. This facilitates energy exchange between the optical and polarization fields. This energy exchange can lead to the existence of mixed modes of the optical and polarization fields (solitary waves) known as *polaritons*. This term was originally used in the description of resonant interaction of optical pulses and two-level media, but is appropriate for resonant interaction with nanostructured optical media as well.

3.1 Nanostructured optical media

Over the last decade many advancements in the manipulation of light have been made using structures whose characteristics vary on the micrometer scale, the same scale as the wavelength of light in the optical domain. Such structures include photonic crystal fibers, distributed Bragg reflectors, resonant optical cavities, and many others. More recent experimental work has demonstrated a great capacity for controlling light on the nanometer scale through the use of nanostructured materials. One tool for light manipulation is the nonlinearity induced by the material, which may be controlled

very well using nanocomposite materials. The ability to affect the behavior of light on very small length scales is important for designing new photonic devices with potential applications in information transmission and processing, subwavelength imaging, and medicine.

Nonlinear optics has played a huge role in the development of photonics, however standard materials exhibit a relatively weak nonlinear response. Thus, high intensities are required to acheive nonlinear effects, which limits the practicability of devices using these technologies. In particular, it is difficult to use nonlinearity-based optical micorchip technologies with standard materials. Nanostructured materials offer the potential for these nonlinearity-based devices on integrated optical chips. Recent developments in fabrication technologies have made it possible to design *nanocomposite* materials, or materials whose structure varies on the subwavelength, nanometer scale. These exciting new materials are capable of achieving much higher effective nonlinear response characteristics through resonant interactions with the optical field. The subject of this research is nonlinear optical pulse dynamics in a simple nanocomposite medium, one which consists of a host medium, such as glass, that has been doped with a uniform distribution of metallic nanoparticles.

3.1.1 Surface plasmon oscillations on metallic nanoparticles

Recent studies of the nonlinear response of nanoscale metallic particles [52, 53] predict an enhancement of optical nonlinearity due to quantum effects in the resonant

interaction between the optical field and plasmonic oscillations (oscillations of the electron cloud). Since metallic nanoparticles are small enough to be considered quantum objects, an accurate description of their interaction with an optical field requires that quantum effects be taken into account. In reference [53], the quantum effects are accounted for by modeling a metallic nanoparticle using the Schrödinger equation with an infinitely deep spherical shell potential. This model is used to calculate the nonlinear response resulting from multiphoton processes. It was shown that in leading order, quantum effects induce a cubic nonlinear response. These predictions [53] were subsequently confirmed with experiment [54]. The size-dependence of optical nonlinearity was also studied, and effective $\chi^{(3)}$ values of $\sim 10^{-12}(\mathrm{m/V})^2$ have been predicted for 10nm Ag particles [55], which is approximately 10 orders of magnitude higher than the Kerr effect in $Si0_2$.

The natural oscillation frequency of metallic particles is only weakly dependent of size in the 5-50nm range, but depends strongly on the shape and orientation relative to the polarization of the electric field [56]. For an ensemble of nanoparticles, this dependence results in broadening of the resonance linewidth, which peaks at $\lambda_r =$ 400nm and is 8nm wide at half maximum [56].

The number density of conduction electrons is an important constant in this analysis, and determining it requires some basic results from solid state physics. The crystalline structure of both Ag and Au is face centered cubic with the unit cell having length of 408.53pm for Ag and 407.82pm for Au [57]. Thus the volume of their unit

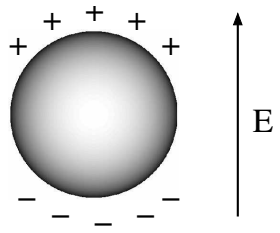

FIGURE 3.1. Charge distribution on a metallic particle in the presence of an electric field.

cells are 0.0682nm^3 and 0.0678nm^3, respectively. The unit cell for the FCC structure has one atom located at each vertex of the cube and one atom centered on each face. One eigth of each vertex atom and one half of each face atom lies within the unit cell. With eight vertices and six faces, this means that each unit cell contains four atoms. This gives the number densities $N \simeq 59$Ag atoms/nm^3 and $N \simeq 58$Au atoms/nm^3. Thus a sphere of radius a contains about $246a^3$ Ag atoms. For example, a 10nm sphere contains about 3.1×10^4 Ag atoms, while a 100 nm sphere contains about 3.1×10^7 Ag atoms. Both Ag and Au donate one electron to the conduction band, so there are as many free electrons per unit volume.

When exposed to an electric field, conduction electrons in a metallic particle redistribute themselves on the surface, inducing a charge separation (see Figure 3.1). This redistribution creates a restoring force which opposes the charge separation and leads to oscillatory behavior of the charge distribution. If the size of the particle is much smaller than the wavelength of light, spatial dynamics of individual electrons may be ignored and the charge cloud oscillations may be described in terms of a

time-dependent ordinary differential equation.

In order to model the dynamics of plasmonic oscillation, it is important to understand and analyze the many relaxation processes involved. Plasmonic oscillation is a complex process which has many characteristic relaxation times. To model this phenomenon, it is important to understand the physical processes involved so that the regime of validity of the model may be identified. The relaxation processes in plasmonic oscillation dynamics can be represented by the following time-heirarchical structrue:

1. Coherency decay time $\tau_c \sim$ 6fs. This is the time it takes for a nanoparticle's coherent plasmon to decay to an ensemble of individual single-electron excitations [58, 59, 60, 61, 62, 63]. This causes broadening of the spectral line, similar to homogeneous broadening in spectroscopy.

2. Electron thermalization time $\tau_T \sim$ 400fs. This is the transistion time from nonequilibrium electron excitations to the equilibrium Fermi distribution as the result of mutual electron interaction [64, 65].

3. Phonon excitation time $\tau_{ph} \sim 3 - 5$ps. Electrons eventually excite the metal ion lattice of the nanoparticle, transfering energy to it via lattice vibrations (phonons) [66, 67, 68, 64].

The subject of this investigation is processes which are shorter than thermalization time τ_T but longer than the limit of applicability of the slowly varying envelope

approximation, which is approximately 100fs.

In leading order, plasmonic oscillations in metallic nanoparticles can be represented in terms of a harmonic oscillator equation forced by the external electric field. Quantum effects result in an additional cubic term which corresponds to the well-known Duffing oscillator equation. In the general, the coefficient of cubic nonlinearity is complex, therefore the oscillator dynamics are described by a complex Duffing equation. Experiments show that the real part of coefficient of nonlinearity is much larger than the imaginary part [69], so in this analysis only a purely real coefficient is considered. However, the effects of the imaginary part, which correspond to absorption processes, should be investigated in future work. The inclusion of the imaginary part could lead to different dyanmics, as is the case with the complex Ginzburg-Landau equation and its purely real analog [70].

3.1.2 Properties of nanocomposite medium

For practical purposes, metallic nanoparticles are embedded in an optical host material, forming a composite medium. This introduces a mutual interaction between the nanoparticles and the host. It is known from experiments that the charactersitic time of energy transfer between the two constituents of the composite medium is 50-100ps [71]. This timescale is very well separated from the pulse durations considered here. Thus the energy exchange across material interfaces has a negligible effect on ultrashort pulses. Although the host material has an effect on group velocity, dispersion,

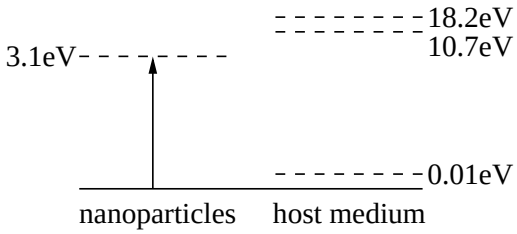

FIGURE 3.2. Energy level diagram for composite medium consisting of metallic nanoparticles and $Si0_2$ host medium, where the energies are shown on a logarithmic scale. The arrow indicates the energy of the photons in the optical field in resonance with the nanoparticles.

and off-resonant nonlinear processes, the physics of the resonant interaction of an ultrashort pulse and the plasmonic oscillations is invariant to the type of host material, as long as its atomic resonance frequencies are well separated from the plasmonic oscillation frequency. The host medium may be solid or liquid; the latter is used in experiments to facilitate parameter control, fabrication, and testing [54]. An example of a solid host medium is $Si0_2$, which is suitable since its atomic resonance frequencies are 68nm, 116nm, and 9896nm [72], all of which are well separated from the 400nm resonance of the nanoparticles. An energy level diagram for a composite medium consisting of metallic nanoparticles embedded in $Si0_2$ appears on a logarithmic scale in Figure 3.2.

The skin depth (distance at which the field is attenuated to $1/e$) or penetration depth of good conductors is 10-20nm at optical wavelengths. But due to the composite nature of the medium and the subwavelength dimension of the nanoparticles, the penetration depth of a typical bulk composite medium is approximately 10cm [69],

although this depends on the volume fraction of the composite material occupied by metal, denoted by p. In this analysis only composites with $p \ll 1$ are considered. Under this condition, backscattering and the consequent counterpropagating field are weak. Moreover, the scales on which the oppositely-directed fields interact are much smaller than those of the optical pulse interacting with the material. Thus the counterpropagating may be ignored and a unidirectional approximation is valid.

There are two ways to approach this problem. The first is on the level of each individual nanoparticle. This approach is intractible because it involves too much scale disparity, as well as a three-dimensional model. The more practicable approach used in light interaction problems is to employ an effective medium approximation, in which effective parameters are obtained by averaging over the small scales in the problem, including the transverse structure of the field, which allows a one-dimensional model to capture the relevant dynamics. The effective medium approximation requres the condition $pN\lambda_0^3 \gg 1$, where N is the density of free electrons in the metal and λ_0 is the carrier wavelength. This condition ensures that the average distance between nanoparticles is much smaller than the wavelength of light. Thus the local fields generated by plasmonic oscillations in nanoparticles (characterized by an interaction distance r_{int}) do not interact with one another. This allows nanoparticle coupling to be neglected and field coherency is preserved [73]. A composite medium in which both conditions ($p \ll 1$ and $pN\lambda_0^3 \gg 1$) are satisfied is depicted in Figure 3.3.

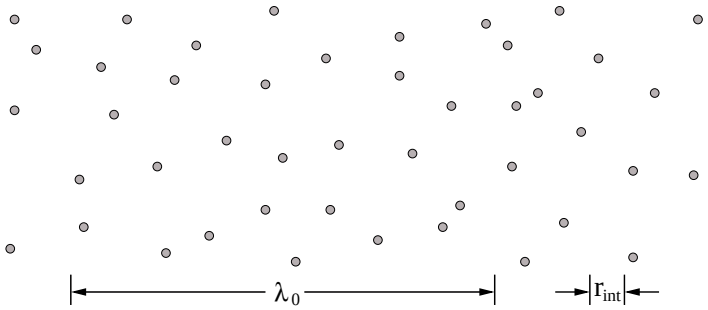

FIGURE 3.3. Distribution of metallic nanoparticles in a composite medium for which $p \ll 1$ and $N\lambda_0^3 \gg 1$. The carrier wavelength λ_0 and the characteristic distance of local nanoparticle field interaction r_{int} are indicated.

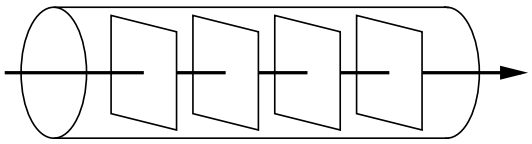

FIGURE 3.4. Unidirectional plane waves propagating in a cigar-shaped sample.

3.2 Model equations

In order to model optical pulse dynamics in the nanocomposite medium described in the previous section, equations must be derived from first principles using valid approximations which preserve the dynamics of interest and take all the influencing effects into account. The equations must model plane wave propagation in a cigar-shaped nanocomposite sample (commonly used in experiments and devices when diffraction may be neglected [74]) as depicted in Figure 3.4. The model equations must describe the resonant interaction of optical pulses with plasmonic oscillations in metallic nanoparticles while taking the following considerations into account:

1. both electric and material excitation field envelopes as functions of time and propagation distance
2. cubic nonlinearity of resonant interaction
3. averaged effective medium parameters

The model must also neglect the small contributions due to:

1. transverse field components
2. nanoparticle-nanoparticle interaction
3. interaction with a counterpropagating field

The derivation of the electric field envelope equation is largely the same as it appears in Section 2.1, beginning with the scalar Maxwell wave equation (2.1), with the exception that the polarization of the composite material has two contributions, one from the nonresonant response of the bulk medium $\tilde{P}_b$, which has the same form as Equation (2.3), and one from the plasmonic oscillations in the metallic nanoparticles $\tilde{P}_n$. Thus the total polarization is given by $\tilde{P} = \tilde{P}_b + \tilde{P}_n$. The polarization induced by the nanoparticles is modeled by considering the individual plasmonic oscillations and then averaging over the ensemble of nanoparticles in the composite medium. To leading order, the equation of motion for the effective coordinate of the center of

charge in a single metallic nanoparticle is

$$\frac{\partial^2 \tilde{Q}}{\partial t^2} + 2\gamma \frac{\partial \tilde{Q}}{\partial t} + \omega_p^2 \tilde{Q} - \kappa \tilde{Q}^3 = \frac{e}{m} \tilde{E}. \tag{3.1}$$

This equation is known as the forced and damped Duffing oscillator, in which t is time, γ is the decay rate for plasmonic oscillations, κ is the nonlinearity coefficient, ω_p is the angular frequency of low-amplitude plasmonic oscillation, and e and m are electron charge and rest mass [75]. The numerical value of κ varies according to the nanoparticle material and structure. The parameters γ, ω_p, and κ (all real and positive) vary from nanoparticle to nanoparticle due to different orientations in the composite medium. Current fabrication techniques are not precise enough to control the precise size and shape of the nanoparticles, so this randomness must be taken into account. This is done by introducing a distribution of γ, ω_p, and κ parameter values. The polarization of the electric field also has an effect on the resonance. In this analysis, a linearly polarized field is considered, but modeling propagation in a noncircular waveguide would require both polarization states to be taken into account.

Both the electric and material excitation fields vary on the scale of the carrier wavelength. However, the dynamics of interest here vary on the scale of the pulse envelope, which is characterized by a much slower and longer scale. With such a separation of scales, a slowly varying envelope approximation may be applied to

obtain simpler equations. Thus a quasimonochromatic wavepacket in the material excitation field is factorized as

$$\tilde{Q}(t,z) = Q(t,z)\exp\big[i(k_0 z - \omega_0 t)\big] + \text{complex conjugate.} \tag{3.2}$$

Applying this ansatz to Equation 3.1 and collecting terms oscillating at k_0, ω_0 results in the envelope equation

$$\frac{\partial^2 Q}{\partial t^2} - 2i\omega_0\frac{\partial Q}{\partial t} - \omega_0^2 Q + 2\gamma\left(\frac{\partial Q}{\partial t} - i\omega_0 Q\right) + \omega_p^2 Q - 3\kappa|Q|^2 Q = \frac{e}{m}E.$$

Consideration is given to the case when detuning from the plasmonic resonance frequency is small, so that $\omega_p^2 - \omega_0^2 = (\omega_p + \omega_0)(\omega_p - \omega_0) \simeq 2\omega_0(\omega_p - \omega_0)$. And since the envelope varies far more slowly than the underlying carrier wave, $|Q_{tt}| \ll \omega_0|Q_t|$ and $|Q_t| \ll \omega_0|Q|$. These separations in scale allow the reduction to

$$i\frac{\partial Q}{\partial t} - (\omega_p - \omega_0)Q + i\gamma Q + \frac{3\kappa}{2\omega_0}|Q|^2 Q = -\frac{e}{2m\omega_0}E. \tag{3.3}$$

These displacements in charge distributions in the metallic nanoparticles are related to the polarization by

$$P_n(t,z) = \frac{Npe}{\epsilon_0}\int_{\mathbf{R}^3} Q(t,z;\omega_p,\gamma,\kappa)g(\omega_p,\gamma,\kappa)\mathrm{d}\omega_p\mathrm{d}\gamma\mathrm{d}\kappa, \tag{3.4}$$

where N is the number of conduction electrons per unit volume of metal and p is the filling factor, which is the fraction of the composite medium occupied by the metallic nanoparticles. The function g describes the distribution of nanoparticle resonance frequencies, damping, and nonlinearity coefficients, and is normalized so that

$$\int_{\mathbf{R}^3} g(\omega_p, \gamma, \kappa) \mathrm{d}\omega_p \mathrm{d}\gamma \mathrm{d}\kappa = 1.$$

The compact notation $P_n = Npe \langle Q \rangle / \epsilon_0$ is used to indicate the average over all nanoparticle parameters.

Because of the additional polarization effect of the metallic nanoparticles, the derivation of the electic field envelope equation is slightly different from that given in Section 2.1. Equation (2.1) is rewritten as

$$\left(\frac{\partial^2}{\partial z^2} - \frac{1}{c^2} \frac{\partial^2}{\partial t^2} \right) \tilde{E} = \frac{1}{c^2} \frac{\partial^2}{\partial t^2} \left(\tilde{P}_b^L + \tilde{P}_b^{NL} + \frac{Npe}{\epsilon_0} \langle \tilde{Q} \rangle \right),$$

where the polarization due to the nonresonant interaction with the bulk medium has been split onto linear and nonlinear contributions. Then the frequency domain representation of this equation, in analogy with Equation (2.4), is given by

$$\left[\frac{\partial^2}{\partial z^2} + \frac{\omega^2}{c^2} \left(1 - \chi^{(1)} \right) \right] \tilde{E} = -\frac{\omega^2}{c^2} \left(\tilde{P}_b^{NL} + \frac{Npe}{\epsilon_0} \langle \tilde{Q} \rangle \right).$$

In a slowly varying envelope approximation, the factorizations (2.6) and (3.2) yield

$$\left[i\frac{\partial}{\partial z} + k(\omega) - k_0\right] E = -\frac{\omega_0^2}{2c^2 k_0}\left(P_b^{NL} + \frac{Npe}{\epsilon_0}\langle Q\rangle\right).$$

Applying a second-degree Taylor polynomial approximation to the dispersion relation and returning to the time domain results in

$$\left(i\frac{\partial}{\partial z} + ik'\frac{\partial}{\partial t} - \frac{k''}{2}\frac{\partial^2}{\partial t^2} + \frac{\omega_0 n_2}{c}|E|^2\right) E = -\frac{Npe\omega_0}{2\epsilon_0 c n_0}\langle Q\rangle, \tag{3.5}$$

where the nonlinear contribution to the polarization is consistent with Equation (2.8). Equations (3.3) and (3.5) describe optical pulse propagation in a resonant nanocomposite medium in a one-dimensional, unidirectional, slowly-varying envelope approximation. They are a nonlinear generalization of the well-known Maxwell-Lorentz model [73], which was used to describe the resonant linear interaction of an electric field with an absorbing medium without taking quantum effects into account. In analogy with this system, Equations (3.3) and (3.5) are hereafter referred to as the Maxwell-Duffing (MD) equations.

3.3 Dimensional analysis

In order to evaluate the strength of each term in the MD equations (3.3) and (3.5) and to identify terms which may be neglected, they must be written in dimensionless

form. Then the magnitude of the coefficients of all the terms may be compared by plugging in real parameter values from the physical system. The control parameters for this system include the carrier wavelength λ_0, the nanoparticle radius a, the filling factor p, the peak field intensity I_0, and the pulse width τ_0.

Moving to a copropagating reference frame and scaling distance, time, and the field amplitudes using the transformations

$$z = z_0\zeta - \tau_0\tau/k', \quad t = \tau_0\tau, \quad E = -E_0\mathcal{E}, \quad Q = Q_0\mathcal{Q}$$

results in the dimensionless system

$$i\frac{\partial\mathcal{E}}{\partial\zeta} - \frac{z_0}{\tau_0^2}\frac{k''}{2}\frac{\partial^2\mathcal{E}}{\partial\tau^2} + z_0E_0^2\frac{\omega_0 n_2}{c}|\mathcal{E}|^2\mathcal{E} = \frac{z_0Q_0}{E_0}\frac{Npe\omega_0}{2\epsilon_0 cn_0}\langle\mathcal{Q}\rangle \tag{3.6}$$

$$i\frac{\partial\mathcal{Q}}{\partial\tau} - \tau_0(\omega_p - \omega_0)\mathcal{Q} + i\tau_0\gamma\mathcal{Q} + \tau_0q_0^2\frac{3\kappa}{2\omega_0}|\mathcal{Q}|^2\mathcal{Q} = \frac{\tau_0E_0}{Q_0}\frac{e}{2m\omega_0}\mathcal{E}. \tag{3.7}$$

In this form characteristic distances may be extracted for coupling z_c, nonlinearity z_{nl}, and dispersion z_d. Similarly, characteristic times for coupling τ_c, nonlinearity τ_{nl}, and damping τ_d are identified. These scales are

$$z_c = \frac{2E_0\epsilon_0 n_0 c}{Q_0 Nep\omega_0} \qquad \tau_c = \frac{2Q_0 m\omega_0}{E_0 e}$$

$$z_{nl} = \frac{c}{E_0^2\omega_0 n_2} \qquad \tau_{nl} = \frac{2\omega_0}{3Q_0^2\kappa}$$

$$z_d = \frac{2\tau_0^2}{|k''|} \qquad \tau_d = \frac{1}{\gamma}$$

The nonlinear response of the nanoparticles is anticipated to be much larger than either the host material nonlinearity or dispersion, so the charactersitic length scale is chosen to be the coupling length, $z_0 = z_c$. Similarly, the characteristic time scale is chosen to be the coupling time $\tau_0 = \tau_c$. Note that selecting this time scale establishes the characteristic pulse duration as well. Equations (3.6) and (3.7) then become

$$
\begin{aligned}
&i\frac{\partial \mathcal{E}}{\partial \zeta} - \frac{z_c}{z_d}\frac{\partial^2 \mathcal{E}}{\partial \tau^2} + \frac{z_c}{z_{nl}}|\mathcal{E}|^2\mathcal{E} = \langle \mathcal{Q} \rangle \\
&i\frac{\partial \mathcal{Q}}{\partial \tau} - \tau_c(\omega_p - \omega_0)\mathcal{Q} + i\tau_c\gamma\mathcal{Q} + \frac{\tau_c}{\tau_{nl}}|\mathcal{Q}|^2\mathcal{Q} = \mathcal{E},
\end{aligned}
$$

where all the coefficients have been expressed as ratios of characteristic lengths and times. Since the material field amplitude Q_0 is determined by the amplitude of the electric field in the composite medium, it should be expressed in terms of other physical constants and control parameters. This is accomplished by setting the coefficient of the $|\mathcal{Q}|^2\mathcal{Q}$ term equal to unity, which results in

$$
Q_0 = \left(\frac{E_0 e}{3m\kappa}\right)^{1/3}. \tag{3.8}
$$

Constraining the scaling in this way is consistent with the expected large nonlinear response of the material, so this term certainly should not be neglected. Using Equation (3.8) along with the relations $E_0^2 = 2I_0/\epsilon_0 n_0 c$, $\omega_0 = 2\pi c/\lambda_0$, and $\kappa = (ma\omega_0^2/\hbar)^2$ [76] results in the following expressions for the coefficients in terms of physical constants

and control parameters:

$$\frac{z_c}{z_{nl}} = \alpha = \bar{\alpha}\left(\frac{a^2 I_0^4}{p^3\lambda_0^4}\right)^{1/3} \qquad \frac{z_c}{z_d} = D = \bar{D}\frac{I_0 a^2}{p\lambda_0}$$
$$\tau_c(\omega_p - \omega_0) = -\delta = \bar{\delta}\frac{\lambda_0 - \lambda_p}{I_0 a^2 \lambda_0^2} \qquad \tau_c\gamma = \Gamma = \bar{\Gamma}\left(\frac{\lambda_0}{I_0 a^2}\right)^{1/3}$$

where the overbarred constants are given by

$$\bar{\alpha} = \left(\frac{6144\pi^4}{e^4\epsilon_0 n_0 \hbar}\right)^{1/3}\frac{n_2 m}{N} = 3.50\times 10^{-28}\mathrm{C}^{-2}(\mathrm{Kg\ m})^{-1/3}$$
$$\bar{D} = \frac{3\pi|k''|mc}{N\hbar} = 5.80\times 10^{-25}\mathrm{m\ s}^2$$
$$\bar{\delta} = \left(\frac{16\pi^2\epsilon_0 n_0}{3e^2}\right)^{1/3}\frac{c}{\lambda_p} = 9.15\times 10^{7}(\mathrm{Kg\ m})^{1/3}\mathrm{s}^{-1}$$
$$\bar{\Gamma} = \left(\frac{2\epsilon_0 n_0 \hbar^2}{3\pi e^2}\right)^{1/3}\gamma = 5.25\times 10^{-3}(\mathrm{Kg\ m})^{1/3}\mathrm{s}^{-1}$$

These constants were computed using typical values for SiO_2 (which would be unaffected by the dilute inclusions [69]): $k'' = 0.14\mathrm{ps}^2/\mathrm{m}$, which is measured [1] at $\lambda_p = 400\mathrm{nm}$, as well as $1/\gamma = 2\mathrm{ps}$, $n_0 = 1.444$, $n_2 = 1.22\times 10^{-22}(\mathrm{m/V})^2$, and $N = 59\mathrm{nm}^{-3}$. The system may now be written

$$i\frac{\partial\mathcal{E}}{\partial\zeta} - D\frac{\partial^2\mathcal{E}}{\partial\tau^2} + \alpha|\mathcal{E}|^2\mathcal{E} = \langle\mathcal{Q}\rangle$$
$$i\frac{\partial\mathcal{Q}}{\partial\tau} + \delta\mathcal{Q} + i\Gamma\mathcal{Q} + |\mathcal{Q}|^2\mathcal{Q} = \mathcal{E},$$

[1] This data for k'' at 400nm was extrapolated using the zero dispersion wavelength $k'' = 0$ at $\lambda =$ and $k'' = 0.12\mathrm{ps}^2/\mathrm{m}$ at 530nm [77].

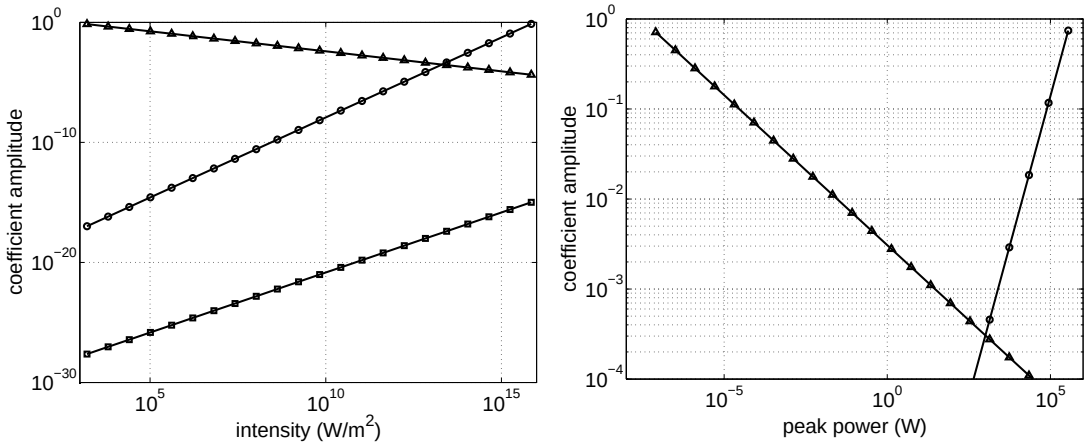

FIGURE 3.5. Dependence of coefficients α (circles), D (squares), and Γ (triangles) on intensity and peak power using typical parameters $a = 10$nm, $\lambda_0 = 400$nm, and $p = 0.1\%$. The peak power was computed from intensity by multiplying by a fiber core area of $50\mu\text{m}^2$.

and the coefficients are plotted as a function of peak field intensity and peak power in Figure 3.5. The figure shows that by transversely confining the field in a waveguide with core area $50\mu\text{m}^2$ and using the indicated values for the control parameters, the effects of damping and host material nonlinearity and dispersion have less than a 1% effect for peak pulse powers in the range 50mW-4KW. This is easily attainable using, for example, a semiconductor laser source. Using these parameter values and pulses with peak power of 1W, the characteristic coupling distance $z_c = 1.5\mu$m.

3.4 Equation properties

In this section the simplified case of identically distributed spherical metallic nanoparticles, or nanospheres, is considered. Since their identical geometries result in identical nonlinear response and plasmonic resonance frequencies, the function g in Equation (3.4) is the Dirac delta function. Thus the MD equations reduce to

$$i\frac{\partial \mathcal{E}}{\partial z} = \mathcal{Q} \tag{3.9}$$

$$i\frac{\partial \mathcal{Q}}{\partial t} + \delta\mathcal{Q} + |\mathcal{Q}|^2\mathcal{Q} = \mathcal{E}. \tag{3.10}$$

This system possesses three invariants. Shifting the coordinates $z \to z+z_0$ or $t \to t+t_0$ does not change the form of the equations, hence spatial and temporal invariance. Also, a simultaneous constant phase shift in $\mathcal{E}$ and $\mathcal{Q}$, i.e., $\mathcal{E} \to \mathcal{E}e^{i\phi}$ and $\mathcal{Q} \to \mathcal{Q}e^{i\phi}$, do not effect the equations, which is known as Gauge invariance.

These equations possess three conservation laws. The first of these is energy conservation, which is obtained in the following way: first, Equation (3.9) is multiplied through by $\mathcal{E}^*$ and subtracted from its complex conjugate, resulting in

$$i\frac{\partial}{\partial z}|\mathcal{E}|^2 = \mathcal{E}^*\mathcal{Q} - \mathcal{E}\mathcal{Q}^*.$$

Equation (3.10) is multiplied by $\mathcal{Q}^*$ and subtracted from its complex conjugate to

obtain

$$i\frac{\partial}{\partial t}|\mathcal{Q}|^2 = -\mathcal{E}^*\mathcal{Q} + \mathcal{E}\mathcal{Q}^*.$$

Equating these expressions yields the conservation law

$$\frac{\partial}{\partial z}|\mathcal{E}|^2 + \frac{\partial}{\partial t}|\mathcal{Q}|^2 = 0, \tag{3.11}$$

The other conserved quantities are derived using standard manipulations. The second law is obtained by differentiating Equation (3.10) with respect to z, multiplying through by $\mathcal{Q}^*$ and subtracting its complex conjugate, which results in

$$i\big(\mathcal{Q}_{tz}\mathcal{Q}^* + \mathcal{Q}^*_{tz}\mathcal{Q}\big) + \big(\delta + |\mathcal{Q}|^2\big)\big(\mathcal{Q}_z\mathcal{Q}^* - \mathcal{Q}^*_z\mathcal{Q}\big) = \mathcal{E}_z\mathcal{Q}^* - \mathcal{E}^*_z\mathcal{Q}. \tag{3.12}$$

Another expression is obtained by multiplying Equation (3.10) by $\mathcal{Q}^*_z$ and subtracting its complex conjugate, which yields

$$i\big(\mathcal{Q}_t\mathcal{Q}^*_z + \mathcal{Q}^*_t\mathcal{Q}_z\big) - \big(\delta + |\mathcal{Q}|^2\big)\big(\mathcal{Q}_z\mathcal{Q}^* - \mathcal{Q}^*_z\mathcal{Q}\big) = \mathcal{E}\mathcal{Q}^*_z - \mathcal{E}^*\mathcal{Q}_z. \tag{3.13}$$

Equations (3.12) and (3.13) are added together to obtain

$$\mathcal{Q}^* \left(|\mathcal{Q}|^2\mathcal{Q}\right)_z - \mathcal{Q}\left(|\mathcal{Q}|^2\mathcal{Q}^*\right)_z + |\mathcal{Q}|^2\mathcal{Q}\mathcal{Q}_z^* - |\mathcal{Q}|^2\mathcal{Q}^*\mathcal{Q}_z$$
$$+i\left(\mathcal{Q}_t^*\mathcal{Q}_z + \mathcal{Q}^*\mathcal{Q}_{tz} + \mathcal{Q}_t\mathcal{Q}_z^* + \mathcal{Q}^*\mathcal{Q}_{tz}\right) = \mathcal{E}_z\mathcal{Q}^* - \mathcal{E}_z^*\mathcal{Q} + \mathcal{E}\mathcal{Q}_z^* - \mathcal{E}^*\mathcal{Q}_z.$$

Here the first line reduces to zero, the next term is $|\mathcal{Q}|_{tz}^2$, and the right hand side is $(\mathcal{E}\mathcal{Q}^* - \mathcal{E}^*\mathcal{Q})_z$. This yields the second conservation law, which in flux/density form reads

$$\frac{\partial}{\partial z}\left(\mathcal{E}^*\mathcal{Q} - \mathcal{E}\mathcal{Q}^*\right) + i\frac{\partial}{\partial t}\left(\frac{\partial}{\partial z}|\mathcal{Q}|^2\right) = 0 \tag{3.14}$$

The third conservation law is derived by differentiating Equation (3.10) with respect to z and using Equation (3.9) to eliminate $\mathcal{E}$. The resulting expression is multiplied through by $\mathcal{Q}^*$, resulting in

$$i\mathcal{Q}^*\mathcal{Q}_{tz} + \delta\mathcal{Q}^*\mathcal{Q}_z + \mathcal{Q}^*\left(|\mathcal{Q}|^2\mathcal{Q}\right)_z = -i|\mathcal{Q}|^2. \tag{3.15}$$

Now multiply Equation (3.10) by $\mathcal{Q}_z^*$ and use Equation (3.9) to obtain

$$i\mathcal{Q}_t\mathcal{Q}_z^* + \delta\mathcal{Q}\mathcal{Q}_z^* + |\mathcal{Q}|^2\mathcal{Q}\mathcal{Q}_z^* = -i\mathcal{E}\mathcal{E}_{zz}^*. \tag{3.16}$$

Subtracting Equation (3.16) and its complex conjugate from Equation (3.15) and its

complex conjugate yields

$$\mathcal{Q}^* \left(|\mathcal{Q}|^2 \mathcal{Q}\right)_z + \mathcal{Q} \left(|\mathcal{Q}|^2 \mathcal{Q}^*\right)_z - |\mathcal{Q}|^2 \mathcal{Q}\mathcal{Q}_z^* - |\mathcal{Q}|^2 \mathcal{Q}^* \mathcal{Q}_z$$
$$+i \left(\mathcal{Q}_t^* \mathcal{Q}_z + \mathcal{Q}^* \mathcal{Q}_{tz} - \mathcal{Q}_t \mathcal{Q}_z^* - \mathcal{Q}^* \mathcal{Q}_{tz}\right) = i \left(\mathcal{E}\mathcal{E}_{zz}^* - \mathcal{E}^* \mathcal{E}_{zz}\right).$$

A number of simplifications may be made. The first line of this expression is equal to $|\mathcal{Q}|_z^4$, the next term is $(\mathcal{Q}^* \mathcal{Q}_z - \mathcal{Q}\mathcal{Q}_z^*)_t$, and the right hand side is $-i \left(\mathcal{E}^* \mathcal{E}_z - \mathcal{E}\mathcal{E}_z^*\right)_z$. This results in [78]:

$$\frac{\partial}{\partial z} \left(|\mathcal{Q}|^4 + \mathcal{E}^* \mathcal{Q} + \mathcal{E}\mathcal{Q}^*\right) + i \frac{\partial}{\partial t} \left(\mathcal{Q}^* \frac{\partial \mathcal{Q}}{\partial z} - \mathcal{Q} \frac{\partial \mathcal{Q}^*}{\partial z}\right) = 0. \tag{3.17}$$

Equations (3.11), (3.14), and (3.17) may be integrated in time. Considering localized pulse solutions, the fields vanish at $t = \pm\infty$ so boundary terms in the integrals are zero. This calculation results in the conserved quantities

$$c_1 = \int_{\mathbf{R}} |\mathcal{E}|^2 \mathrm{d}t, \quad c_2 = \mathrm{Im} \int_{\mathbf{R}} \mathcal{E}^* \mathcal{Q} \mathrm{d}t, \quad c_3 = \int_{\mathbf{R}} \left[|\mathcal{Q}|^4 + 2\mathrm{Re} \left(\mathcal{E}^* \mathcal{Q}\right)\right] \mathrm{d}t.$$

3.5 Solitary wave solutions and self-induced transparency

It is well known from the classical theory of light interaction with a resonant "active" medium that the material acts as an attenuator. This is described by the classical Lorentz model. Due to the absorbing nature of the material, this model does not

support solitary wave solutions. However, through an exchange of energy between an intense optical pulse and a resonant medium, solitary wave solutions do exist. Many nonlinear systems occurring in nature admit solitary wave solutions. The previous chapter discusses solitary wave solutions of the NLS equation in detail. The MD equations have a form which is similar to NLS, and the physics of energy exchange between the pulse and the medium is similar to pulse propagation in active media. Therefore it is reasonable to search for solitary wave solutions of the MD equations.

3.5.1 Derivation

In this section a family of solitary wave solutions to the MD system, Equations (3.9) and (3.10), is derived. To begin the derivation, a scaling analysis suggests the use of the following ansatz:

$$\mathcal{E}(t,z) = v^{3/4}\exp(i\varphi + i\Omega t)\mathcal{E}_s(\xi) \quad \mathcal{Q}(t,z) = v^{1/4}\exp(i\varphi + i\Omega t)\mathcal{Q}_s(\xi)$$

where the traveling wave reduction

$$\xi = \frac{z - v(t - t_0)}{\sqrt{v}}$$

is used. The real constants φ, Ω, v, and t_0 represent phase, frequency, velocity, and position, respectively, of the solitary wave. The velocity v represents the amount

by which the pulse propagates *slower* than the speed of light in the medium and the frequency Ω takes any change in the carrier frequency of the optical pulse into account. Inserting this into the MD system obtains ordinary differential equations for the form of the solitary wave

$$\begin{aligned} i\mathcal{E}_s' &= \mathcal{Q}_s \\ -i\mathcal{Q}_s' + 2\Delta\mathcal{Q}_s + |\mathcal{Q}_s|^2\mathcal{Q}_s &= \mathcal{E}_s, \end{aligned} \tag{3.18}$$

where

$$\Delta = \frac{\delta - \Omega}{2\sqrt{v}}.$$

In the traveling wave reference frame, the expression for energy conservation, Equation (3.11) becomes

$$\left(|\mathcal{E}_s|^2 - |\mathcal{Q}_s|^2\right)' = 0.$$

Since only solitary wave solutions, for which the fields vanish as $\xi \to \pm\infty$, are being considered, integrating this expression results in

$$|\mathcal{E}_s|^2 = |\mathcal{Q}_s|^2,$$

where the integration constant is necessarily zero. This implies that the amplitudes of $\mathcal{E}_s$ and $\mathcal{Q}_s$ are identical. Thus the forms

$$\mathcal{E}_s = u\exp(i\theta), \qquad \mathcal{Q}_s = u\exp(i\theta + i\psi),$$

in which u, θ, and ψ are real functions of ξ, are applied to Equation (3.18) to obtain the system

$$u' = u\sin\psi \tag{3.19}$$

$$\theta' = -\cos\psi \tag{3.20}$$

$$\psi' = 2\cos\psi - 2\Delta - u^2. \tag{3.21}$$

Dividing Equation (3.21) by Equation (3.19) and using $\sin\psi \mathrm{d}\psi/\mathrm{d}u = -\mathrm{d}\cos\psi/\mathrm{d}u$ results in a linear equation for $\cos\psi$, the solution of which is

$$\cos\psi = \Delta + u^2/4.$$

The integration constant is zero since $u = 0$ as $\xi \to \pm\infty$ but $\cos\psi$ is bounded. It is now possible to solve Equation (3.19). Multiplying through by $2u$ and using $2uu' = (u^2)'$ gives

$$(u^2)' = 2u^2\sqrt{1 - (\Delta + u^2/4)^2}.$$

This equation may be integrated to obtain

$$u(\xi) = \eta \left[\cosh(\eta\xi) + \Delta\right]^{-1/2},$$

where $\eta = 2\sqrt{1-\Delta^2}$. This result is used to integrate Equations (3.20) and (3.21), yielding

$$\theta(\xi) = -\Delta\xi - \arctan\left[\mu \tanh\left(\eta\xi/2\right)\right]$$

$$\psi(\xi) = -2\arctan\left[\mu \tanh\left(\eta\xi/2\right)\right],$$

with $\mu = \sqrt{(1-\Delta)/(1+\Delta)}$. Finally the solitary wave solutions to the MD equations are

$$\begin{aligned} \mathcal{E}_s(t,z) &= \frac{\eta v^{3/4} \exp[i\varphi + i\Omega t - i\Delta\xi - i\chi(\xi)]}{\sqrt{\cosh(\eta\xi) + \Delta}} \\ \mathcal{Q}_s(t,z) &= v^{-1/2}\mathcal{E}_s(t,z)\exp[-2i\chi(\xi)], \end{aligned} \tag{3.22}$$

where $\chi(\xi) = \arctan\left[\mu \tanh\left(\eta\xi/2\right)\right]$. Plots of the electric field as a function of the moving frame time coordinate t appear in Figure 3.6. It is clear that pulses become more sharply peaked and localized with increased velocity v. Positive frequency Ω (or negative detuning δ) results in higher amplitude and induces a positive slope on the argument of $\mathcal{E}$.

The reality of η implies that $1 - \Delta^2 > 0$, which results in the condition for exis-

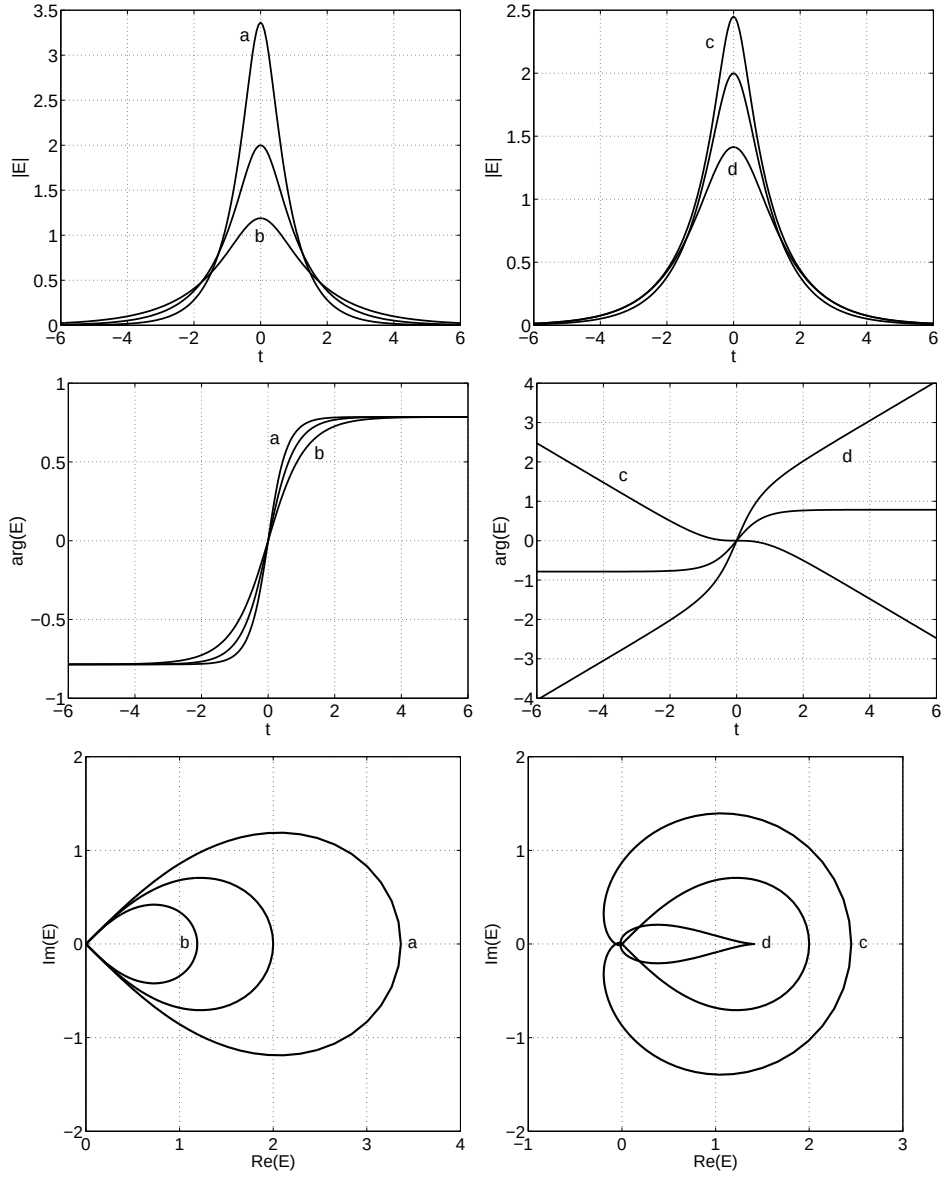

FIGURE 3.6. Solitary wave solutions of the Maxwell-Duffing equations (3.9) and (3.10). The electric field envelope is plotted at $z = 0$. The left column shows variation in velocity: $v = 2$ is labeled (a) and $v = 1/2$ is labeled (b). The unlabeled curve is $v = 1$. The other parameters in the left column plots are $\varphi = 0$, $\delta = 0$, $\Omega = 0$, and $t_0 = 0$. The right column shows variation in frequency: $\Omega = -1/2$ is labeled (c) and $\Omega = 1/2$ is labeled (d). The unlabeled curve is $\Omega = 0$. The other parameters in the right column plots are $v = 1$, $\varphi = 0$, $\delta = 0$, and $t_0 = 0$.

tence of these solutions

$$|\delta - \Omega| < 2\sqrt{v}. \tag{3.23}$$

The parameters v, Ω, φ, and t_0 provide relatively simple mathematical expressions for the solitary waves. In practice, however, it is easier to control and measure peak amplitude $A = 2v^{3/4}\sqrt{1-\Delta}$ than pulse velocity, therefore the parameters A, Ω, φ, and t_0 form a more suitable set for the practitioner. Given the pulse amplitude A, the corresponding velocity parameter depends on the value of the quantity $\delta - \Omega$. If $\delta = \Omega$, then $v = (A/2)^{4/3}$ trivially. For the case when $\delta \neq \Omega$, write the amplitude as

$$A = 2v^{3/4}(1 - \sigma|\delta - \Omega|/2\sqrt{v})^{1/2},$$

where the parameter $\sigma = \mathrm{sgn}(\delta - \Omega)$. Then defining $\bar{v} = (2\sqrt{v}/|\delta - \Omega| - \sigma)^{1/2}$ and $\bar{A} = \sqrt{27/2}|\delta - \Omega|^{-3/2}A$ leads to an expression for the modified velocity

$$\bar{v} = (y^{-1/3} - \sigma y^{1/3})/\sqrt{3}, \quad y = \sigma[(\bar{A}^2 + \sigma)^{1/2} - \bar{A}]^{1/2}.$$

In this calculation, the appropriate branches have been chosen so that the expressions are consistent with reality and positivity conditions on the parameters.

3.5.2 Interpretation of solitary wave solutions

These solitary wave solutions may be viewed as analogs to the phenomenon of self-induced transparency of Maxwell-Bloch (MB) optical pulses in two-level media [73]. An optical pulse of arbitrary shape whose carrier wave is in resonance with the atomic transition frequency of the two-level medium induces its own transparency if it contains a sufficient amount of a dimesionless quantity known as "optical area," which is defined as

$$A(t,z) = \frac{e^2}{m\omega_0 d}\int_{-\infty}^{t} E(t',z)\mathrm{d}t'.$$

Here d is the dipole moment of the active atoms, ω_0 is the optical carrier frequency, and e and m are the electron charge and rest mass. An incident pulse induces transparency and evolves into a solitary wave (or solitary waves) when it's "optical area" is greater than π. Pulses which are not sufficiently intense are simply absorbed by the medium, as described by the classical linear Lorentz theory. These dynamics are predicted by the optical area theorem [73], which describes the evolution of optical area as a function of propagation distance. The mathematical statement of the area theorem is

$$\frac{\partial A}{\partial z} = -\sin A,$$

where $A = A(\bar{t}, z)$ is evaluated at some time $\bar{t}$ which occurs after the pulse has passed the observation point z. This equation has stable fixed points at $2n\pi$ and unstable fixed points at $(2n+1)\pi$, where n is an integer. Given an input pulse with arbitrary optical area, its area evolves to its nearest 2π-multiple as the pules propagates through the absorber.

In the case of the MD equations, the linear regime is similarly described by Lorentz theory. However, an analog to the area theorem has not been discovered. While there is no analytic theory which predicts pulse evolution, this problem can be studied numerically. Numerical simulations of the evolution of three Gaussian input pulses with successively increasing amplitudes are shown in Figure 3.7 for both the electric and material excitation fields. In the case of an input pulse of amplitude 1/2, shown in the top surfaces, the system cannot adapt to form a solitary wave and the pulse is converted into continuous radiation, characterized by small-amplitude oscillations in the fields. The plotting routine used emphasizes the contrast between different surface angles, which accentuates these oscilations. However, they are small in amplitude. The energy from the pulse is dispersed and exchanged between the electric and material excitation fields. The middle row of surfaces shows the evolution of an input pulse of amplitude 2. In this case, a solitary wave is produced along with excessive radiation. The bottom row of surfaces indicates the evolution of an input pulse with amplitude 5. Here the initial pulse immediately splits into two solitary waves of different amplitudes, and again emits excessive radiation.

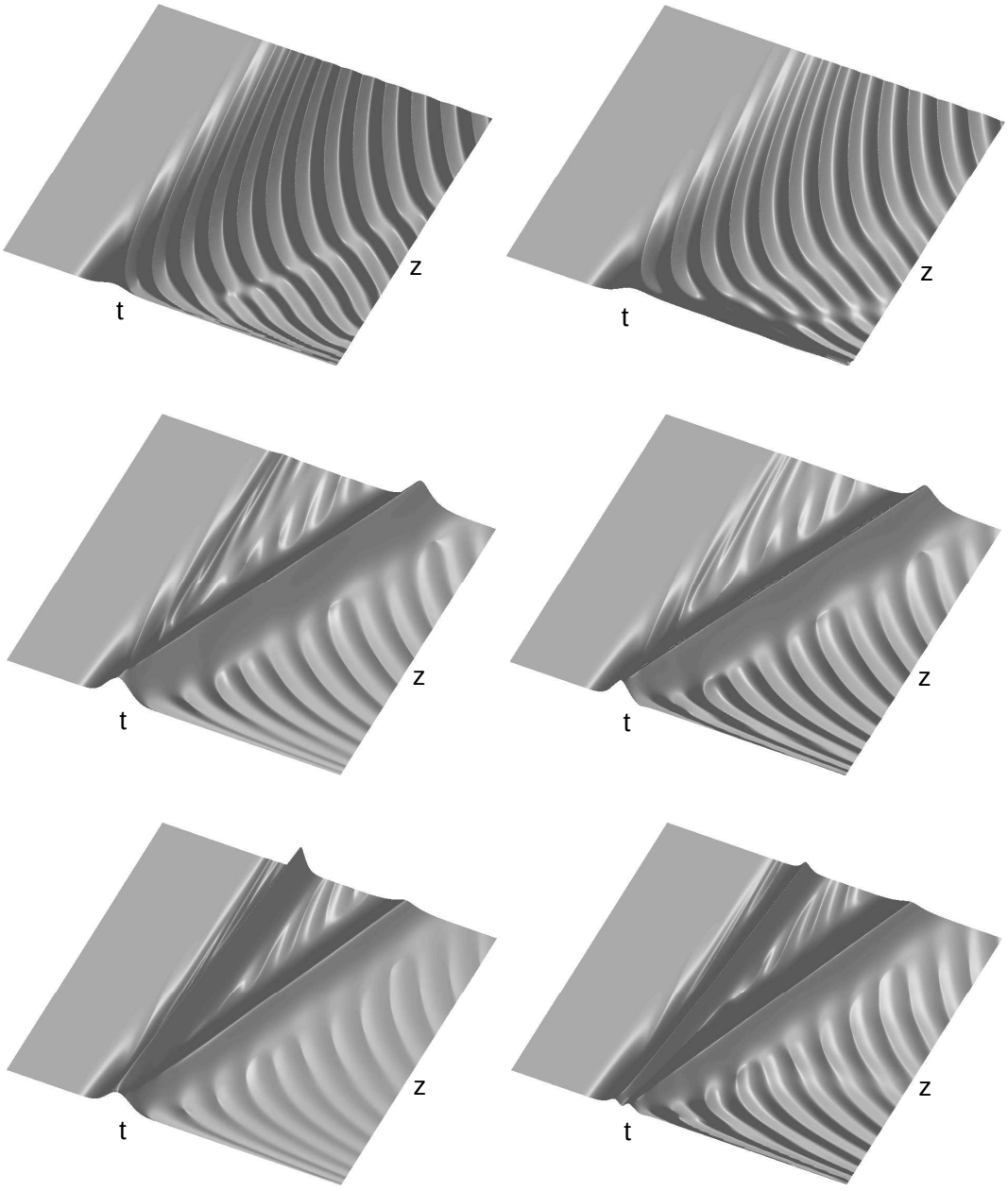

FIGURE 3.7. Evolution of electric (left) and material excitation (right) field amplitudes in response to Gaussian input pulses of amplitude 1/2 (top), 2 (middle), and 5 (bottom). For sufficiently large amplitude input pulses, one or more solitary waves evolve from the initial pulse, emitting radiation in the process.

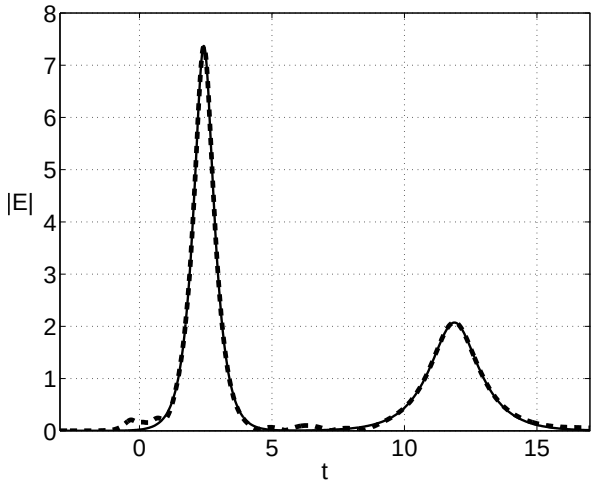

FIGURE 3.8. Comparison between numerical simulation of solitary wave formation (dashed line) and analytic solutions (solid line) using parameters obtained from the numerics. These two solitary waves formed from a Gaussian input pulse $5\exp(-t^2/2)$. Aside from low-amplitdue radiation, the agreement is excellent, indicating self selection of the solitary wave solutions.

The amplitudes and widths (at half maximum) of the pulses in these simulations may be measured and used to calculate their velocities and frequencies. In the last simulation, the two pulses which evolve from the large Gaussian input pulse are determined to have $v_1 = 8.02$, $\Omega_1 = -2.28$, $t_1 = 2.43$, and $v_2 = 1.76$, $\Omega_2 = -1.43$, $t_2 = 11.89$. Figure 3.8 shows a comparison between the analytic form of the solitary waves with these parameters and the results of the numerical simulation. Ignoring the emitted radiation, the agreement is excellent. This shows that indeed the system self-selects the solitary wave solutions from arbitrarily-shaped input pulses.

The evolution of solitary waves from Gaussian input pulses is characterized in Figure 3.9. This diagram shows the amplitude and multiplicity of the solitary waves

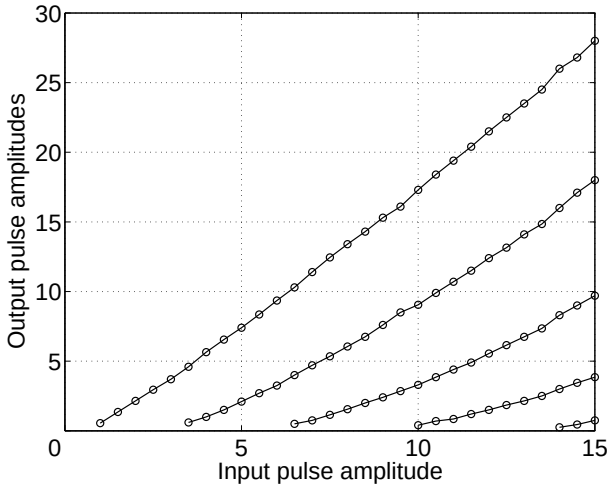

FIGURE 3.9. Amplitude of solitary waves evolving from Gaussian input pulses of the form $A\exp(-t^2/2)$ as a function of incident pulse amplitude A. In response to increasing input pulse amplitudes, solitary wave amplitudes increase until a bifurcation occurs resulting in the production of an additional solitary wave. The bifurcations take place at $A \sim$1, 3.5, 6.5, 10, and 14.

produced as a function of the initial Gaussian pulse amplitude. As input pulse amplitude increases, so too does the amplitude of the solitary wave which evolves from it. This trend continues until a certain threshold is acheived and a second solitary wave is produced. Then the amplitudes of these waves increase until a third wave is produced. In this way, an arbitrary number of solitary waves may be produced from a sufficiently intense input pulse. The first five bifurcation points in the input pulse amplitude at which a new solitary wave is created are approximately 1, 3.5, 6.5, 10, and 14.

Despite the similar self-induced transparency behavior of MB and MD solitary waves, the two systems admit solitary wave solutions which differ in two ways: MB

	Maxwell-Bloch	Maxwell-Duffing
phase	linear	nonlinear
SIT	determined by area theorem	no analytic description
collision dynamics	elastic	parameter dependent

TABLE 3.1. Contrasting characteristics of Maxwell-Bloch and Maxwell-Duffing solitary waves and their dynamics.

pulses are characterized by linear phase, whereas MD pulses have nonlinear phase; and MB pulses interact elastically with one another, whereas the degree of elasticity of MD pulses is parameter dependent. This feature will be discussed further in a later section on collision dynamics. The contrasting features of MB and MD solitary waves are presented in Table 3.1

Stability analysis is critical to the mathematical description of solitary waves since stability determines whether or not the pulses may be realized experimentally. A stability analysis of the MD solitary waves is conducted in the following section.

3.5.3 Stability analysis and localized modes

A unique feature of the MD solitary waves is the difference of the asymptotic values of the phase when detuning and frequency parameters are zero. This difference is defined as $\Delta\phi = \phi(\infty) - \phi(-\infty) = \pi/2$, where $\phi = \arg(E)$ (see the second row of plots in Figure 3.6). Given this unusual feature, it is natural to examinate the pulse dynamics under a deformation of the argument which affects $\Delta\phi$. This kind of deformation is

an illustration of a general perturbation of the solitary wave, which may be seen by writing the wave in amplitude-phase form $\mathcal{E} = A\exp(i\Phi)$ and introducting an ε perturbation:

$$\begin{aligned}
\mathcal{E} &= A\exp[i(1+\varepsilon)\Phi] \\
&= A\exp(i\Phi)\exp(i\varepsilon\Phi) \\
&= A\exp(i\Phi)(1+i\varepsilon\Phi+\cdots) \\
&\simeq \mathcal{E}_s + i\varepsilon\Phi\mathcal{E}_s,
\end{aligned}$$

where $\mathcal{E}_s$ is a solitary wave solution. Writing the form of the electric field in this way illustrates that a (perhaps strong) perturbation to the phase of the pulse is effectively a more general additive perturbation, where the perturbation may influence the pulse dynamics differently depending on the sign and amplitude of ε.

Figure 3.10 shows the results of numerical simulations of the pulse dynamics in cases where the phase difference is compressed to $\Delta\phi = \pi/4$ (left surface), corresponding to the $\varepsilon < 0$ case; and expanded to $\Delta\phi = 3\pi/4$ (right surface), corresponding to the $\varepsilon > 0$ case. When the phase difference is compressed, the pulse emits radiation but evolves into a solitary wave solution and persists. This indicates that the pulse parameters are shifted while the pulse evolves, and they approach values for which the existence condition (3.23) is satisfied. However, when the phase difference is expanded, the pulse parameters are unable to adapt to a state where they satisfy

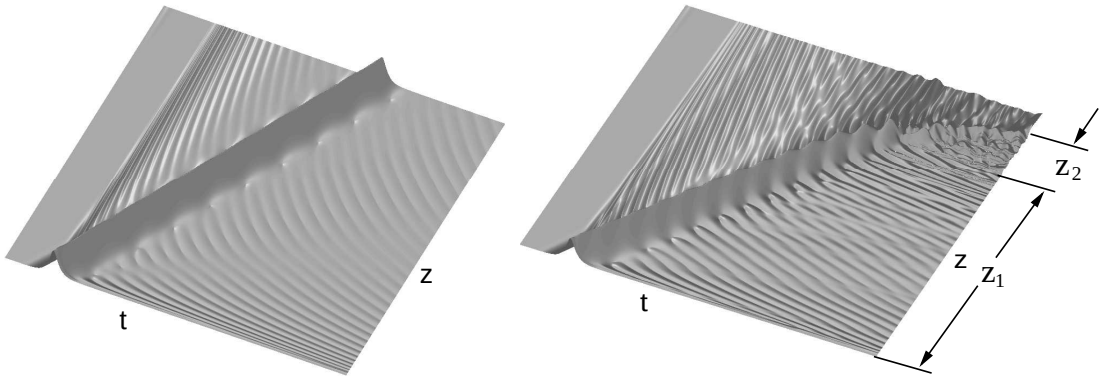

FIGURE 3.10. Evolution of the electric field envelope under phase perturbations $\Delta\phi = \pi/4$ (left) and $\Delta\phi = 3\pi/4$ (right). In both cases the pulse emits radiation, but the phase-compressed pulse evolves into a stable solitary wave, while the phase-expanded pulse is unstable and disintigrates. The right surface shows the two characteristic instability scales of confinement z_1 and breakup z_2. The unperturbed solitary wave used in these simulations is parameterized by $v = 1$, $\Omega = 0$, $t_0 = 0$, $\varphi = 0$, and $\delta = 0$, and the simulation domain is $t \in [-10, 50]$, $z \in [0, 30]$.

the existence condition and the pulse is destroyed. This illustrates the dependence of solitary wave stability on the sign of the perturbation $\pm\varepsilon$. From the figure, it is clear that there are two distinct scales involved with the pulse destruction. The long scale (indicated by z_1) is characterized by the existence of two structures: both the pulse and the radiation. The short scale (indicated by z_2) characterizes the complete disintegration of the pulse into radiation. These distinct scales suggest the dynamics of the pulse before its destruction are described by first-order perturbation effects. The modes describing the perturbation grow (hence the increasing amplitude of oscillation) until second-order effects become large. These second-order effects characterize finite-distance blowup in the amplitude of these modes. Through nonlinear interac-

tion, the energy in the local modes is transfered to the radiation modes, resulting in complete loss of energy confinement and destruction of the pulse.

It is convenient to observe the evolution of the phase-perturbed pulses in the complex plane, with the curve parameterized by t (see the bottom row of plots in Figure 3.6). In this way a solitary wave appears as a homoclinic orbit, with the vertex of the orbit is located at the origin of the complex plane, as required by the asymptotic decay of the pulses as $t \to \pm\infty$. At $z = 0$, the lower branch of the orbit represents the shoulder of the pulse for negative values of t, while the upper branch indicates positive values of t. The angle the branches form at the vertex of the orbit indicates the asymptotic phase difference $\Delta\phi$ (when $\Omega = \delta = 0$). The evolution of the phase-compressed pulse (corresponding to the left surface of Figure 3.10) appears in Figure 3.11. The procession of the orbit about the origin indicates the frequency shift incurred by the pulse under the perturbation. The shape of the orbit changes as the pulse propagates, but its loop topology is preserved which indicates that energy confinement persists. These dynamics provide more evidence that localized modes which characterize the perturbation are excited.

Figure 3.12 illustrates the evolution and breakup of the phase-expanded pulse, corresponding to the right surface in Figure 3.10. Again, the pulse picks up a shift in frequency, although it processes about the origin in the opposite direction due to the opposite sign of ε. The oscillations of the orbit shape become increasingly prevalent, indicating that the amplitude of the localized modes continues to grow until the loop

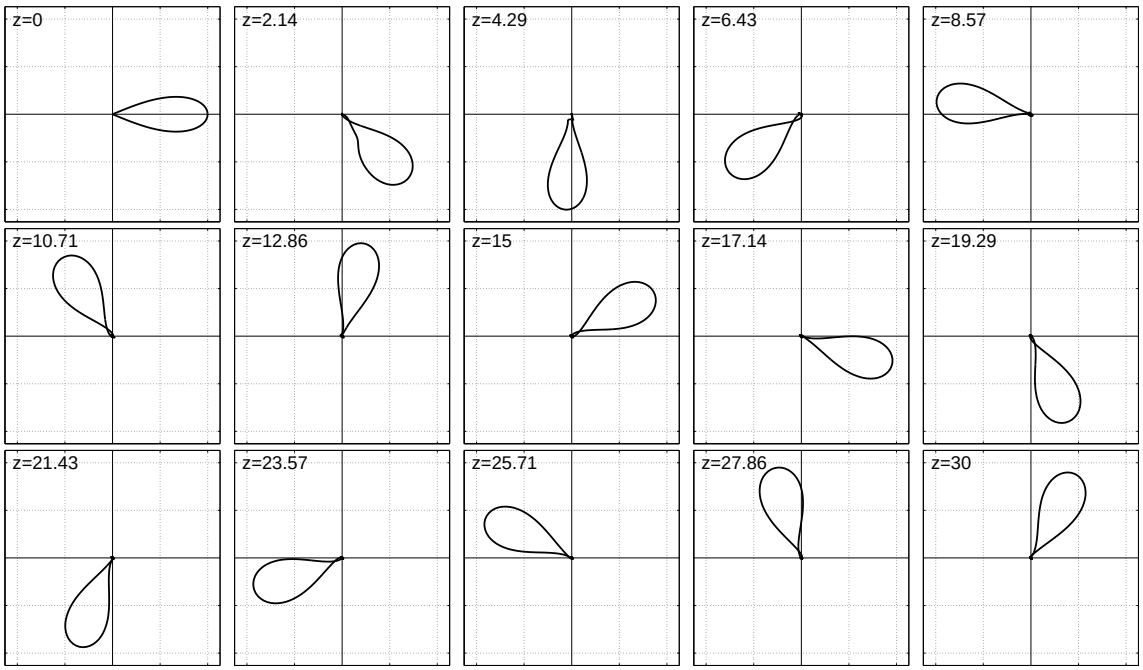

FIGURE 3.11. The z-evolution of the electric field in the phase-compressed ($\Delta\phi < \pi/2$) case plotted in the complex plane. The horizonal axes are real and the vertical axes are imaginary. The clockwise procession about the origin is due to a frequency shift caused by the perturbation. The subtle change in shape of the orbit indicates that localized modes which characterize perturbations about the solitary wave solution are excited.

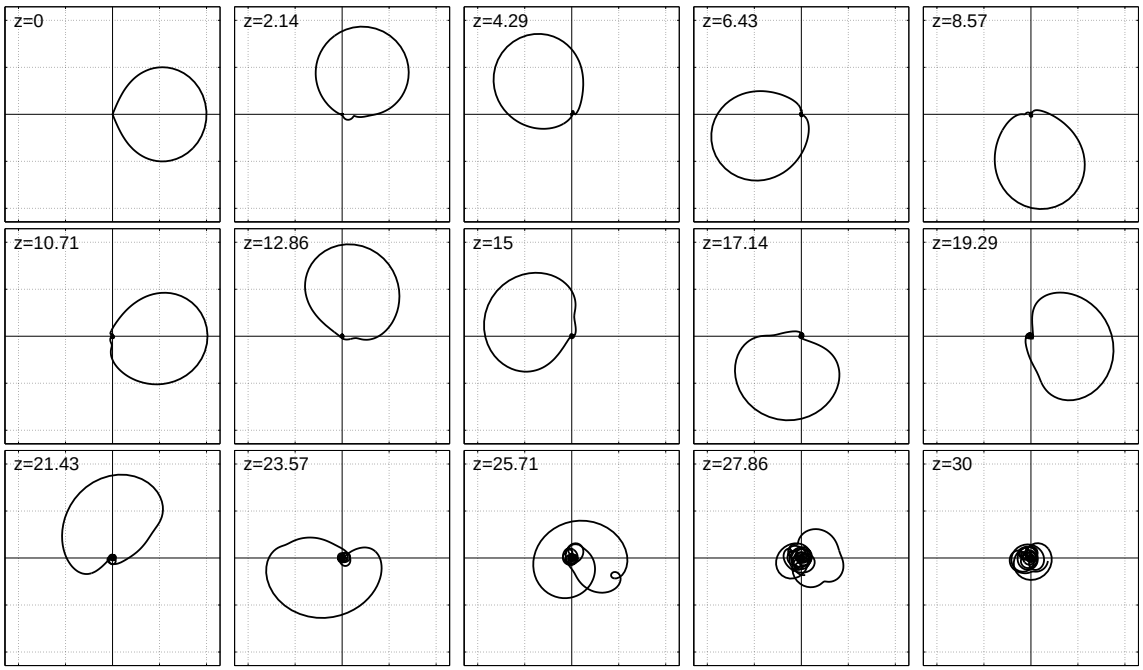

FIGURE 3.12. The z-evolution of the electric field in the phase-expanded ($\Delta\phi > \pi/2$) case plotted in the complex plane. The horizonal axes are real and the vertical axes are imaginary. The counterclockwise procession about the origin is due to frequency shift caused by the phase expansion. The amplitude of the excited localized modes grows until their energy is transfered to radiation modes, resulting in pulse destruction.

topology collapses into continuous radiation.

Numerical simulations show that the dynamics of perturbed MD solitary waves have two characteristics: pulse oscillations and emission of radiation. There are two possible explanations of these phenomena. In the first case, the pulse does not have any internal structure (localized modes). In the absence of the internal structure, any excessive energy is simply released from the pulse in the form of radiation. As it radiates, the pulse slowly approaches a stationary solution in a manner characterized by algebraically-decaying oscillations [79]. In the second case, the pulse possesses the

internal structure of localized modes. Exact solitary waves 3.22 propagate without exciting these modes, but perturbations to the wave cause the modes to become excited. In this case the propagation dynamics are complicated by the dynamical contribution of the excited localized modes. The next task is to determine into which catagory the MD solitary waves fall.

In order to determine the structure of MD perturbations, it is necessary to characterize the spectrum of the linear operator describing perturbations about the solitary wave solutions. The stability of solutions of nonlinear PDEs are commonly studied by introducing an additive perturbation into the solution and linearizing in the order of the perturbation. This results in a nonconstant coefficient linear operator which describes the dynamics of the perturbation about the PDE solution. The location of the spectrum of this operator in the complex plane determines the stability of the solution. It reveals whether the perturbation grows, decays, or is constant. In the MD case, the following ansatz is inserted into Equations (3.9) and (3.10):

$$\mathcal{E}(t,z) = \mathcal{E}_s(t,z) + v^{3/4}\exp(i\varphi + i\Omega t)\epsilon(\xi,\tau)$$

$$\mathcal{Q}(t,z) = \mathcal{Q}_s(t,z) + v^{1/4}\exp(i\varphi + i\Omega t)q(\xi,\tau).$$

Here $\mathcal{E}_s(t,z)$ and $\mathcal{Q}_s(t,z)$ are the solitary wave solutions derived in the preceeding

subsection and

$$\xi = \frac{z - v(t - t_0)}{\sqrt{v}}, \quad \tau = \sqrt{v}t.$$

The perturbations ϵ and q are of subleading order and τ is considered the evolution variable. Collecting the terms in $\mathcal{O}(\epsilon, q)$ obtains the linear PDE

$$i\partial_\tau q = i(\partial_\xi - \partial_\xi^{-1})q - 2\Delta q - 2|\mathcal{Q}_s|^2 q - \mathcal{Q}_s^2 q^*, \tag{3.24}$$

where

$$\Delta = \frac{\delta - \Omega}{2\sqrt{v}}.$$

When combined with its negative complex conjugate, Equation (3.24) can be written as

$$i\partial_\tau \mathbf{q} = \hat{L}\mathbf{q} \tag{3.25}$$

with the spinor $\mathbf{q} = (q, q^*)^T$ and the operator

$$\hat{L} = \left[i\hat{I}(\partial_\xi - \partial_\xi^{-1}) - 2\hat{\sigma}_3(\Delta + |\mathcal{Q}_s|^2) + \begin{pmatrix} 0 & -\mathcal{Q}_s^2 \\ \mathcal{Q}_s^{*2} & 0 \end{pmatrix} \right]. \tag{3.26}$$

(3.27)

In this expression, $\hat{I}$ is the 2×2 identity matrix, the third Pauli matrix is

$$\hat{\sigma}_3 = \begin{pmatrix} 1 & 0 \\ 0 & -1 \end{pmatrix},$$

and the reciprocal derivative operator is defined as

$$\partial_\xi^{-1}(\cdots) = \int_{-\infty}^{\xi} (\cdots) \mathrm{d}\xi'.$$

As previously discussed, the breathing dynamics of the phase-perturbed solitary waves could have two explanations. Either the pulse approaches the true solitary wave form via algebraically-decaying oscillations or localized modes are excited by the perturbation. To understand which is the case, it is reasonable to investigate the existence of localized modes by examining the spectrum of $\hat{L}$, the operator which describes perturbations about the solitary wave solution. The spectrum of an operator may be divided into discrete and continuous subsets. The former corresponds to modes which are local to the solitary wave while the latter corresponds to radiation modes which propagate as plane waves away from the pulse. The regions of the complex plane which contain continuous spectrum may be identified by analyzing the dispersion relation for plane waves far from the solitary wave. To this end, let $\xi \to \infty$, in which case the potential terms $|\mathcal{Q}_s|^2$, $\mathcal{Q}_s^2$, and $\mathcal{Q}_s^{*2}$ vanish. Inserting a plane wave

ansatz $q = \exp(ik\xi - i\omega\tau)$ into Equation (3.24) in this limit results in

$$-\omega = k + 1/k + 2\Delta.$$

Solving for k gives the dispersion relation

$$k(\omega) = -\frac{\omega + 2\Delta}{2} \pm \sqrt{\frac{(\omega + 2\Delta)^2}{4} - 1}.$$

Radiation modes do not grow or decay, so they are characterized by real-valued wavenumbers. The dispersion relation shows that $k \in \mathbf{R}$ when

$$|\omega + 2\Delta| > 2. \tag{3.28}$$

Thus there exists a prohibited gap in the continuous spectrum, which implies that only plane waves with frequencies outside the gap propagate. If localized modes exist, then their corresponding eigenvalues lie within the gap.

In the representation of Equation (3.25), solitary wave solutions are stable if the imaginary part of the spectrum of $\hat{L}$ is negative. If the spectrum lies on the real axis, the solitary waves are neutrally stable. Therefore the location of the spectrum in the complex plane describes the stability of the solitary waves and thus needs to be determined.

While spectral theory is well-developed in the case of self-adjoint operators, not

much theory exists for non-self-adjoint operators such as $\hat{L}$. However, the spectrum can be investigated using numerical methods. To this end, the operator $\hat{L}$ is discretized and the problem

$$\hat{L}\mathbf{q} = \mu\mathbf{q}$$

is solved for the eigenvalues μ and eigenvectors $\mathbf{q}$. The discrete approximation of $\hat{L}$ is a matrix whose spectrum is purely discrete. Thus the eigenvalues of the discrete $\hat{L}$ are only representative approximations of the true spectrum of the continuous operator. Using Matlab's `eig` function, the numerical analysis of the spectrum is presented in Figure 3.13 for the case where the solitary wave $\mathcal{Q}_s$ has parameters $v = 1$, $\Omega = 0$, $\varphi = 0$, and $t_0 = 0$, the detuning is $\delta = 0$. Also shown on the plots in this figure is a circle indicating the boundary between discrete and continuous spectrum, as determined by Equation (3.28). The top left plot shows the entire spectrum on the complex plane. The eigenvalues which are aligned with the real axis and are located outside the gap represent the discrete approximation of the continuous spectrum. Many eigenvalues have positive imaginary parts, which would indicate an instability. This is an indication that some error is introduced by the eigenvalue solver, since solitary waves are observed to be stable in numerical simulations which intrinsically introduce perturbations due to limitations in accuracy and roundoff error.

A gap in the representation of the continuous spectrum is observed as predicted by

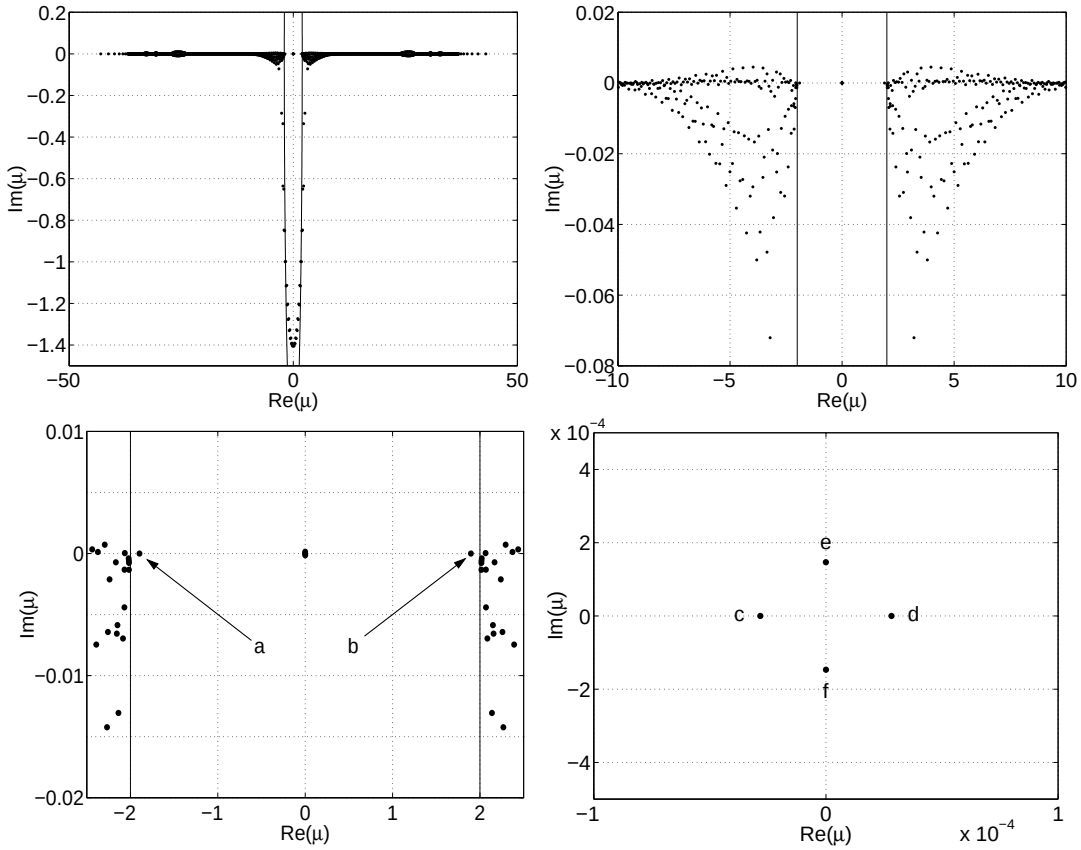

FIGURE 3.13. Numerical analysis of the spectrum of the discretized operator $\hat{L}$ in the case where the solitary wave $\mathcal{Q}_s$ has parameters $v = 1$, $\Omega = 0$, $\varphi = 0$, and $t_0 = 0$, the detuning is $\delta = 0$. The highly elongated circle (due to axes scales) indicates the prohibitive gap in the continuous spectrum. Each plot gives a closer view of the origin of the complex plane. Six localized modes are contained within the gap and thier corresponding eigenvalues are labeled a, b, c, d, e, and f. Eigenvalues μ_{c}-μ_{f} converge to zero as the discretization of the $\hat{L}$ is refined, indicating that their corresponding eigenfunctions are in the nullspace of $\hat{L}$. The eigenvalues $\mu_{\mathrm{a,b}} = \pm 1.897$ using $\Delta\xi = 0.0\bar{3}$ with a tenth order accurate discretization.

Equation (3.28). The eigenvalues within the gap which have imaginary part near -1.2 have unlocalized corresponding eigenvectors, which suggests that they are numerical artifacts introduced by the eigenvalue solver and have no physical meaning. The top right plot shows a closeup of the structure of the spectrum near the gap. The lower left plot shows an even closer view of the gap, where eigenvalues are identified both near the origin and near the boundary of the gap (labeled a and b). An even closer view of the origin of the complex plane is shown in the lower right plot, revealing four distinct eigenvalues, labeled c, d, e, and f. These eigenvalues are observed to converge to zero as the discretization of $\hat{L}$ is refined, suggesting that they correspond to zero eigenmodes which live in the nullspace of $\hat{L}$. This convergence behavior indicates that the discrete spectrum has zero imaginary part. Thus the corresponding modes are neutrally stable, which agrees with the numerical observation of oscillations occuring in perturbed pulses. These modes are excited by the perturbation and do not grow or decay; they simply propagate along with the pulse at its group velocity.

The modes corresponding to these six eigenvalues within the gap are shown in Figure 3.14. The modes corresponding to eigenvalues a and b are localized but are characterized by broad tails. The modes corresponding to eigenvalues c and d have identical profiles and are more localized than those which correspond to eigenvalues near the boundary of the gap. Similarly, the modes corresponding to eigenvalues e and f are degenerate and localized. The decay of the amplitude of the modes as $t \to \pm\infty$ is shown in Figure 3.15, where they are plotted on a log scale along with the

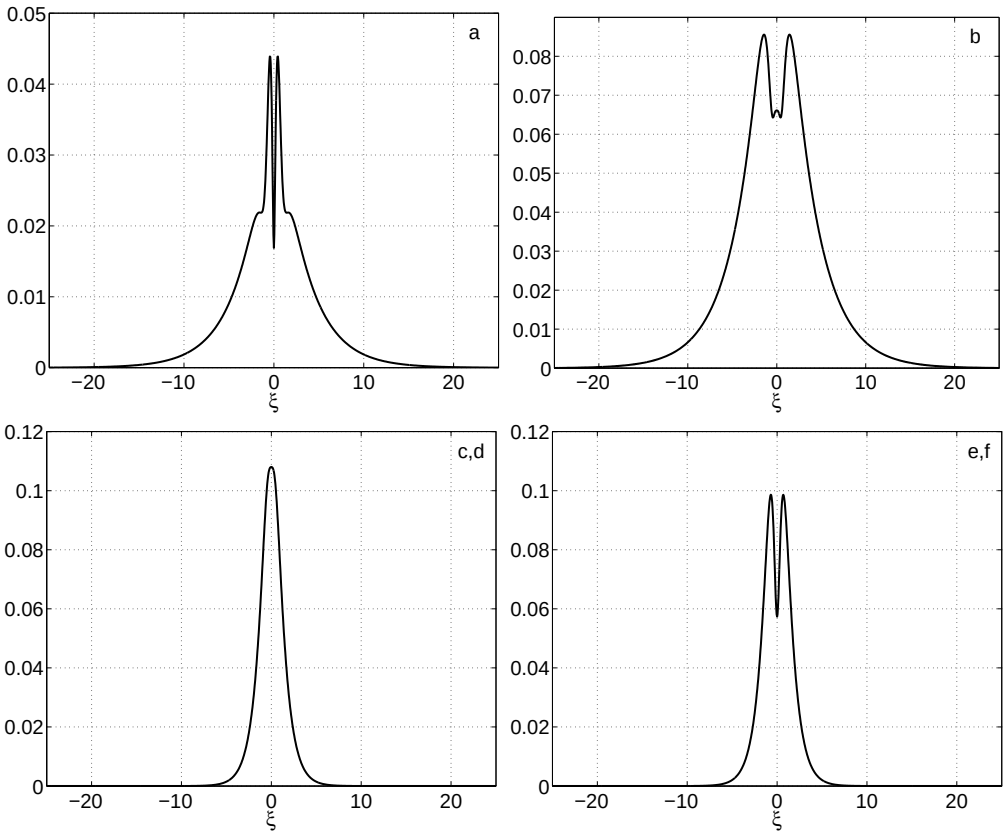

FIGURE 3.14. Localized eigenfunctions corresponding to the discrete spectrum of $\hat{L}$. The eigenfunctions labeled a, b, c, d, e, and f correspond to the labeled eigenvalues in Figure 3.13

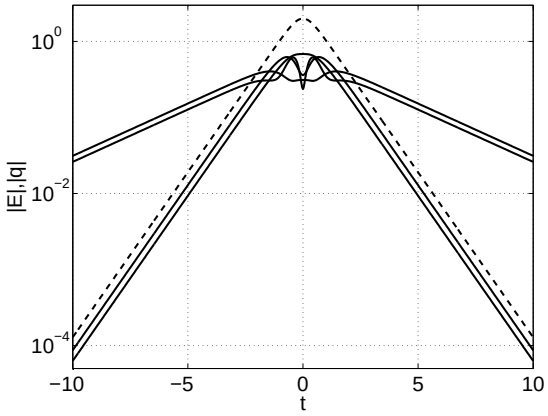

FIGURE 3.15. Amplitude of localized modes (solid) and solitary wave solution with $v = 1$, $\Omega = 0$ plotted on a log scale. Modes a and b decay more slowly than the others.

solitary wave solution with $v = 1$, $\Omega = 0$. This figure reveals that the broad modes (a and b) decay at a slower rate than the narrow modes (c-f), which in turn decay at the same rate as the solitary wave solution.

Numerical simulations may be used to observe the effects these localized modes have on the solitary wave solutions. The initial condition in the electric field is given by

$$\mathcal{E}(t,0) = \mathcal{E}_s(t,0) + 0.05\epsilon(-\sqrt{v}t, 0),$$

where ϵ is obtained by integrating Equation (3.9)

$$\epsilon(\xi,\tau) = -i\int_{-\infty}^{\xi} q(\xi',\tau)\mathrm{d}\xi'$$

and q corrsponds to the modes in Figure 3.14.

The results of these numerical simulations are presented in Figure 3.16, where a solitary wave with parameters $v = 1$, $\varphi = 0$, $\Omega = 0$, and $t_0 = 0$ is used as the zeroth order solution. The first column of surface plots illustrates the amplitude of the electric field. The computational domain is taken to be $t \in [-10, 30]$, $z \in [0, 20]$. These plots reveal that, although the perturbations are local, they result in some emission of nonlocal radiation. This is due to second order effects in the perturbation. The second column of plots shows the profiles of the electric field amplitude at $z = 10$, or halfway through the simulation. The solid lines indicate the perturbed solution while the dashed lines represent the unperturbed solution for comparison. These plots reveal that the amplitude of the radiation emitted due to the perturbation is indeed second order in the perturbation parameter. Its amplitude is approximately $0.05^2 = 0.0025$. The radiation emitted in the unperturbed case is due to limitations of the numerical method. These plots also reveal that some of the modal perturbations induce a shift in the velocity of the pulse. This is seen for modes b and c,d. The final column of plots shows the deviation from the initial peak amplitude of the solitary wave as a function of distance. Again the solid lines indicate the perturbed solution while the dashed lines represent the unperturbed solution for comparison. The oscillatory behavior of the perturbed amplitude indicates that local mode(s) have indeed been excited, while the unperturbed solitary wave has a constant amplitude.

The linear stability analysis does not reveal the mechanism for pulse destruction

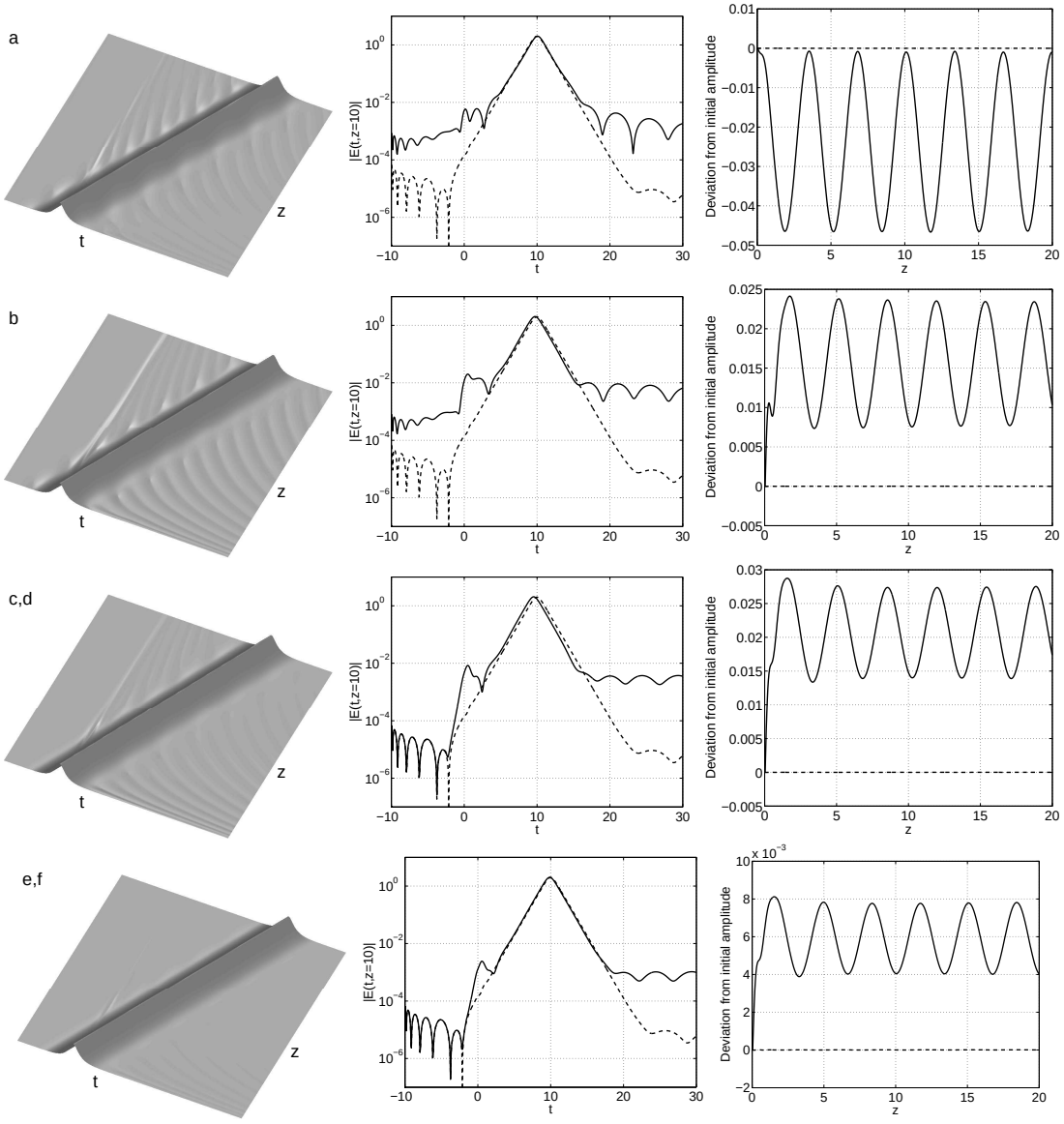

FIGURE 3.16. Numerical simulations showing the effects of modal perturbations on a solitary wave with $v = 1$, $\varphi = 0$, $\Omega = 0$, $t_0 = 0$, and $\delta = 0$. The second column shows the amplitude of emitted radiation is second order in the perturbation parameter whose value is 0.05. Solid and dashed lines indicate perturbed and unperturbed solitary waves, respectively. The $\mathcal{O}(10^{-5})$ radiation in the uperturbed case is due to limitations in the numerical method. The third column shows the peak amplitude of the pulse as a function of distance, where $\mathcal{O}(0.05)$ oscillations confirm the excitement of local modes.

in the phase-expanded case illustrated in Figure 3.10. However, it does reveal that the process is not linear. If it was, the spectrum corresponding to localized modes would have a positive imaginary part and the instability would develop according to a single characteristic scale. The nonlinearity of the destruction mechanism is evidenced by the two distinct scales involved with the instability. It is possible that a second-order perturbation analysis would reveal a nonlinear destruction mechanism in which the amplitude of the localized modes increases until the potential created by the zeroth-order solitary wave can no longer contain the localized modes, at which point the entire pulse energy is transferred to the radiation modes and energy confinement is lost.

3.5.4 Collision dynamics

With a better understanding of the dynamics of perturbed solitary waves, it is now possible to analyze their mutual interaction. The analysis in the previous subsection suggests that collisions between solitary waves will result in shifts in the pulse parameters v, Ω, φ, and/or t_0, excited localized modes, and the emission of radiation. Since there is no analytic theory describing the collision dynamics of MD solitary waves, numerical simulations are again used to examine the behavior.

As a result of extensive numerical and analytical studies of nonlinear evolution equations, it is known that interaction dynamics of solitary waves depend on the relative phase $\Delta\varphi = \varphi_1 - \varphi_2$ of the colliding waves. Therefore it is reasonable to

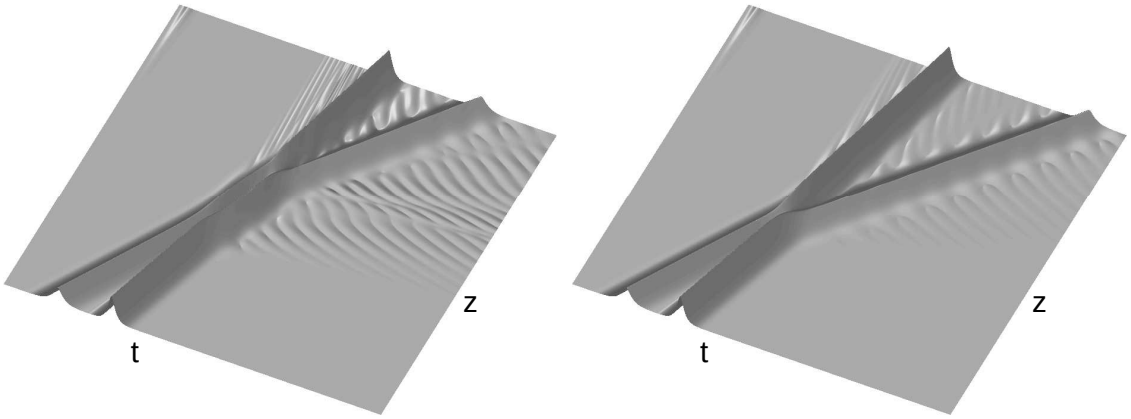

FIGURE 3.17. Collisions between solitary waves with $v_1 = 1$ and $v_2 = 2$. The left surface shows a collision where the initial relative phase of the solitary waves is $\Delta\varphi = 0$, while the right surface illustrates a $\Delta\varphi = \pi$ collision. Both collisions induce radiation emission, shifts in the characteristic parameters, and excitation of localized modes. However, the interaction distance is longer for the $\Delta\varphi = 0$ case.

study the the collision dynamics of the MD solitary waves as a function of $\Delta\varphi$. Figure 3.17 shows the amplitude of the electric field for two collision simulations in which solitary waves with $v_1 = 1$ and $v_2 = 2$ interact. In these simulations, the solitary wave frequencies are zero as is the detuning. The left surface shows the case when $\Delta\varphi = 0$, while the right surface indicates the $\Delta\varphi = \pi$ case. In both simulations, the collision results in the emission of radiation and shifts in the values of the characteristic solitary wave parameters. For example, it is clear from the figure that the pulse velocites are not preserved through the collision, for the angle of their trajectories changes after the collision. It is also evident that the waves do not pass through one another, rather they behave more like billiard balls. In the $\Delta\varphi = 0$ case, the pulses interact

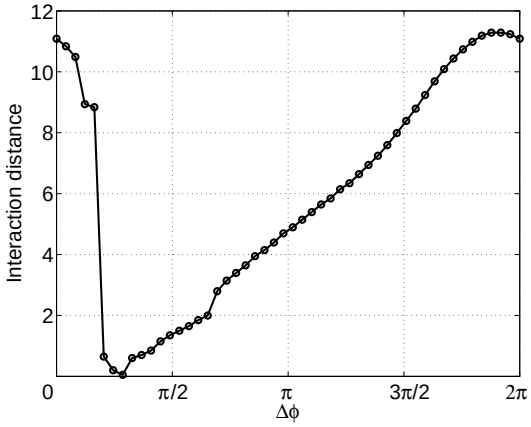

FIGURE 3.18. Interaction distance as a function of relative phase of colliding solitary waves. The jump near $\pi/4$ indicates a dramatic change in collision dynamics in this region of relative phase.

over a greater distance than in the $\Delta\varphi = \pi$ case. In collisions with long interaction distances, radiation is emitted during the interaction. Then after the collision, the pulses continue to emit excessive radiation as they adjust to the energy exchange and loss due to the collision. Collisions with short interaction distances do not allow much time for nonlinear mixing to occur so little radiation is emitted during the collision, and comparatively less radiation is emitted after the collision. To further investigate the interaction distance as a function of $\Delta\varphi$, the simulations are repeated for many values of $\Delta\varphi$ and the interaction distance is determined by measuring the distance over which the minimum between the two pulses is greater than the threshold value of 3/4 (chosen to best show the distance). The results of this analysis are presented in Figure 3.18. By this metric the interaction distance varies smoothly as a function of relative phase everywhere except in the region about $\Delta\varphi = \pi/4$. Here there is an

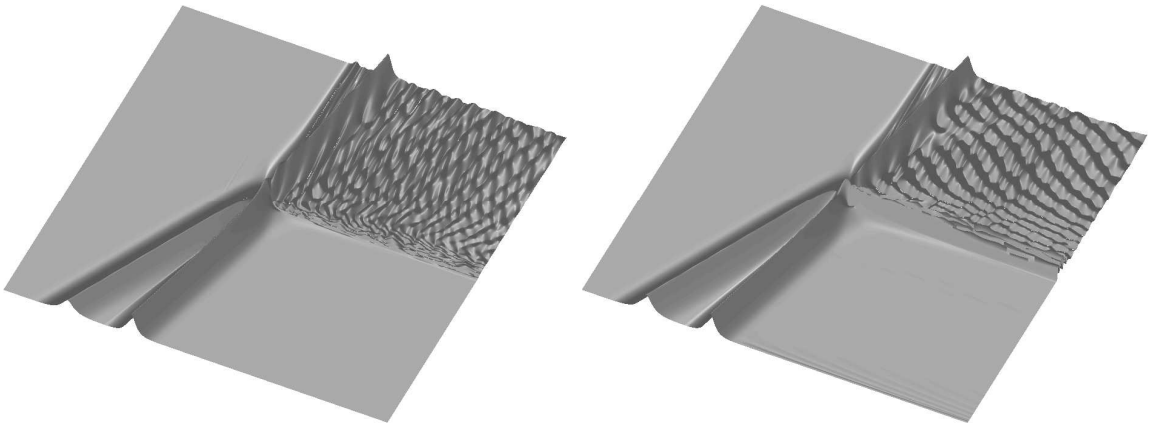

FIGURE 3.19. Electric (left) and material excitation (right) fields for a collision between pulses with velocities $v_1 = 1$ and $v_2 = 2$ and relative phase $\Delta\varphi = \pi/3$. The collision results in the immediate destruction of one pulse. Its energy is deposited into a localized region of material excitation where it persists long after the collision takes place. This "hotspot" continuously radiates energy back into the electric field.

abrupt change in the interaction distance, which suggests that a dramatic change in the collisiong dynamics occurs in this regime. The results of a numerical simulation of two pulses colliding with $\Delta\varphi = \pi/3$ is presented in Figure 3.19. The surface on the left, corresponding to electric field amplitude, shows that one pulse is destroyed in the collision while the other persists. The material excitation field amplitude, presented on the right, indicates that the pulse energy is converted into a localized hotspot in material excitation. This hotspot is observed to persist long after the collision takes place, during which time it slowly radiates energy back into the electric field.

To study the origin of this behavior, consider the MD equations on a rapidly-varying length scale $y = z/\epsilon$, where ϵ is a small parameter. Then Equation (3.9)

becomes

$$i\frac{\partial \mathcal{E}}{\partial y} = \epsilon \mathcal{Q}.$$

Expanding the fields in ϵ power series and collecting the zeroth order terms results in

$$i\frac{\partial \mathcal{E}_0}{\partial y} = 0.$$

Since only localized solutions are considered, the trivial integration in y obtains $\mathcal{E}_0 = 0$. Applying this result to Equation (3.10) yields the decoupled zeroth order expression

$$i\frac{\partial \mathcal{Q}_0}{\partial t} + \delta \mathcal{Q}_0 + |\mathcal{Q}_0|^2 \mathcal{Q}_0 = 0,$$

the solution of which is

$$\mathcal{Q}_0 = A(y) \exp[i\delta t + iA^2(y)t + i\psi(y)],$$

where A and ψ are the initial amplitude and phase of $\mathcal{Q}_0$. This analysis shows that rapid z-variations in the fields cause the equations to decouple in leading order. The resulting excitation of the medium is incoherent since the plasmonic oscillators are no longer strongly coupled through the electric field. This is why the topography of the hotspot is not smooth in Figure 3.19. Therefore certain values of the relative phase

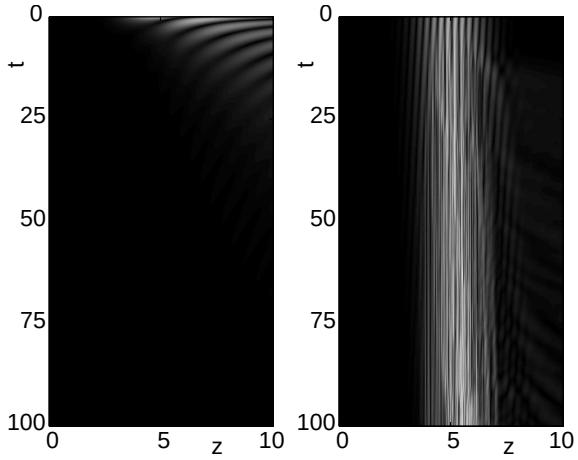

FIGURE 3.20. Intensity plots of the material excitation field amplitude for two different boundary conditions. On the left, the material is prepared with a smooth function $\mathcal{Q}(0,z) = \exp[-(z-5)^2]$, resulting in dispersion of the excitation through the sample. On the right, the high-gradient function $\mathcal{Q}(0,z) = \exp[-(z-5)^2]\sin(10z)$ results in a hotspot.

causes steep gradients to occur in the fields when the waves collide, resulting in the formation of a localized hotspot.

This analysis is verified by numerical simulation in Figure 3.20, where two different material states are prepared. In the left intensity plot of the material excitation field amplitude, the boundary condition $\mathcal{Q}(0,z) = \exp[-(z-5)^2]$ is used and the excitation simply disperses through the sample. The right plot uses $\mathcal{Q}(0,z) = \exp[-(z-5)^2]\sin(10z)$, the same boundary condition except modulated with a sinusoid, which has high gradients. The result is the formation of a hotspot.

These hotspots represent an alternative approach to the so-called "stopping light" phenomenon. This subject has been investigated in recent work concentrating on

stopping light in 3-level media [80] as well as defects in photonic crystal structures [81]. The research is motivated by potential applications in optical data storage, logic devices, and switching. The dramatic dependence of pulse interaction on relative phase suggests that nano-based, phase-controlled optical devices could be developed in a MD framework since pulse phase is easily controllable.

The numerical simulations indicate that the collision inelasticity depends on the relative phase of the colliding waves. A rough estimate of inelasticity may be obtained by measuring the amount of energy lost through the right boundary of the computational time domain $t = b$. The energy flux across this boundary may be measured using the energy conservation law (3.11). Integrating over the computational time domain results in

$$\frac{\partial}{\partial z}\int_b^a |E(t,z)|^2 \mathrm{d}t + |Q(a,z)|^2 - |Q(b,z)|^2 = 0.$$

This expression may be integrated from 0 to z to obtain

$$c_1 = \int_b^a |E(t,z)|^2 \mathrm{d}t + \int_0^z \left[|Q(a,z')|^2 - |Q(b,z')|^2\right] \mathrm{d}z'.$$

While Equation (3.11) leads to a conserved quantity on an infinite domain, this expression is the analogous quantity for the finite computational domain. The first integral is the density of energy on the grid, while the second integral keeps track of

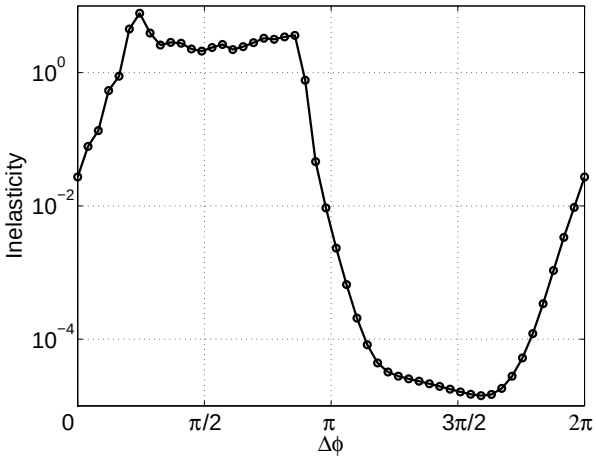

FIGURE 3.21. Collision inelasticity as a function of relative phase. The region of high inelasticity about $\Delta\varphi = \pi/2$ indicates values for which the collision results in hotspot formation or nealy-immediate pulse destruction. The region of low inelasticity about $\Delta\varphi = 3\pi/2$ represents quasielastic collision dynamics.

flux entering and exiting the domain. Because of the boundary condition $Q(a, z) = 0$ and since information only flows in the positive t and z directions, the flux through the $t = a$ boundary may be neglected, and the energy flux through the $t = b$ boundary is given by

$$f_b = \int_0^z |Q(b, z')|^2 \mathrm{d}z'.$$

This provides a means for numerically measuring the inelasticity of a collision, since a large portion of the radiation emitted during a collision trails the pulses and exits the domain through the $t = b$ boundary. A plot of this measurement as a function of $\Delta\varphi$ appears in Figure 3.21. This plot indicates that a large amount of energy passes

through the left time boundary in the region $\Delta\varphi \in [0.6, 2.7]$. This is due to waves which 1) survive the collision but are quickly destroyed and converted to continuous radiation which exits the domain through the $t = b$ boundary, or 2) for hotspots. Hotspots formation takes place in the region $\Delta\varphi \in [0.8, 1.6]$. The other region of interest in this figure is $\Delta\varphi \in [3.6, 5.5]$, where the inelasticity is measured as less than 10^{-4}. In this region the waves collide quasielastically. In fact, for $\Delta\varphi = 4.82$ the inelasticity is approximately 1.4×10^{-5}. The plots in Figure 3.22 show that for this value, the solitary waves collide elastically to numerical precision. The surface in Figure 3.22 shows the electric field amplitude when colliding pulses with $v_1 = 1$, $v_2 = 2$, and $\Delta\varphi = 4.82$. This plotting routine is particularly sensitive to changes in surface angle yet shows no indication of radiation emission at any time during the simulation. The lower graphs show the electric field amplitude profiles at the beginning (dashed) and end (solid) of the simulation. On the left, the solitary waves are presented on a linear scale which shows that the shapes and sizes of the waves are preserved after the collision. The difference in amplitude of the larger wave before and after the collision is measured as less than 0.027 (about 0.8% of the pulse amplitude). The right plot shows the pulse amplitudes on a log scale, which highlights the radiation present at the end of the simulation. Its amplitude is $\mathcal{O}(10^{-4})$, barely above numerical accuracy. This indicates that very little energy is lost to radiation and the collision is highly elastic. The low amplitude oscillations to the left of the pulses are a purely numerical effect.

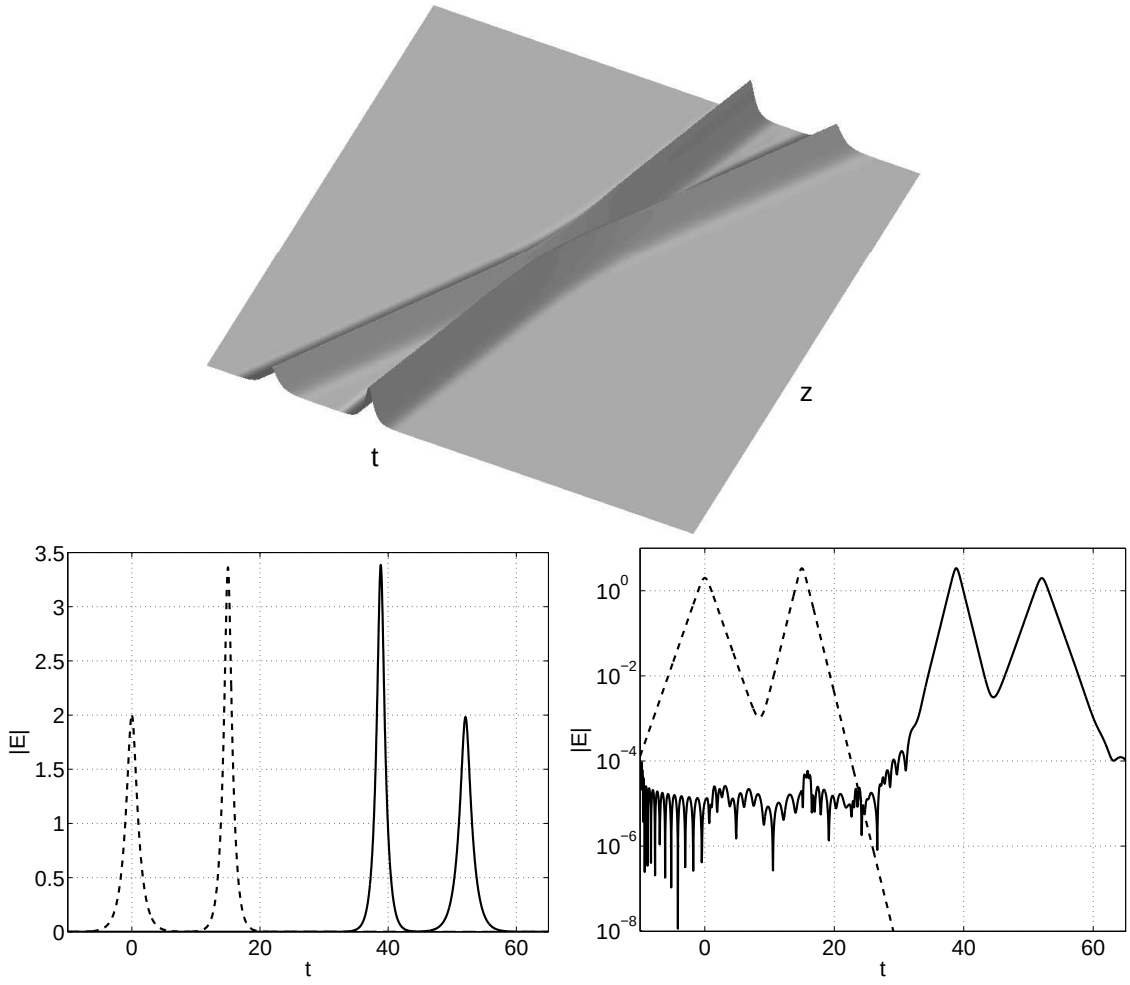

FIGURE 3.22. Numerical analysis of an elastic collision where the solitary waves have velocities $v_1 = 1$, $v_2 = 2$, and relative phase $\Delta\varphi = 4.82$. The surface shows no visible emission of radiation. The lower left plot shows the amplitude and shape of the waves is the same before the collision at $z = 0$ (dashed) and after the collision at $z = 50$ (solid). The lower right plot illustrates the same profiles on a log scale, where the $\mathcal{O}(10^{-4})$ amplitude of the radiation is observable.

3.6 Modulational instability

Perhaps the simplest nontrivial solutions to Equations (3.9) and (3.10) are stationary. This corresponds to a specific state of illumination and material preperation which will be made clear below. It is common to analyze the stability of such solutions since many nonlinear systems exhibit a modulational instability, in which localized pulses evolve from modulations in the constant amplitude "condensate" due to an intrinsic instability. In this section, such constant amplitude solutions are derived and their stability is analyzed.

3.6.1 Derivation of stationary solutions

Illuminating a sample with a continuous wave corresponds to time-independent evolution of the fields, in which case Equations (3.9) and (3.10) reduce to

$$
\begin{aligned}
i\frac{\partial \mathcal{E}_c}{\partial z} &= \mathcal{Q}_c \\
\mathcal{E}_c &= \left(\delta + |\mathcal{Q}_c|^2\right)\mathcal{Q}_c,
\end{aligned}
$$

where the subscript c denotes the condensate solution. Multiplying the first equation by $\mathcal{E}_c^*$ and subtracting the resulting expression from its complex conjugate, gives the

condition that

$$|\mathcal{E}_c| = \text{constant}.$$

Thus the only z-dependence of $\mathcal{E}_c$ is in its phase. Multiplying the second equation by $\mathcal{E}_c^*$, results in

$$|\mathcal{E}_c| = \left(\delta + |\mathcal{Q}_c|^2\right)|\mathcal{Q}_c|.$$

If detuning is zero, then $|\mathcal{Q}_c|$ is also constant. This condition allows the simple integration of

$$i\frac{\partial \mathcal{E}_c}{\partial z} = \mathcal{Q}_c = \mathcal{E}_c|\mathcal{Q}_c|^{-2},$$

which obtains the constant-amplitude condensate solutions

$$\begin{aligned}\mathcal{E}_c(z) &= \mathcal{E}_c(0)\exp\left[-iz|\mathcal{E}_c(0)|^{-2/3}\right] \\ \mathcal{Q}_c(z) &= \mathcal{E}_c(0)|\mathcal{E}_c(0)|^{-2/3}\exp\left[-iz|\mathcal{E}_c(0)|^{-2/3}\right].\end{aligned} \tag{3.29}$$

3.6.2 Stability of condensate solutions

To study the stability of these solutions the ansatz

$$\mathcal{E}(t,z) = \mathcal{E}_c(z)\psi(t,z), \quad \mathcal{Q}(t,z) = \mathcal{Q}_c(z)\phi(t,z)$$

is inserted into Equations (3.9) and (3.10) with $\delta = 0$. This yields equations for the modulation of the condensate:

$$i\psi_z|\mathcal{Q}_c|^2 + \psi = \phi, \quad i\phi_t|\mathcal{Q}_c|^{-2} + |\phi|^2\phi = \psi,$$

which may be simplified through the transformation $z = |\mathcal{Q}_c|^2\zeta$ and $t = |\mathcal{Q}_c|^{-2}\tau$ to obtain

$$i\psi_\zeta + \psi = \phi, \quad i\phi_\tau + |\phi|^2\phi = \psi. \tag{3.30}$$

Now let $\psi = 1 + e$ and $\phi = 1 + q$, where e and q are terms of subleading order, into (3.30) and linearize. This results in equations for the dynamics of the perturbations e and q:

$$ie_\zeta + e = q, \quad iq_\tau + 2q + q^* = e.$$

By separating real and imaginary parts $e = u + iv$ and $q = r + ip$ the linear system may be written as

$$u_\zeta + v = p$$

$$v_\zeta - u = -r$$

$$r_\tau + p = v$$

$$p_\tau - 3r = -u.$$

Now the plane wave ansatz $(u, v, r, p) = (\bar{u}, \bar{v}, \bar{r}, \bar{p})e^{i(k\zeta - \omega\tau)}$ is used to obtain the following linear system:

$$\begin{pmatrix} ik & 1 & 0 & -1 \\ -1 & ik & 1 & 0 \\ 0 & -1 & -i\omega & 1 \\ 1 & 0 & -3 & -i\omega \end{pmatrix} \begin{pmatrix} \bar{u} \\ \bar{v} \\ \bar{r} \\ \bar{p} \end{pmatrix} = 0.$$

The solutions for this system are obtained by setting the determinant of the coefficient matrix equal to zero. This results in the dispersion relation

$$k_\pm(\omega) = \frac{-\omega \pm \omega\sqrt{\omega^2 - 2}}{\omega^2 - 3}.$$

In practice a condensate never has an exactly constant amplitude. There is always at least a small amount of noise present. This noise has a broad spectrum and is the

perturbation which causes the modulational instability to initiate. The dispersion relation may be used to determine which frequency component of the noise grows the fastest. Values of ω for which k has a positive imaginary part correspond to growing modes. Thus the ω for which k has the largest imaginary part is the mode which grows the fastest. The frequency of the fastest growing mode is given by

$$\mathrm{Im}\frac{\mathrm{d}k_{\pm}}{\mathrm{d}\omega} = 0,$$

the solution of which is $\omega = \sqrt{3/2}$. This occurs at the wavenumber $k_{-} = 1/\sqrt{3}$.

A numerical simulation of the modulational instability is presented in Figure 3.23 using initial and boundary conditions $\mathcal{E}(t,0) = 1$ and $\mathcal{Q}(0,z) = \exp(-iz)$, which correspond to Equations (3.29) with $\mathcal{E}_c(0) = 1$. This figure shows that the amplitude of the condensate remains approximately 1 near the boundaries $t = 0$ and $z = 0$ until perturbations from the numerical approximation excite the modulational instability. The result from the fastest growing mode analysis provides the distance and time between evolved pulses. These values are given by the spatial and temporal periods of oscillation of the fastest growing mode, which are given by $2\sqrt{2/3}\pi$ and $2\sqrt{3}\pi$, respectively. The incident electric field evolves into a pulse train which propagates at a certain speed. The speed is determined by the phase velocity of the $\omega = \sqrt{3/2}$ mode,

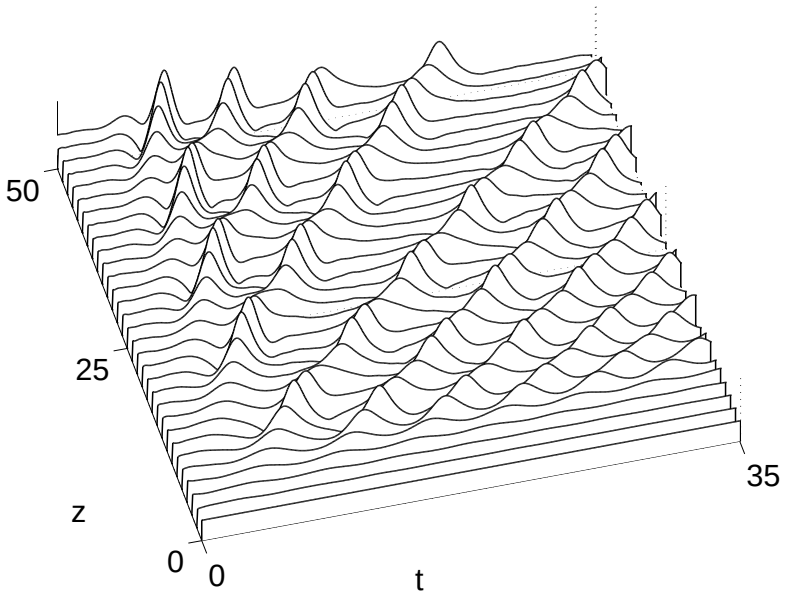

FIGURE 3.23. Amplitude of electric (left) field with initial and boundary conditions given by $\mathcal{E}(t,0) = 1$ and $\mathcal{Q}(0,z) = \exp(-iz)$. Two different kinds of pulse trains are produced from a modulational instability. The pulses resulting from the incident electric field

which may be determined from the dispersion relation. Plane waves are expressed as

$$\exp[i(k\zeta - \omega\tau)] = \exp[ik(\zeta - \omega\tau/k)] = \exp[ik(\zeta - v_p\tau)],$$

where the phase velocity $v_p = \omega/k$. Inserting the expression for $\mathrm{Re}(k_-)$ into the phase velocity and evaluating at $\omega = \sqrt{3/2}$ yields $v_p = 3/2$. Numerical simulations confirm that indeed the pulses propagate at this velocity.

The pulse train resulting from the incident electric field is not the unique feature of Figure 3.23. The boundary condition $\mathcal{Q}(0, z) = \exp(-iz)$ represents a prepared medium from which a different kind of pulse train develops. Since the governing equations are hyperbolic and there is a consequent principle of causality, this other pulse train is uneffected by the incident electric field. It is purely the result of the prepared medium. In this case, the pulses are more dynamic. Their amplitude gets larger and smaller in an oscillatory way. This is the result of energy exchange between the pulses and the condensate. These pulses extract energy from the condensate to grow in amplitude, then return their energy to the condensate and diminish in amplitude. This behavior is in direct analogy with NLS solitons which evolve from a condensate. In the NLS case, an analytic expression for the solitons is known [82]

$$E(x,t) = \frac{2\nu}{\mu}\left[\frac{\nu\cos(\Omega t) + i\mu\sin(\Omega t)}{\cosh(2\nu x) + E_0/\mu\cos(\Omega t)}\right],$$

where ν and μ are parameters, Ω is the oscillation frequency, and E_0 is the condensate amplitude. However, an analytic expression for the MD condensate solitons remains unknown.

3.7 Self-similar solutions

In the case of zero detuning, the MD equations are written

$$i\frac{\partial \mathcal{E}}{\partial z} = \mathcal{Q}$$
$$i\frac{\partial \mathcal{Q}}{\partial t} + |\mathcal{Q}|^2\mathcal{Q} = \mathcal{E}.$$

This system exhibits self-similar behavior, which may be seen by making the transformation

$$\mathcal{E}(t,z) = z^{3/2}A(\zeta), \quad \mathcal{Q}(t,z) = z^{1/2}\rho(\zeta), \tag{3.31}$$

where the self-similarity variable $\zeta = (2zt)^{1/2}$. Under this transformation, the MD equations reduce to the following set of nonconstant coefficient ordinary differential equations:

$$\frac{\mathrm{d}A}{\mathrm{d}\zeta} = (2\rho - 3A)/\zeta, \tag{3.32}$$
$$\frac{\mathrm{d}\rho}{\mathrm{d}\zeta} = i\zeta|\rho|^2\rho - \zeta A. \tag{3.33}$$

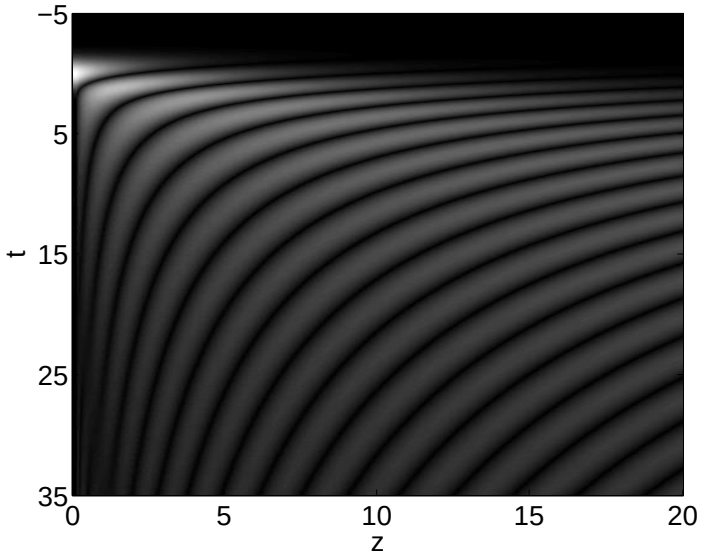

FIGURE 3.24. Numerical simulation showing self-similar hyperbolic patterns in low-amplitude radiation as provided by the initial condition $\mathcal{E}(t,0) = 0.3\exp(-t^2)$. In this intensity plot, the amplitude of the electric field is raised to the 3/4 power to emphasize low amplitude variations.

Considering a fixed ζ_0, it may be seen that the self-similarity variable represents a family of hyperbola:

$$t = \zeta_0^2/2z.$$

This characteristic is verified by the numerical simulation shown in Figure 3.24, where a low amplitude Gaussian pulse $\mathcal{E}(t,0) = 0.3\exp(-t^2)$ is used as the initial condition. The self-similar hyperbola are clearly visible.

The solution of Equation (3.32) is singular at the point $\zeta = 0$ unless

$$2\rho(0) = 3A(0). \tag{3.34}$$

Therefore this condition is required for physically meaningful solutions and reduces the dimensionality of the initial conditions to one. Equations (3.32) and (3.33) are invariant to a sign change in ζ, which implies that solutions of the system are even functions.

The self-similar behavior of this system may be analyzed further by making the transformation $A = B\zeta^{-3}$. Applying this to Equation (3.32) results in the condition $\mathrm{d}B/\mathrm{d}\zeta = 2\zeta^2\rho$. Equation (3.33) becomes

$$\zeta^2 \frac{\mathrm{d}\rho}{\mathrm{d}\zeta} = i\zeta^3|\rho|^2\rho - B,$$

which, after differentiating with respect to ζ, substituting $\mathrm{d}B/\mathrm{d}\zeta = 2\zeta^2\rho$, and dividing by ζ^2, results in

$$\frac{\mathrm{d}^2\rho}{\mathrm{d}\zeta^2} + \frac{2}{\zeta}\frac{\mathrm{d}\rho}{\mathrm{d}\zeta} + 2\rho = 3i|\rho|^2\rho + i\zeta\frac{\mathrm{d}}{\mathrm{d}\zeta}(|\rho|^2\rho). \tag{3.35}$$

In this form it is easy to see that for low amplitudes the nonlinear terms are small and this reduces to Bessel's equation of order zero. A numerical simulation of Equations (3.32) and (3.33) reveals this low amplitude behavior, and is presented in the left plot

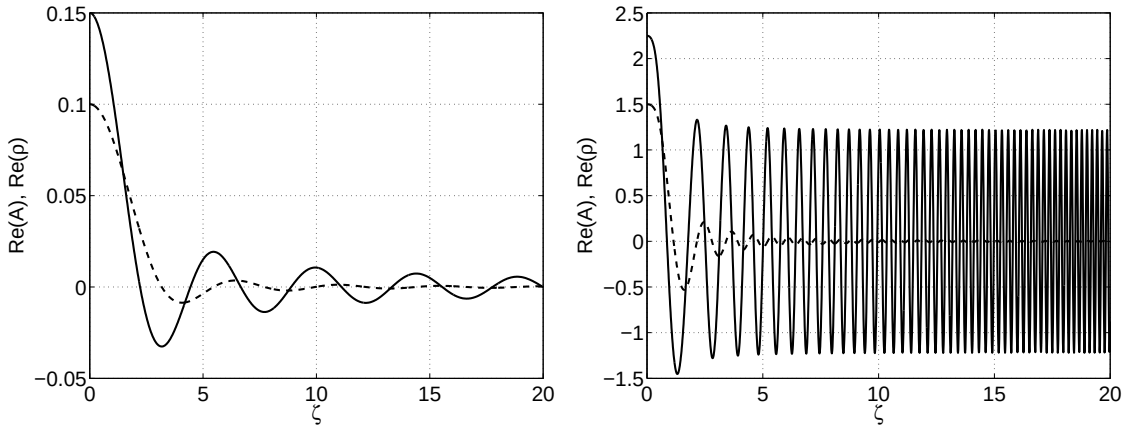

FIGURE 3.25. Numerical integration of the self-similarity equations (3.32) and (3.33). The solid lines indicate the real part of ρ and the dashed lines indicate the real part of A. The left plot shows the solution in the low amplitude regime, where the initial conditions $A(0) = 0.1$ and $\rho(0) = 0.15$ are used, showing the zeroth order Bessel function-like behavior of ρ. The right plot shows the asymptotic behavior of A and ρ, characterized by decay to zero and constant amplitude oscillations of increasing frequency, respectively.

in Figure 3.25. This plot shows the real part of A and ρ using the initial conditions $A(0) = 0.1$ and $\rho(0) = 0.15$, as requred by condition (3.34). In this regime, the real part of the solution is much larger than the imaginary part since only the nonlinear terms have imaginary coefficients. This makes the imaginary part negligibly small $(\mathcal{O}(\rho^3(0)))$.

Long-ζ behavior may also be analyzed by multiplying Equation (3.35) through by ζ^2 and combining the total derivatives, resulting in

$$(\zeta^2\rho')' + 2\zeta^2\rho = i(\zeta^3|\rho|^2\rho)',$$

where the primes denote differentiation with respect to ζ. As $\zeta \to \infty$, the second term on the left hand side makes a negligible contribution. The remaining terms may be integrated with respect to ζ, which yields the first order differential equation

$$\rho' = i\zeta|\rho|^2\rho.$$

The constant of integration is zero since ρ vanishes at infinity (this is a consequence of transformation (3.31) and the fact that E, Q, and their derivatives vanish at $\pm\infty$). The solution of this equation is

$$\rho(\zeta) = \rho(0)\exp(i|\rho(0)|^2\zeta^2/2),$$

which characterizes constant amplitude oscillations whose frequency increases linearly with ζ. Substituting this expression into Equation (3.32), it is clear that A decays to zero asymptotically. These observations are confirmed by the results of a numerical integration of the self-similarity equations (3.32) and (3.33) shown in the right plot of Figure 3.25. After a transient, the amplitude of ρ settles down to a constant, while its oscillations increase in frequency as predicted by the analysis above.

3.8 Numerical analysis of the MD equations

The discovery of most of the interesting dynamics presented in this chapter, namely the stability of solitary waves, collision dynamics, the evolution of arbitrarily shaped initial pulses, as well as the nonlinear development of pulse trains due to the modulational instability of constant-amplitude solutions, have been made using numerical simulations. All these phenomena are analyzed numerically since the corresponding analytic theory remains elusive. This is precisely the situation in which numerical methods show their power and practicality. This section details the methods used to obtain the results presented in the preceeding sections.

3.8.1 Numerical estimation of spectrum

Since the operator $\hat{L}$ is non-self-adjoint, none of the analytic theory of self-adjoint operators is applicable toward determining its spectrum. Thus, the problem is studied numerically by discretizing the operator and using an eigensolver to determine its eigenvalues and eigenvectors. Since the operator is nonlocal (it contains an integral term), its discretization results in a dense matrix, regardless of the discretization method. The determinization of all the eigenvalues and eigenvectors of a dense $N \times N$ matrix is an expensive $\mathcal{O}(N^4)$ computation. Thus it is important to use a high-order discretization to reduce the dimensionality of the problem and make it computationally tractible. This is accomplished using standard center difference approximations

	k				
p	1	2	3	4	5
2	$1/2$				
4	$2/3$	$-1/12$			
6	$3/4$	$-3/20$	$1/60$		
8	$4/5$	$-1/5$	$32/840$	$-1/280$	
10	$5/6$	$-5/21$	$5/84$	$-5/504$	$1/1260$

TABLE 3.2. Coefficients $\alpha_k^{(p)}$ for first derivative center difference approximations with $\mathcal{O}(h^p)$ accuracy and stencil size $p+1$.

for the derivative terms and endpoint corrected trapezoid rules for the integral terms.

A center difference approximation of the first derivative may be written

$$u'_j = \frac{1}{h}\sum_{k=1}^{p/2} \alpha_k^{(p)}(u_{j+k} - u_{j-k}) + \mathcal{O}(h^p),$$

where $u_j = u(\xi_j)$, h is the mesh spacing, and the coefficients $\alpha_k^{(p)}$ are shown for approximations up to tenth order accuracy in Figure 3.2. The matrix form of the center difference approximation is sparse and has bandwidth $p+1$. For example, the fourth-order first derivative operator has the form

$$u'(\xi) = \frac{1}{12h}\begin{pmatrix} 0 & -8 & 1 & & & & \\ 8 & 0 & -8 & 1 & & & \\ -1 & 8 & 0 & -8 & 1 & & \\ & \ddots & \ddots & \ddots & \ddots & \ddots & \\ & & -1 & 8 & 0 & -8 & 1 \\ & & & -1 & 8 & 0 & -8 \\ & & & & -1 & 8 & 0 \end{pmatrix}\begin{pmatrix} u_1 \\ u_2 \\ u_3 \\ \vdots \\ u_{N-2} \\ u_{N-1} \\ u_N \end{pmatrix} + \mathcal{O}(h^4).$$

For integrating periodic analytic functions, the trapezoid rule converges exponentially fast. The usual second-order accuracy of the method comes from the endpoints of the integration interval for nonperiodic functions. To increase the accuracy of the numerical integration, a family of endpoint-corrected trapezoid rules were developed. These rules incorporate information about the function outside the integration interval to reduce the error incurred at the endpoints, since the interior region of integration is exponentially accurate. The endpoint corrected trapezoid rule is written as

$$\int_a^b u(\xi)\mathrm{d}\xi = T(u) + h\sum_{k=1}^{p/2} \beta_k^{(p)}(-u_{1-k} + u_{1+k} + u_{N-k} - u_{N+k}) + \mathcal{O}(h^p),$$

where the interval is represented on N meshpoints with $a = \xi_1$ and $b = \xi_N$, and the usual trapezoid rule approximation for this integral is given by

$$T(u) = \frac{h}{2}(u_1 + u_N) + h\sum_{n=2}^{N-1} u_n.$$

The coefficients $\beta_k^{(p)}$ are shown for approximations up to sixth order in Table 3.3. A general formula for coefficients for higher order approximations are given in reference [83]. The matrix form of the uncorrected trapezoid rule for approximating the antiderivative of a function f is given by

p	k	
	1	2
4	$1/24$	
6	$41/720$	$-11/1440$

TABLE 3.3. Coefficients $\beta_k^{(p)}$ for endpoint corrected trapezoid rules of $\mathcal{O}(h^p)$ accuracy.

$$\int_{-\infty}^{\xi} u(\xi')\mathrm{d}\xi' = h \begin{pmatrix} 0 & & & & \\ 1/2 & 1/2 & & & \\ 1/2 & 1 & 1/2 & & \\ \vdots & \vdots & \ddots & \ddots & \\ 1/2 & 1 & \cdots & 1 & 1/2 \end{pmatrix} \begin{pmatrix} u_1 \\ u_2 \\ u_3 \\ \vdots \\ u_N \end{pmatrix} + \mathcal{O}(h^2).$$

For localized integrand functions which decay exponentially, such as those considered in this work, the $\mathcal{O}(h^2)$ error in computing the antiderivative comes from the right endpoint in regions where the modulus of the function is large. This is because the value of the function at the left endpoint is exponentially small, so any error introduced there is likewise exponentially small. Consider part of the calculation of the antiderivative function, for example the value of the antiderivative of hyperbolic secant at $\xi = 1$. This computation is represented in Figure 3.26 as the area of the shaded region. For this kind of calculation, only the right endpoint needs to be corrected to improve the accuracy of the method. Thus the following fourth-order right endpoint-corrected trapezoid rule approximation of the antiderivative is sufficient:

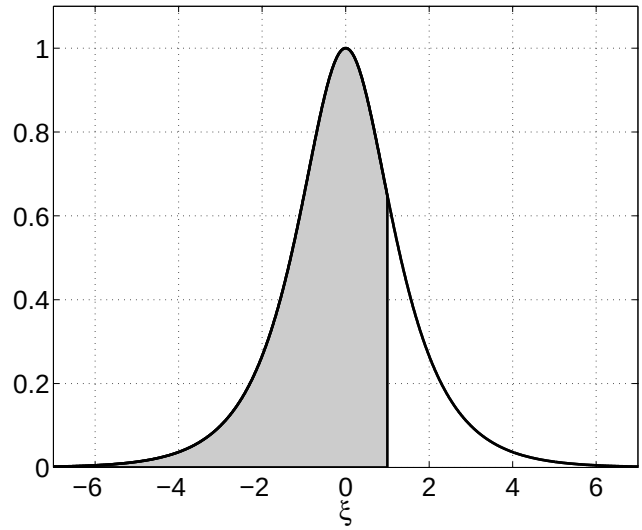

FIGURE 3.26. The antiderivative of hyperbolic secant at the point $\xi = 1$ is given by the area of the shaded region. The $\mathcal{O}(h^2)$ error induced by the trapezoid rule comes from the right endpoint ($\xi = 1$).

$$\int_{-\infty}^{\xi} u(\xi')\mathrm{d}\xi' = h \begin{pmatrix} 0 & & & & & \\ 1/2 & 1/2 & & & & \\ 1/2 & 1 & 1/2 & & & \\ 1/2 & 1 & 25/24 & 1/2 & -1/24 & \\ \vdots & \vdots & \ddots & \ddots & \ddots & \ddots \\ 1/2 & 1 & \cdots & 1 & 25/24 & 1/2 \end{pmatrix} \begin{pmatrix} u_1 \\ u_2 \\ u_3 \\ u_4 \\ \vdots \\ u_N \end{pmatrix} + \mathcal{O}(h^4).$$

In this approximation, the first few points of the antiderivative function are computed using the regular trapezoid rule which produces only an exponentially small error since the value of the function is exponentially small at the left endpoint.

Using these approximations, the discrete version of $\hat{L}$ has nonzero entries as indicated in Figure 3.27 in the illustrative case where the function is computed on only

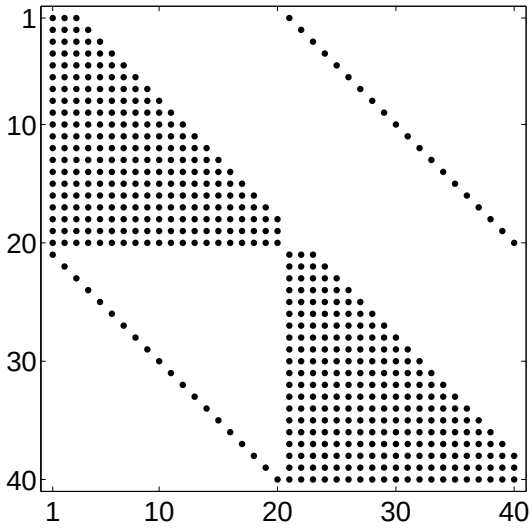

FIGURE 3.27. Nonzero entries in the $\mathcal{O}(h^4)$ approximation of $\hat{L}$ on a 20-point grid.

20 gridpoints and fourth-order approximations are used.

3.8.2 Trapezoid rule for integrating the MD equations

The numerical integration the MD equations requires the propagation of initial and boundary data, given by $\mathcal{E}(t,0)$ and $\mathcal{Q}(a,z)$ throughout the rectangular computational window $z \in [0,Z]$, $t \in [a,b]$. Two uniform grids are used to represent the $\mathcal{E}$ and $\mathcal{Q}$ fields, on which Δt and Δz are the mesh spacing and the points $t_j = a + j\Delta t$ and $z_n = n\Delta z$. This section describes the discretization of the MD equations on these grids, the implementation, and the analysis of the numerical scheme.

Since the MD equations posess conservation laws, a prudent choice of discretization is one which preserves at lease one of the conserved quantities. Equations of the form $u' = if(|u|)u$ conserve the quantity $|u|^2$ (energy) and this property is preserved

under discretization using the trapezoid rule. Equation 3.10 is of this form, except that it has a forcing term, the electric field envelope. This discretization works well for the problem since it is a single step method, requiring information from one previous gridpoint in each of the t and z directions. Moreover, it does not require knowledge of the field at intermediate stages, which is unavailable. Applying this discretization to Equations 3.9 and 3.10 results in

$$\mathcal{E}_j^n = \mathcal{E}_j^{n-1} - i\tfrac{\Delta z}{2}\left(\mathcal{Q}_j^n + \mathcal{Q}_j^{n-1}\right),$$
$$\left[1 - i\tfrac{\Delta t}{2}\left(\delta + |\mathcal{Q}_j^n|^2\right)\right]\mathcal{Q}_j^n = \left[1 + i\tfrac{\Delta t}{2}\left(\delta + |\mathcal{Q}_{j-1}^n|^2\right)\right]\mathcal{Q}_{j-1}^n - i\tfrac{\Delta t}{2}\left(\mathcal{E}_j^n + \mathcal{E}_{j-1}^n\right).$$

Note that both fields at point (j, n) may be computed by solving this system using the field values at points $(j-1, n)$ and $(j, n-1)$. The equation for $\mathcal{Q}_j^n$ is both nonlinear and therefore must be solved iteratively at each gridpoint.

Nonlinear iterations The $\mathcal{Q}_j^n$ equation may be solved using Newton's method by splitting it into real and imaginary parts, or by considering a system of the unknown and its complex conjugate. In either case, a system of two nonlinear equations must be solved at each gridpoint, and Newton's method is very efficient for this type of problem.

Consider the problem of finding points on the u-v plane such that the surfaces $f(u, v)$ and $g(u, v)$ equal zero. In the absence of an exact solution, and iterative numerical scheme called Newton's method may be used to find the roots provided

the scheme yields a contraction mapping. Expanding these functions in a Taylor series about the unknown points at which the functions are zero:

$$f(u,v) = f(u_0,v_0) + (u-u_0)\frac{\partial f}{\partial u} + (v-v_0)\frac{\partial f}{\partial v} + \cdots = 0$$
$$g(u,v) = g(u_0,v_0) + (u-u_0)\frac{\partial g}{\partial u} + (v-v_0)\frac{\partial g}{\partial v} + \cdots = 0$$

Omitting the higher order terms represented by the $\cdots$ results and replacing u and v with the current iterate and u_0 and v_0 with the previous iterate obtains the system

$$\mathbf{u}_{k+1} = \mathbf{u}_k - J^{-1}\mathbf{F},$$

where

$$\mathbf{u} = \begin{pmatrix} u \\ v \end{pmatrix}, \quad J = \begin{pmatrix} f_u & f_v \\ g_u & f_v \end{pmatrix}, \quad \mathbf{F} = \begin{pmatrix} f \\ g \end{pmatrix},$$

and J^{-1} and $\mathbf{F}$ are evaluated at $\mathbf{u}_k$.

In order to ensure that the iteration converges to the correct fixed point, it is necessary to choose a starting point which is near the fixed point. Since the fields are continuous, a good initial guess is provided by the solution obtained at the previous gridpoint. Taking this one step further, fewer iterations may be required by

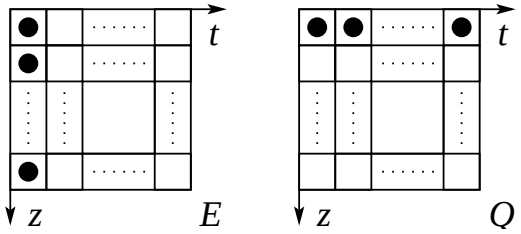

FIGURE 3.28. Initial information on the $\mathcal{E}$ and $\mathcal{Q}$ grids. Grid cells with known values are indicated with dots.

extrapolating the initial guess from nearby points according to

$$\mathcal{Q}_{init} = 2\mathcal{Q}^n_{j-1} - \mathcal{Q}^n_{j-2}.$$

This allows Newton's method to converge to the tolerance limited by the discretization error $[\mathcal{O}(\Delta t^2)]$ in three or fewer iterations. Further code performance enhancements may be realized by linearizing the equation for $\mathcal{Q}^n_j$ in regions where the cube of the material field amplitude is smaller than the discretization error. In such regions the nonlinearity makes a negligible contribution and may be ignored. Thus the linearized equations may be solved directly in these (usually large) regions of the computational domain.

Implementation The initial state of the problem may be represented on two grids, one for each complex field. Figure 3.28 indicates the known values of the grids provided by the initial and boundary data. The Maxwell-Duffing equations are written using optical coordinates, where z is considered the evolution variable. Thus the integration

should proceed by solving for the grid values in a columnwise fashion; the integration in t is performed for the first column before advancing on to the next column. The values of $\mathcal{E}$ on the first column of the grid are given by the initial condition, but it remains to determine the first column of $\mathcal{Q}$ values. These may be obtained by solving Equation (3.10), which is reduced to an ordinary differential equation in t forced by the known initial electric field envelope with the initial value given by $\mathcal{Q}(a)$. On the first column, the trapezoid rule discretization gives

$$\left[1 - i\tfrac{\Delta t}{2}\left(\delta + |\mathcal{Q}_j^0|^2\right)\right]\mathcal{Q}_j^0 = \left[1 + i\tfrac{\Delta t}{2}\left(\delta + |\mathcal{Q}_{j-1}^0|^2\right)\right]\mathcal{Q}_{j-1}^0 - i\tfrac{\Delta t}{2}\left(\mathcal{E}_j^0 + \mathcal{E}_{j-1}^0\right).$$

Here the the subscript index represents the jth gridpoint in the t-direction and the superscript index 0 indicates the zeroth integration step in the z-direction. This nonlinear equation for $\mathcal{Q}_j^1$ may be solved using Newton's method for each $j > 0$ on the grid.

With the first $\mathcal{Q}$-column filled, the numerical grids are now represented by Figure 3.29 and the procedure for computing the rest of the grids is given by Equations 3.36.

Convergence To test the convergence properties of the trapzoid rule on the MD eqution, the simulation results are compared with the known analytic solitary wave solution (3.22) with zero detuning and parameters $v = 1$ and $\alpha = \Omega = t_0 = 0$. Surface plots of the electric and material excitation field amplitudes appear in Figure

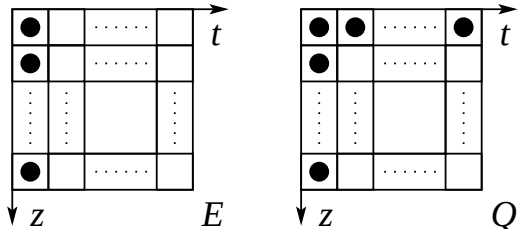

FIGURE 3.29. Computed gridcells after initial integration of Equation (3.10).

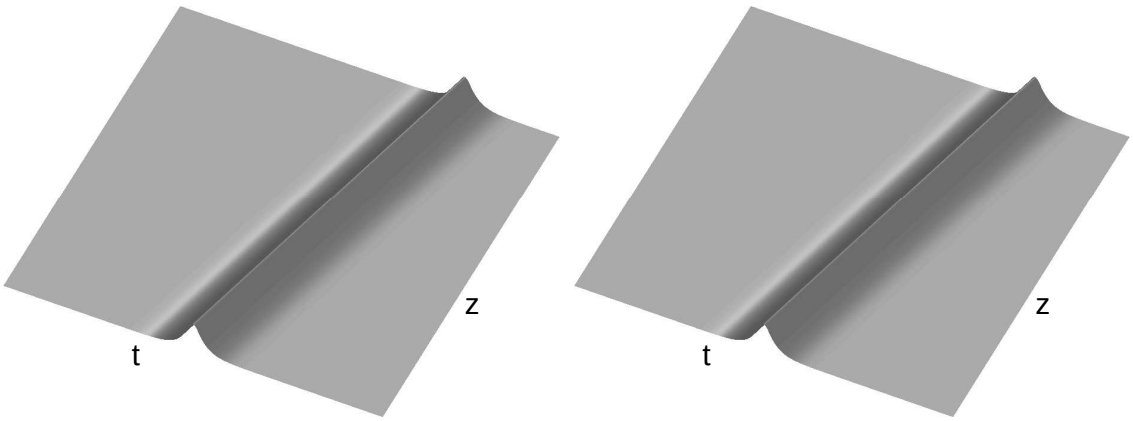

FIGURE 3.30. Electric (left) and material excitation (right) field amplitudes for the solitary wave solution (3.22) with zero detuning and parameters $v = 1$ and $\alpha = \Omega = t_0 = 0$.

3.30. The boundary condition $Q(a, z) = 0$ is used in numerical simulations, which produces a small error due to the fact that the analytic solutions are nonzero everywhere. However, the solutions decay exponentially as $t \to \pm\infty$, so this boundary error may be controlled by making $a \gg t_0$. For the convergence analysis, the computational domain $z \in [0, 10]$, $t \in [-20, 20]$ is chosen (as shown in Figure 3.30) so that errors in the boundary condition are smaller than the error induced by the numerical

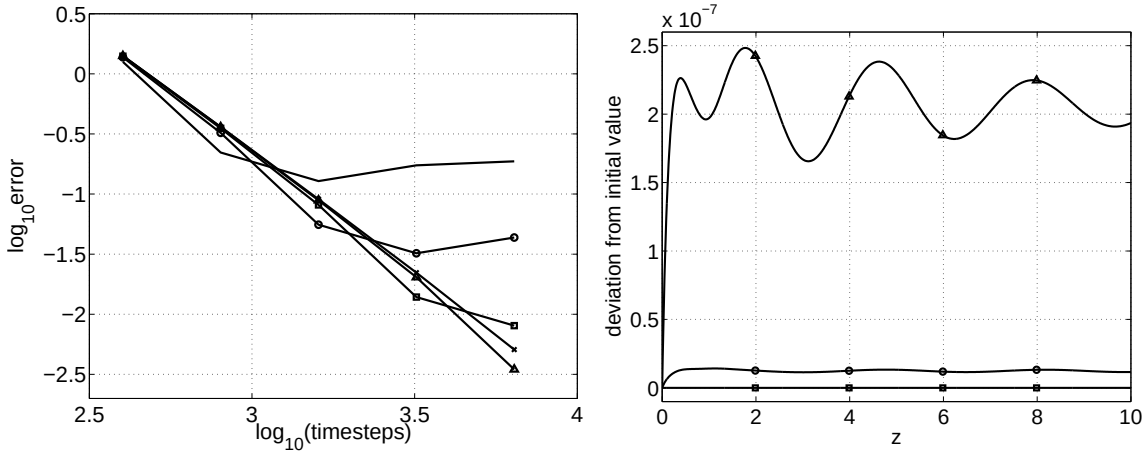

FIGURE 3.31. Left: convergence of the trapezoid method simulating single pulse propagation. The solid line refers to a spatial discretization using 101 points, while circles, squares, triangles, and x's indicate 201, 401, 801, and 1601 points, respectively. Right: deviation from initial values of the conserved quantities c_1 (circles), c_2 (squares), and c_3 (triangles) as a function of propagation distance using $\Delta t = 0.00625$ and $\Delta z = 0.0125$.

method. Therefore the convergence analysis only shows error from integration, not from initial and boundary data. The error is measured as the integrated modulus of the difference between the numerical and analytical solutions at $z = 10$. The results of the convergence analysis appear in Figure 3.31. With adequate resolution, the slope of curves is ~ -2, which verifies the $\mathcal{O}(\Delta t^2)$ convergence of the trapezoid discretization. The conserved quantities c_1, c_2, and c_3 are also plotted as functions of z in Figure 3.31. Zooming in on the curves reveals that the maximum deviations $\Delta c_1 < 1.5 \times 10^{-8}$, $\Delta c_1 < 10^{-13}$, and $\Delta c_1 < 2.5 \times 10^{-7}$ in this simulation.

3.8.3 Predictor-corrector methods for the MD equations

Higher order integrators for the MD equations may be constructed using linear multistep methods. A good compromise between stability and efficiency is made using a predictor-corrector scheme, in which an Adams-Bashforth explicit multistep method is used as a predictor for an Adams-Moulton implicit multistep corrector. When applied to the problem $u'(x) = f(u, x)$, an Adams-Bashforth method of order p is given by

$$u_{n+1} = u_n + h \sum_{j=1}^{p} \alpha_j f(u_{n-j+1}, x_{n-j+1}),$$

where $u(x) = u(hn) = u_n$ on the computational grid and h is the grid spacing. The Adams-Bashforth method of order p is given by

$$u_{n+1} = u_n + h \sum_{j=1}^{p} \beta_j f(u_{n-j+2}, x_{n-j+2}).$$

In these formulae, the coefficients α_j and β_j are presented in Tables 3.4 and 3.5, respectively. Combining these formulae, the multistep predictor-corrector of order p

	j					
p	1	2	3	4	5	6
1	1					
2	$^3/_2$	$^{-1}/_2$				
3	$^{23}/_{12}$	$^{-4}/_3$	$^5/_{12}$			
4	$^{55}/_{24}$	$^{-59}/_{24}$	$^{37}/_{24}$	$^{-3}/_8$		
5	$^{1901}/_{720}$	$^{-1387}/_{360}$	$^{109}/_{30}$	$^{-637}/_{360}$	$^{251}/_{720}$	
6	$^{4277}/_{1440}$	$^{-2641}/_{480}$	$^{4991}/_{720}$	$^{-3649}/_{720}$	$^{959}/_{480}$	$^{-95}/_{288}$

TABLE 3.4. Coefficients α_j for Adams-Bashforth methods.

	j					
p	1	2	3	4	5	6
1	1					
2	$^1/_2$	$^1/_2$				
3	$^5/_{12}$	$^2/_3$	$^{-1}/_{12}$			
4	$^9/_{24}$	$^{19}/_{24}$	$^{-5}/_{24}$	$^1/_{24}$		
5	$^{251}/_{720}$	$^{323}/_{360}$	$^{-11}/_{30}$	$^{53}/_{360}$	$^{-19}/_{720}$	
6	$^{95}/_{288}$	$^{1427}/_{1440}$	$^{-133}/_{240}$	$^{241}/_{720}$	$^{-173}/_{1440}$	$^3/_{160}$

TABLE 3.5. Coefficients β_j for Adams-Moulton methods.

is given by

$$v = u_n + h \sum_{j=1}^{p} \alpha_j f(u_{n-j+1}, x_{n-j+1}),$$
$$u_{n+1} = u_n + h \left[\beta_1 f(v, x_n) + \sum_{j=2}^{p} \beta_j f(u_{n-j+2}, x_{n-j+2}) \right].$$

The disadvantage of this method is that $\mathcal{O}(h^p)$ accuracy requires p gridpoints to advance the solution. This is not a problem integrating in the t-direction, since the fields are exponentially small ahead of the pulse and the first p points may be considered zero. In the z-direction, however, initial data for the electric field envelope must be provided. For simulations involving solitary waves, the analytic solution gives the necessary data. For arbitrary initial data, the electric field is assumed stationary for the first p propagation steps, which corresponds to propagation through the host medium in the absence of metallic nanoparticles. The resonance interaction then begins at $z = p\Delta z$. The implementation of this integration method goes in much the same way as it does for the trapezoid method.

Convergence A convergence analysis for the fourth-order predictor-corrector appears in Figure 3.32. This order of scheme was chosen because it is stable and accurate for the Δt and Δz values used in the analysis of the trapezoid method for purposes of comparison of the two methods (the analysis was attempted with the sixth-order predictor-corrector but was unstable on the coarsest grid). Fourth-order convergence

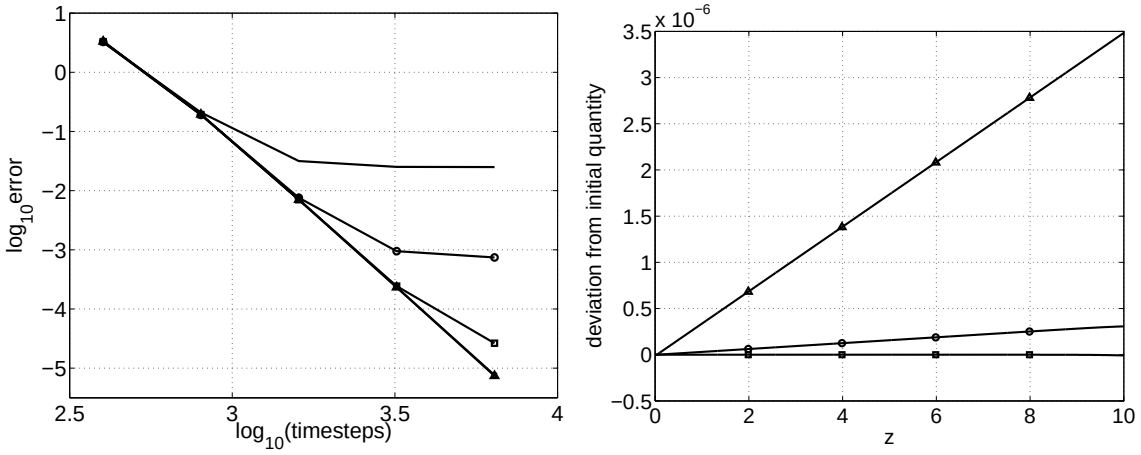

FIGURE 3.32. Left: convergence of the $\mathcal{O}(\Delta t^4, \Delta z^4)$ predictor-corrector method simulating single pulse propagation. The solid line refers to a spatial discretization using 101 points, while circles, squares, triangles, and x's indicate 201, 401, 801, and 1601 points, respectively (note the x's and triangles overlap one another). Right: deviation from initial values of the conserved quantities c_1 (circles), c_2 (squares), and c_3 (triangles) as a function of propagation distance using $\Delta t = 0.00625$ and $\Delta z = 0.0125$.

is verified by the slope of ~ -4 when adequate resolution is acheived. This Figure also shows how the scheme preserves the conserved quantities, which are characterized by linear growth in z rather than the oscillatory behavior observed using the trapezoid rule of the previous section. Zooming in on the plot reveals the maximum deviations $\Delta c_1 < 3.5 \times 10^{-7}$, $\Delta c_1 < 10^{-8}$, and $\Delta c_1 < 3.5 \times 10^{-6}$ in this simulation.

This analysis shows that the trapezoid method offers superior conservation performance, while the predictor-corrector offers greater accuracy. Also, since the trapezoid method requires the solution of a complex-valued nonlinear equation at each gridpoint, while the predictor corrector requires only two function evaluations per gridpoint, there is a huge difference in their computational costs. My Matlab implementations show the sixth-order predictor corrector is 15 times faster than the trapezoid method for modest-size problems (1000×500 grid). The expense of the trapezoid method is not useless, since it buys both preservation of the conserved quantities and unconditional stability.

3.9 Conclusions

In this chapter, the resonant interaction of an optical field with plasmonic oscillations in metallic nanoparticles is studied in an envelope approximation. The governing Maxwell-Duffing equations are found to confer a family of solitary wave solutions whose stability depends on the nature of the applied perturbation. In one case,

the wave emits radiation but ultimately persists. The other case causes radiation emission and a nonlinear degenerative process which culminates in the destruction of the wave. The system is found to exhibit self-induced transparency, and input pulses evolve into solitary waves and continuous radiation. The number of waves that evolve from the initial pulse is determined by the input pulse parameters. In contrast to known nonlinear evolution equations, the collision dynamics of the MD solitary waves vary dramatically depending on their relative phase. One specific value of relative phase results in an elastic collision, while another results in the immediate conversion of one of the waves to a localized hotspot of material excitation as well as continuous radiation. This hotspot persists long after the collision takes place and represents a new mechanism of stopping light. Modulational instability is studied and its characteristic parameters are determined. Self-similarity equations are derived from the MD system and analyzed. Finally, the numerical methods used in all of the above-mentioned studies are presented and analyzed.

References

[1] L. F. Mollenauer, R. H. Stolen, J. P. Gordon, Phys. Rev. Lett. **45**, No. 13 (1980)

[2] M. H. Anderson, J. R. Ensher, M. R. Matthews, C. E. Wieman, E. A. Cornell, Science, **269**, No. 5221, 198-201 (1995)

[3] E. P.Gross, Nuovo Cimento **20** 454 (1961)

[4] E. P.Gross, J. Math. Phys. **4** 195 (1963)

[5] L. P. Pitaevskiii, Sov. Phys. JETP **13**, 451 (1961)

[6] R. Y. Chiao, E. Garmire, and C. H. Townes Phys. Rev. Lett. **13**, 479-482 (1964)

[7] P. L. Kelley, Phys Rev Lett **15**, No. 26, 1005-1008 (1965)

[8] V. I. Talanov, JETP Lett. **2**, No. 5 (1965)

[9] Ostrovsky, JETP (1966).

[10] D. J. Benney, A. C. Newell, Journal of Mathematics and Physics, **46**, No. 2 (1967).

[11] V.E. Zakharov, A.B. Shabat, Sov. Phys. JETP **34**, 62 (1972).

[12] Y. Kodama, A. Hasegawa, IEEE Journal of Quantum Electronics **23**, No. 5, 510-524 (1987).

[13] J. V. Moloney, A. C. Newell, *Nonlinear Optics*, Westview Press, Boulder, 2004.

[14] A. Hasegawa, F. Tappert, Appl. Phys. Lett **23** No. 142 (1973).

[15] A. Hasegawa, Y. Kodama, Progress in Optics **30**, 205-259 (1992).

[16] P. V. Mamyshev, L. F. Mollenauer, Opt. Lett. **21**, 6 (1996).

[17] J. N. Elgin, Phys. Lett. A, **110A**, 9 (1985).

[18] J. P. Gordon, H. A. Haus, Opt. Lett. **11**, 10 (1986).

[19] L. F. Mollenauer, J. P. Gordon, S. G. Evangelides, Opt. Lett. **17** 22 (1992).

[20] G.P. Agrawal, *Nonlinear Fiber Optics* (Academic Press, San Diego, 1995).

[21] R. W. Boyd, *Nonlinear Optics*, Academic Press, Boston, 1992.

[22] Z. S. Agranovich, V. A. Marchenko, Doklady Akademii Nauk SSSR, **113**, 5 (1957).

[23] V.E. Zakharov, A.B. Shabat, Funct. Anal. Appl. **8**, 226-235 (1974).

[24] V.E. Zakharov, A.B. Shabat, Funct. Anal. Appl. **13**, 166-174 (1979).

[25] D.J. Kaup, Phys. Rev. A **42**, 5689 (1990).

[26] J.N. Elgin, T Brabec, and S.M.J Kelly, Opt. Commun. **114** 321 (1995).

[27] A. Peleg and Y. Chung, J. Phys. A **36**, 10039 (2003).

[28] A. Hasegawa and Y. Kodama, *Solitons in optical communications* (Clarendon Press, Oxford, 1995).

[29] E. Iannone, F. Matera, A. Mecozzi, and M. Settembre, *Nonlinear Optical Communication Networks* (Wiley, New York, 1998).

[30] L.F. Mollenauer, J.P. Gordon, and P.V. Mamyshev, in *Optical fiber Telecommunications III*, edited by I.P. Kaminov and T.L. Koch, (Academic Press, San Diego, 1997) Chap. 12 Sec. V-B.

[31] H.A. Haus and W.S. Wong, Rev. Mod. Phys. **68**, 423 (1996).

[32] A. Peleg, M. Chertkov, I. Gabitov, Phys. Rev. E **68**, 026605 (2003).

[33] A. Peleg, M. Chertkov, I. Gabitov, J. Opt. Soc. Am., **21**, no.1, p.18-23.

[34] L.F. Mollenauer, P.V. Mamyshev, and M.J. Neubelt, Electron. Lett., **32**, 471 (1996).

[35] L.F. Mollenauer and P.V. Mamyshev, IEEE J. of Quantum Electron., **34**, 2089 (1998).

[36] Y.S. Kivshar and B.A. Malomed, J. Phys. A **19**, L967 (1986).

[37] B.A. Malomed, Phys. Rev. E **43**, 3114 (1991).

[38] D. Pushkarov, S. Tanev, Opt. Comm. **124**, 354 (1996).

[39] C. Zhou, X.T. He, and S. Chen, Phys. Rev. A **46**, 2277 (1992).

[40] J. Yang and D.J. Kaup, SIAM J. Appl. Math. **60**, 967 (2000).

[41] J. Soneson, A. Peleg, Physica D **195**, 123 (2004).

[42] H. Yoshida, Phys. Lett. A **150**, 5-7 (1990).

[43] G. Strang, SIAM J. Numer. Anal. **5**, 3 (1968).

[44] F. Neri, "Lie algebras and canonical integration", Department of Physics, University of Maryland, preprint (1988).

[45] J. W. Cooley, J. W. Tukey, Math. of Comp. **19**, No. 90, 297-301 (1965).

[46] S. O. Fatunla, *Numerical methods for initial value problems in ordinary differential equations*, Academic Press, Boston, 1988.

[47] J. P. Berenger, Journal of Computational Physics, **114**, 185-200 (1994).

[48] T. Hagstrom, *New results on absorbing layers and radiation boundary conditions*, Department of Mathematics and Statistics, University of New Mexico, preprint (2002).

[49] M. Chertkov, Y. Chung, A. Dyachenko, I. Gabitov, I. Kolokolov and V. Lebedev, Phys. Rev. E, **67**, 036615 (2003).

[50] J.M. Soto-Crespo, N.N. Akhmediev, and V.V. Afanasjev, J. Opt. Soc. Am. B **13**, 1439 (1996).

[51] J.M. Soto-Crespo, N.N. Akhmediev, V.V. Afanasjev, and S. Wabnitz, Phys. Rev. E **55**, 4783 (1997).

[52] F. Hache, D. Ricard, C. Flytzanis, J. Opt. Soc. Am. B **3**, No. 12, 1647 (1986).

[53] S. G. Rautian, Zh. Eksp. Teor. Fiz. (JETP) **112**, 836-855 (1997).

[54] V. P. Drachev, E. N. Khaliullin, W. Kim, F. Alzoubi, S. G. Rautian, V. P. Safonov, R. L. Armstrong, V. M. Shalaev, Phys. Rev. E **69**, 035318 (2004).

[55] V. P. Drachev, A. K. Buin, H. Nakotte, V. M. Shalaev, Nano Lett. **4**, No. 8, 1535-1539 (2004).

[56] V. M. Shalaev, in *Optical Properties of Random Nanostructures*, Ed: V. M. Shalaev, Springer-Verlag, Topics in Applied Physics v.82, Berlin Heidelberg 2002.

[57] http://www.webelements.com.

[58] J. -Y. Bigot, J. -C. Merle, O. Cregut, A. Daunois, Phys. Rev. Lett. **75**, 4702 (1995).

[59] M. Perner, P. Bost, G. von Plessen, J. Feldman, U. Becker, M. Mennig, M. Schmitt, H. Schmidt, Phys. Rev. Lett. **78**, 2192 (1997).

[60] T. Klar, M. Perner, S. Grosse, G. Von Plessen, W. Spirkl, J. Feldman, Phys. Rev. Lett. **80**, 4249 (1998).

[61] B. Lamprecht, A. Leitner, F. R. Aussenegg, Appl. Phys. B **68**, 419 (1999).

[62] T. B. Shahbazyan, I. E. Perakis, J. -Y. Bigot, Phys. Rev. Lett. **81**, 3120 (1998).

[63] T. V. Shahbazyan, I. E. Perakis, Chem. Phys. **251**, 37 (2000).

[64] V. Halte, J. Guille, J. -C. Merle, I Perakis, J. -Y. Bigot, Phys. Rev. B **60**, 11738 (1999).

[65] C. Voisin, D. Christofilos, N. Del Fatti, F. Vallee, B. Prevel, E. Cottancin, J. Lerme, M. Pellarin, and M. Broyer, Phys. Rev. Lett. **85**, 2200 (2000).

[66] R. N. M. Groeneveld, R. Sprik, and A. Lagendijk, Phys. Rev. B **51**, 11433 (1995).

[67] N. Del Fatti, R. Bouffanais, F. Vallee, and C. Flytzanis, i Phys. Rev. Lett. **81**, 922 (1998).

[68] J. Lehmann, M. Merschdorf, W. Pfeiffer, A. Thon, S. Voll, G. Gerber, J. Chem. Phys. **112**, 5428 (2000).

[69] Communication with V. P. Drachev.

[70] N. Akhmediev, J. M. Soto-Crespo, G. Town, Phys. Rev. E. **63** 566021 (2001).

[71] V. P. Safonov, V. M. Shalaev, V. A. Markel, Yu. E. Danilova, N. N. Lepeshkin, W. Kim, S. G. Rautian, and R. L. Armstrong Phys. Rev. Lett. **80**, 1102-1105 (1998).

[72] G.P. Agrawal, *Fiber-Optic Communication Systems* (Wiley, New York, 1997).

[73] L. Allen, J.H. Eberly, *Optical Resonance and Two-Level Atoms*, Wiley-Interscience, New York, 1975.

[74] I. R. Gabitov, V. E. Zakharov, A. V. Mikhailov, JETP **86** 1204 (1984).

[75] Basharov on the Duffing oscillator.

[76] I. P. Gabitov, R. Indik, N. Litchinitser, A. I. Maimistov, V. M. Shalaev, J. E. Soneson, *Resonant Interaction of Optical Pulses with Plasmonic Oscillations in Metallic Nanoparticles*, in preperation.

[77] G. P. Agrawal, in *The Supercontinuum Laser Source*, Ed: R. R. Alfano, Springer-Verlag, New York 1989.

[78] Communication with Avner Peleg.

[79] E. A. Kuznetsov, A. V. Mikhailov, I. A. Shimokhin, Physica D; **87** 201-215 (1995).

[80] R. Walsworth, S. Yelin, M. Lukin, Optics & Photonics News **13**, 50 (2002).

[81] R. H. Goodman, R. E. Slusher, M. I. Weinstein, J. Opt. Soc. Am. B **19**, 1635 (2002).

[82] E. A. Kuznetsov, Sov. Phys. Dokl, **22** 9 (1977).

[83] S. Kapur, V. Rokhlin, SIAM J. Numer. Anal. **34**, No. 4 (1997).